Radboud Repository

Radboud University Nijmegen

PDF hosted at the Radboud Repository of the Radboud University Nijmegen

The following full text is a publisher's version.

For additional information about this publication click this link.
http://hdl.handle.net/2066/145716

Please be advised that this information was generated on 2017-12-05 and may be subject to change.

Far-Infrared Magneto-Optics of Low Dimensional Semiconductor Structures and Organic Conductors

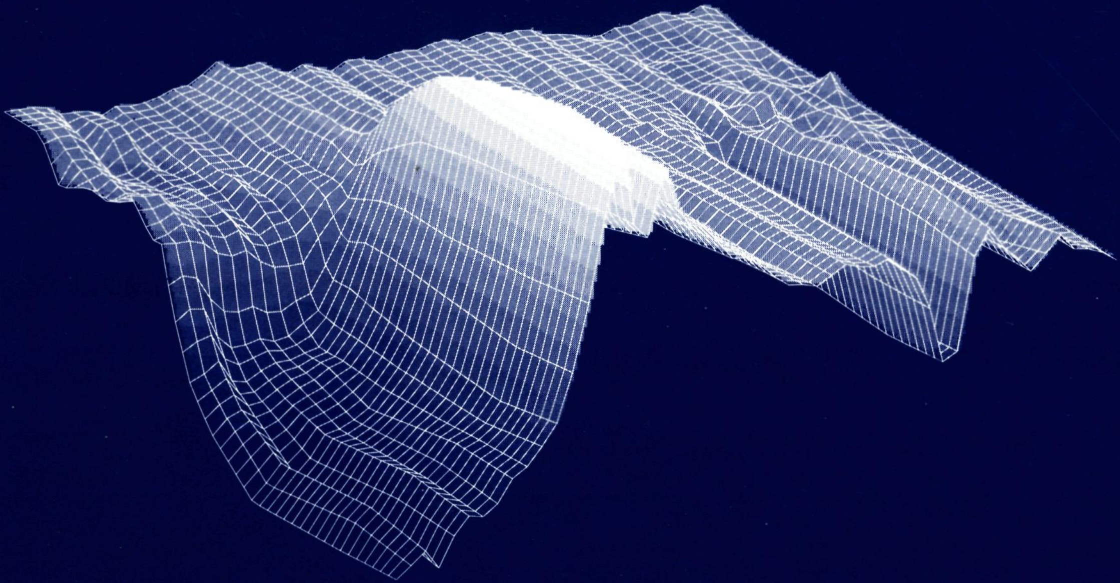

Jan-Theodoor Janssen

Far-Infrared Magneto-Optics of Low Dimensional Semiconductor Structures and Organic Conductors

CIP-GEGEVENS KONINKLIJKE BIBLIOTHEEK, DEN HAAG

Janssen, Theodorus Johannes Bernardus Maria

Far-infrared magneto-optics of low dimensional
semiconductor structures and organic conductors /
Theodorus Johannes Bernardus Maria Janssen. - [S.l. :s.n.]. - Ill.
Proefschrift Nijmegen. - Met lit. opg. - Met samenvatting
in het Nederlands.
ISBN 90-9006609-8
Trefw.: halfgeleiders / organische geleiders / infrarood
spectroscopie.

Far-Infrared Magneto-Optics of Low Dimensional Semiconductor Structures and Organic Conductors

een wetenschappelijke proeve op het gebied van
de Natuurwetenschappen

Proefschrift

ter verkrijging van de graad van doctor aan
de Katholieke Universiteit Nijmegen,
volgens besluit van het College van Decanen
in het openbaar te verdedigen op
dinsdag 18 januari 1994,
des namiddags om 3.30 uur precies

door

Theodorus Johannes Bernardus Maria Janssen

geboren op 2 november 1965
te Oudenbosch

Promotor: Prof. Dr. H. van Kempen
Co-promotor: Dr. J.A.A.J. Perenboom

Het werk beschreven in dit proefschrift maakt deel uit van het onderzoeksprogramma van de Stichting voor Fundamenteel Onderzoek der Materie (FOM) en is mede mogelijk gemaakt door financiële steun van de Nederlandse Organisatie voor Wetenschappelijk Onderzoek (NWO). De internationale samenwerking bij dit onderzoek werd mogelijk gemaakt door de financiële steun van de Europese Gemeenschap.

voor Willemijn

Het zou een misverstand zijn om te veronderstellen dat dit boekje het werk is van slechts één persoon, vele mensen hebben een grote of kleine bijdrage geleverd aan het totstand komen hiervan. Met name de interactie met talloze buitenlandse onderzoekers was een stimulerende en plezierige ervaring. Ik ben hen alle zeer dankbaar hiervoor. Een aantal mensen zou ik graag met name willen bedanken:

- *Allereerst Jos Perenboom voor de prettige samenwerking en de mogelijkheden/vrijheden die ik heb gekregen om mijn onderzoek te verrichtten.*
- *Alle medewerkers van de afdeling Experimentele Vaste Stof Fysica 2 o.l.v. Herman van Kempen voor de prettige sfeer en de goede samenwerking. In het bijzonder dank ik Ton Gerrits voor het samen delen van het vele experimentele lief en leed in de afgelopen jaren (vooral veel van dat laatste) en de talloze potjes Triviant die we gedurende de lange nachten gespeeld hebben.*
- *De kollega's van het magnetenlab, te weten Klaas, die menig nachtje door mij uit bed is gebeld vanwege weer een vergeten schakelaartje, Jos en Lijnis die in no-time de meest onmogelijke ideeën wisten te verwezenlijken, Olek voor de nodige hulp bij de bits, bauds en bytes, Jan voor zijn goede ideeën en nimmer aflatende drang tot experimenteren, en natuurlijk Hung, Harry, Elma, en Peter.*
- *Jan Kees Maan voor zijn immer kritische maar oprechte aanwijzingen aangaande het manuscript en in het bijzonder voor de inspirerende discussies omtrent hoofdstuk 2.*
- *Nalin Patel and Donald Arone are gratefully acknowledged for producing beautiful mesoscopic samples and the many successful experiments we did on those.*
- *Martyn Chamberlain and Stuart Hawksworth I thank for our co-operation on the hole gases. In this context I also want to thank Ulf Ekenberg and Annalisa Fasolino for explaining the secrets about Landau level diagrams.*
- *In particular I want to thank James Brooks, and Alex Perel from Boston University for many successful collaborations, impossible experiments and interesting life experiences (Speed Bowling). In addition, I want to express my gratitude to Mitra for her very kind hospitality during my visit to Boston.*
- *I also enjoyed working with Francis Pratt, Mariano Doporto, Steven Hill and Peter-Paul Hendriks (ik heb jou hier ook maar bij gezet) from the University of Oxford. But I am most grateful to John Singleton who was an inspiring and stimulating teacher in the beginning years and later, after he returned to Oxford, kept on being involved. His enthusiasm and support have been indispensable.*

Tot slot bedank ik mijn ouders, familie, en (muziek)vrienden voor hun belangstelling en steun, maar vooral voor de nodige ontspanning buiten de natuurkunde. Echter mijn grootste dank gaat uit naar Willemijn, die met haar steun, begrip en vooral liefde mij altijd terzijde heeft gestaan. Aan jou draag ik daarom dit proefschrift op.

Jan-Theodoor

Preface

In this thesis a number of far-infrared magneto-optical experiments are reported on two totally different classes of low dimensional systems. The term "low dimensional" refers in this context to the dimensionality of the electronic system (which is less than three). From the studies reported much insight is gained into the effects of the reduced dimensionality on the physical properties of the systems, such as for example the electronic excitation spectrum.

The first part of the thesis is devoted to the study of low dimensional semiconductor structures, which can be produced artificially with layer by layer growth techniques. The dimensionality of the two-dimensional semiconductor so created can be further reduced by subsequent nanoscale patterning. Also the application of a high magnetic field can be used to reduce the effective dimensionality through the Landau quantization of carrier movement. In this way devices can be produced in which the charge carriers are confined to zero, one or two dimensions (chapter 1, 2 and 3, respectively).

The second part of the thesis is dedicated to a study of the spectroscopic properties of organic charge-transfer salts. In these materials the low dimensionality is a consequence of the molecular structure of the crystal and so occurs naturally. By proper choice of cation- and anion-molecules crystals result which can be quasi-one-dimensional (chapter 4) or quasi-two-dimensional (chapter 5).

The two different systems are characterized by their low dimensional electronic properties, and so have much physics in common. However, from a material point of view they are extremely different. The charge carriers in semiconductors can be considered in first approximation as independent (non-interacting) particles. Their electronic properties are to a great extent determined by the size and geometry of the confining potential which can give rise to quantization effects. In organic compounds strong interactions between charge carriers mutually and between charge carriers and the lattice play an important role. These interactions together with the characteristic low dimensional Fermi surfaces of organic materials result in a rich phase diagram with many intriguing phase transitions at low temperatures and high magnetic fields.

Contents

I LOW DIMENSIONAL SEMICONDUCTORS 3

Introduction 5

1 Magneto-optical and capacitance study of voltage tunable quantum dots 9
- 1.1 Introduction 10
- 1.2 The quantum dot devices 12
- 1.3 Experimental results 15
  - 1.3.1 Capacitance measurements 15
  - 1.3.2 Optical measurements on a modulated 2DEG 17
  - 1.3.3 Optical measurements on isolated dots 19
- 1.4 Discussion 23
- 1.5 Summary 27

2 Ballistic transport, and photo-response in a 1D channel 31
- 2.1 Introduction 32
- 2.2 The split gate device; quantization of the conductance 33
- 2.3 Ballistic transport in one dimension: additional quantization produced by an electric field 35
  - 2.3.1 Experimental details and results 36
  - 2.3.2 Discussion 37
  - 2.3.3 Summary 43
- 2.4 Photo-response of a 1D channel 43
  - 2.4.1 Experimental details and results 44
  - 2.4.2 Analysis of the experimental results 46
  - 2.4.3 Bolometric heating effects 50
  - 2.4.4 Discussion 52
  - 2.4.5 Summary 53

3 Cyclotron resonance of high mobility GaAs-(Ga,Al)As (311) 2D hole gases 57
- 3.1 Introduction 58
- 3.2 (311)A Hole gas heterostructures 59
- 3.3 Experimental results 60
  - 3.3.1 Calculation of hole Landau levels in magnetic field 65
- 3.4 Discussion 68
- 3.5 Summary 70

II LOW DIMENSIONAL ORGANIC CONDUCTORS 73

Introduction 75

4 Magneto-optics of the quasi-1D organic conductor $(TMTSF)_2ClO_4$ 79
- 4.1 Introduction . . . 80
  - 4.1.1 Crystal and electronic structure . . . 81
  - 4.1.2 Theory on quasi-one-dimensional conductors . . . 84
- 4.2 Magnetic field dependent behaviour in $(TMTSF)_2ClO_4$ . . . 89
  - 4.2.1 Experimental details . . . 90
  - 4.2.2 Results . . . 90
  - 4.2.3 Discussion . . . 92
  - 4.2.4 Summary . . . 95
- 4.3 FIR spectroscopy of the FI-SDW gap in $(TMTSF)_2ClO_4$ . . . 95
  - 4.3.1 Experimental details . . . 96
  - 4.3.2 Results . . . 97
  - 4.3.3 Discussion . . . 100
  - 4.3.4 Summary . . . 103
- 4.4 Temperature dependence of the excitation spectrum in $(TMTSF)_2ClO_4$ . . . 103
  - 4.4.1 Experimental details . . . 104
  - 4.4.2 Results . . . 104
  - 4.4.3 Discussion . . . 107
  - 4.4.4 Hysteresis and memory effects . . . 109
  - 4.4.5 Summary . . . 110

5 Cyclotron resonance of the quasi-2D organic conductor $(BEDT\text{-}TTF)_2\text{-}KHg(SCN)_4$ 115
- 5.1 Introduction . . . 116
- 5.2 Crystal and electronic structure . . . 117
- 5.3 Magneto-transport results . . . 118
- 5.4 Cyclotron resonance measurements . . . 121
  - 5.4.1 Experimental details and results . . . 121
  - 5.4.2 Discussion . . . 123
- 5.5 Summary . . . 125

Summary 127

Samenvatting 131

List of publications 135

Curriculum Vitae 139

Part I

LOW DIMENSIONAL SEMICONDUCTORS

Introduction

During the last decade semiconductor technology has continued to make impressive advances in miniaturization. The size of electronic components has approached the regime where the classical description of diffusive electron transport breaks down and quantum concepts take over, and this brings about fundamental changes in electronic and optical properties. In principle two major technological developments have ushered in the era of reduced dimensionality condensed matter physics.

The first step has been the sophistication of ultra-thin epitaxial film growth techniques (molecular beam epitaxy (MBE) [1] and metal organic chemical vapor deposition (MOCVD) [2]). In the last decade, it has become possible to grow high quality crystalline layers of semiconductors with nearly atomic abruptness in compositional transition. This has generated an exceedingly rich field, since the ability to vary composition, band offset, periodicity, and other variables results in nearly limitless possibilities in creating structures for physical exploration as well as for electronic and optical device applications. For example, the combination of GaAs and $\mathrm{Al}_x\mathrm{Ga}_{1-x}\mathrm{As}$ in a heterostructure, results in a system which possesses a built-in electric field, creating a one-dimensional well at the interface. While the carriers remain free to wander in the plane of the interface, their motion in the perpendicular direction is quantized by this narrow well, and a two-dimensional electron gas (2DEG) [3] results. Using modulation doping [4], extremely pure 2DEG's with huge carrier mobilities can be created. Some fundamental phenomena discovered in the 2DEG include the celebrated integral [5] and fractional quantum Hall effects [6]; however, the 2DEG has also generated considerable practical interest, in for example the high electron mobility transistor [7,8]. Yet, because the epitaxial semiconductor structures inherently are two-dimensional, investigations have generally concentrated on quantum confinement in the growth direction.

The second step, developed in the last few years, has been the progress in nanoscale-fabrication technology which allowed additional lateral dimensions of quantum confinement on two-dimensional systems. These techniques include the use of electron beam or holographic lithography followed by either deposition of a metal gate or etching [9]. In this way, devices can be produced with dimensions approaching those of the lengths in the epitaxial growth direction. Incorporating this dimensional scale onto high mobility 2DEG's creates structures that are smaller than other relevant electronic length scales. The electronic properties become then fully size and shape dependent; this regime is known as the ballistic quantum regime. The artificial structures obtained by these methods have revealed a wealth of novel physical properties [10]. In addition, nanostructured devices have the potential for revolutionary applications in electronics and optoelectronics [11].

The work presented in the first part of this thesis concerns the effects of the confinement of charge carriers in various low dimensional geometries, realized in semiconductor systems. These effects are studied using far-infrared (FIR) spectroscopic techniques and (to a lesser extent) transport measurements. In addition, a magnetic field is an important parameter in these investigations. The application of a magnetic field quantizes the motion of the carriers into cyclotron orbits in the plane perpendicular to the field as a result of the Lorentz force, and gives rise to Landau levels. Effectively this results in adding a magnetic confinement (measured by the cyclotron radius) to the electrostatic confinement determining the geometry of the carrier system. The delicate balance between this magnetic and electrostatic confinement can be probed by FIR spectroscopy and transport measurements.

Imposing ultrafine lateral confinement at length scales of about 100 nm on an orignally 2D system will quantize the electron motion in the lateral direction. Ideally lateral confinement in one direction will define a quantum wire. Lateral confinement in two directions defines a quantum dot: an artificial atom with a totally discrete energy spectrum. Just as with real atoms, one expects to obtain information about the quantum confined energy levels in these low dimensional systems by optical studies of the electronic transitions. However, because a quantum dot is actually quasi-0D and confines more than one single electron, collective and many body effects are important and may even be dominant when the dimensions of the dots become large. In chapter 1, we present a study of quantum dot devices with different dimensions, defined in a high mobility GaAs-(Ga,Al)As heterostructure. In our devices we define the dots via the depletion action of a metal gate, which allows for a further reduction of the dot dimensions below the lithographically defined sizes. In addition, the gate also controls the number of electrons in the dots. The devices have been designed such that simultaneous measurement of the capacitance and FIR transmission in magnetic field is possible. The two types of measurements provide complementary information that is useful in determining the respective importance of the collective and single particle contributions to the observed optical response as a function of dot dimension and number of electrons in the dot.

One of the topics in low dimensional condensed matter physics is the observation of quantized conductance in a short and narrow ballistic 1D channel. Such a device, called a quantum point contact, can for example be made electrostatically by means of a split gate on top of a GaAs-(Ga,Al)As heterostructure containing a high mobility 2DEG at its interface. These devices are the analogue of point contacts defined in metals, which have been used extensively for the study of electron transport in metals. An essential difference between metallic point contacts and the 2DEG point contacts is that the transport through the former can generally be described classically. In the 2DEG point contacts however, the width can be made comparable with the Fermi wavelength, and quantum effects play an important role. Recently, quantum size effects have also been demonstrated in a novel type of ultra-small metallic "break" junctions [12]. In chapter 2, we present a transport and optical study of quantum point contact devices in the nonlinear transport regime. In zero magnetic field, we have observed steps in the differential conductance of e^2/h, as opposed to the "conventional" value of $2e^2/h$ for a assumes that the bias is dropped symmetrically in the 1D channel. The same effects were found to persist in a transverse magnetic field and allowed the subband spacings as a function of the applied magnetic field to be calculated. In the optical experiment, a strong *dc* voltage response was observed when a quantum point contact was subjected to high frequency (FIR) radiation. The response was found to exhibit oscillations when the number of occupied 1D subbands was varied. We will show that this signal can be explained by the rectification of the high frequency electric field, caused by the nonlinear 1D transport properties of the quantum point contact.

The major difference between holes and electrons, confined in a two-dimensional sheet, is that the holes have much higher effective masses and exhibit greater subband anisotropy as a result of the orbital degeneracy at the top of the GaAs valence band. We have performed cyclotron resonance experiments up to 20 T to study the Landau level spectrum in GaAs-(Ga,Al)As two-dimensional hole gases (2DHG); the results are presented in chapter 3. A full exploration of the Landau level spectrum has become possible due to advances in growth techniques which have resulted in a significant mobility increase to almost half a million $cm^2V^{-1}s^{-1}$ for GaAs-(Ga,Al)As 2DHG's grown onto (311)A oriented substrates. We have observed a large splitting of the cyclotron resonance, which we studied as a function of 2D hole density using a number of different samples. A self-consistent calculation of the Landau level diagram for the higher symmetry (100) direction was used to interpret this data and identify the observed transitions.

References

1. B.A. Joyce, Rep. Prog. Phys. **48**, 1637 (1985).
2. M.R. Leys, Chemtronics **2**, 155 (1987).
3. M.J. Kelly and R.J. Nicholas, Rep. Prog. Phys. **48**, 1699 (1985).
4. R. Dingle, H.L. Störmer, A.C. Gossard, and W. Wiegmann, Appl. Phys. Lett. **33**, 665 (1978).
5. K. von Klitzing, G. Dorda, and M. Pepper, Phys. Rev. Lett. **45**, 494 (1980).
6. D.C. Tsui, H.L. Stömer, and A.C. Gossard, Phys. Rev. Lett. **48**, 1559 (1982).
7. H. Sakaki, IEEE J. Quantum Electron. **QE22**, 1845 (1986).
8. K. Board, Rep. Prog. Phys. **48**, 1595 (1986).
9. For a review, see: *Science and Engineering of One- and Zero-dimensional Semiconductors*, edited by S.P. Beaumont and C.M. Sotomayor-Torres, Plenum Press, New York (1990).
10. For a review, see: *Nanostructured Systems*, edited by M.A. Reed, Semiconductors and Semimetals, Vol. **35** (1992).
11. For a recent update, see a series of articles in: Physics Today, June 1993.
12. C.J. Muller, J.M. Ruitenbeek, and L.J. de Jongh, Phys. Rev. Lett. **69**, 140 (1992).

Chapter 1

Magneto-optical and capacitance study of voltage tunable quantum dots

---

Parts of this work have been published in the following papers:

- *High Magnetic Fields in Semiconductor Physics III*, G. Landwehr ed.. Springer Series in Solid State Sciences **101**, 339 (1992).
- J. Phys.: Condens. Matter **5**, 1517 (1993).
- J. Phys.: Condens. Matter **5**, L1 (1993).

1.1 Introduction

The fundamental physics of systems with reduced dimensionality has stimulated considerable efforts to investigate experimentally and theoretically small, artificially confined electron systems [1]. At low temperatures a large number of interesting deviations from classical behaviour have been observed among various different low dimensional configurations. The preparation of these confined systems has been enabled by the rapid advances n nanoscale lithographic processing techniques, driven by the need for smaller and faster electronic devices [2].

Different semiconductors can be used to produce confined systems, however, the most frequently used base-material is the high mobility two-dimensional electron gas (2DEG) at the interface of a GaAs-(Ga,Al)As heterostructure [3], in which the electrons are already confined in one direction (denoted as the z-direction). They can move freely only parallel to the interface, leading to an energy spectrum $E^k(k_x, k_y) = \hbar^2 k_x^2/2m^* + \hbar^2 k_y^2/2m^* + E_z^k$ with the quantized energy levels E_z^k in the z-direction. The dimensionality can be further reduced by lateral confinement that quantizes the original free motion of the electrons parallel to the interface of the 2DEG. Confining only one direction will create a one-dimensional (1D) energy spectrum and results in so called quantum wires. Confining potentials both in the x- and y-direction will create a discrete energy spectrum $E^{i,j,k} = E_x^i + E_y^j + E_z^k$. The electrons in these systems are totally bound and their energy is quantized and dispersionless. In this limit the system can be thought of as an *artificial atom* or *quantum dot*, having however, confining potential different from the Coulomb potential in a natural atom.

Different methods have been used to create lateral confinement potentials, of which two are most generally applied; deep mesa-etching [4,5,6] or electrostatic depletion [7, 8,9,10]. With the first technique, material is removed all the way into the active layer at the 2DEG interface by the use of precisely optimized etching techniques [5]. In the second technique a negative voltage is applied to a metal gate at the top of the sample which depletes electrons from underneath its surface. In both cases a confined dot of electrons will be left at the position of the original 2DEG. In the case of dots defined by etching the carrier density and dimension are fixed, whereas for dots defined using the depletion action of gates these both can be varied. MOSFET semiconductor devices based on InSb [7] and Si [8] have also been used successfully to produce quantum dots. Frequently these devices have been produced with multiple stacked gates, which give the ability to separately tune the confining potential and carrier density of the dots.

The work on quantum dots has followed earlier extensive studies performed on one-dimensional wires that have been measured using transport [5,11] and optical techniques [12,13,14,15]. In the case of a quantum dot, electrical contacts necessary for transport measurements cannot be easily made and this has meant that the majority of the experiments have concentrated on capacitance studies [16,17] or optical spectroscopy [4,7,8,9,18], although some important transport experiments have been done on a special type of quantum dot devices [19]. In this case a dot geometry was created by using two quantum point probe the energy states in the dot.

The typical energies involved in the confined electron systems in semiconductor materials are of the order of several meV. hence the photon energies of the excitations lie in the far-infrared (FIR) regime. An additional complication in optical experiments is, that in order to produce an observable effect, large arrays of dots have to be made, which will be measured in parallel.

2D electron discs (with radius $R \approx 1.5$ μm) were first studied by Allen *et al.* [4] in periodic arrays of mesa-etched GaAs-(Ga,Al)As heterojunctions. Somewhat later confined 2D electron systems restricted to macroscopic discs ($R \approx 1$ cm) were examined by Glatti *et al.* [20] and by Mast *et al.* [21] on the surface of liquid helium. The excitations and their magnetic field dependent dispersion resemble each other in these two different systems and are described as classical depolarization, or equivalently, as edge magnetoplasmon modes [22]. In magnetic fields applied perpendicular to the discs, two type of modes can be identified; bulk-modes whose frequencies initially increase linearly with the cyclotron resonance frequency squared, and edge-modes whose frequencies decrease inversely with magnetic field [22]. More recently, for dots of much smaller dimensions ($R \approx 0.1$ μm) in various types of semiconductor systems [7,8], the same magnetic field dependent dispersion was observed, and interpreted on a quantum mechanical basis of excitations between single particle energy levels. In the intermediate regime both collective and single particle effects are thought to contribute to the observed resonance frequency [9,18.23]. However, from the experiments mentioned above no definite conclusions could be drawn, because either exact knowledge on dot dimension or carrier density lacked.

Due to rapidly advancing processing techniques, the size and number of electrons in the quantum dots have gradually decreased, and systems have now been developed, containing less than 3 electrons per dot. Novel effects of single electron charging have been observed in these systems [24,25]. Also the opposite of quantum dots, anti-dots have been studied [26], produced by etching circular "holes" in the homogeneous 2DEG. With an applied magnetic field, the electrons are forced to percolate around these anti-dots which leads to a very rich dispersion spectrum.

The quantum dot samples (with dot radii of 0.2 to 0.5 μm) used for the work reported in this chapter, have been designed so that both capacitance and FIR transmission experiments can be performed on the same sample. In our devices we can tune the dimensions of the dots via a metal gate, thereby bridging the range of dimensions used in the experiments above. The two types of measurements provide complementary information that is useful in determining the respective importance of the collective and single particle contributions to the observed dimensional resonance as a function of dot dimension and number of electrons in the dot.

This chapter is organized as follows. First, in section 1.2 the processing and operation of the devices is explained together with some remarks on the experimental details. In section 1.3 the capacitance and FIR transmission data are presented, followed by the discussion and summary in sections 1.4 and 1.5, respectively.

1.2 The quantum dot devices

The samples used in this experiment were fabricated at the Cavendish Laboratory of the University of Cambridge from a standard GaAs-(Ga,Al)As heterostructure, containing a high mobility 2DEG at AlGaAs/GaAs interface, and an additional Si δ-doped conducting layer 2000 Å below (Fig. 1.1). This δ-doped layer serves as a back contact and remains ohmic even when a bias voltage is applied to the gate. This layer can therefore be used as a ground plane relative to which the gate bias is applied, allowing for the electronic squeezing necessary to define the dots and also permitting the capacitance of the structure to be measured. The added advantage of using a δ-doped layer is that it is transparent to FIR radiation and so transmission experiments are possible with this device. The mesa was defined using optical lithography and wet etching. The substrate of the sample was wedged ($\approx 2^o$) in order to prevent multiple reflections within the sample and consequent distortion of the resonance lineshape [27]. Electrical ohmic contacts were formed with NiAuGe, annealed sufficiently to make contact to both conducting layers. The dots were defined on the mesa using electron beam lithography with high resolution negative (HRN) resist. This process produced a large periodic matrix of 0.5 μm high pillars of resist, and a total sample area of 4 mm^2 was covered by the matrix of dots. A gate was produced by evaporating a 50 Å thick layer of NiCr over the dots of resist as a semi-transparent gate. The dots are defined in the top most 2DEG by applying a negative gate voltage that depletes electrons selectively from underneath the gated regions. The NiCr covering the pillars of resist is disconnected from the rest of the NiCr by the steep walls of the pillars. Hence, the regions under the resist are not affected by the gate voltage, and remain

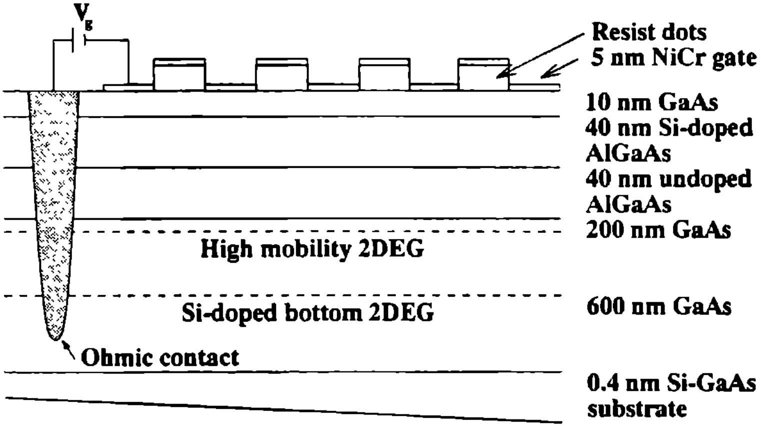

Figure 1.1 Schematic of the device (not to scale) showing the positions of the top most high mobility 2DEG and the bottom low mobility δ-doped 2DEG. The ohmic contact connects with both 2DEG's. The metal at the top of the resist dots is disconnected from the metal below, and thus no voltage is applied to these parts.

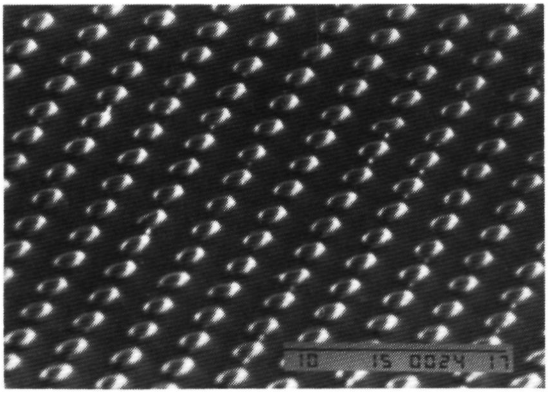

Figure 1.2 Scanning electron micrograph (SEM) picture of part of the sample surface (the black bar is 10 μm long). A regular matrix of dots is visible with periodicity of 2.25 μm and 0.5 μm dot radius. The sample surface contains approximately 10^6 dots in total.

undepleted, and it is these regions that forms the quantum dots to be investigated. The back contact, provided by the Si δ-doped layer, is spatially further away from the metal gate than the top 2DEG and so remains relatively unaffected by the gate voltage. Via the method described above, a series of samples were produced from the same wafer with different dot dimensions and periodicities. The samples used in this work are listed in Table 1.1 with their lithographic dot radii, array periodicities and carrier densities (at zero gate voltage). Figure 1.2 shows a SEM picture of a part of the sample surface, a regular periodic matrix of dots can be observed (the sample contains approximately 10^6 dots in total).

The measurements were undertaken in a ^{3}He cryostat at a temperature of approximately 400 mK. Unpolarized light from an optically pumped FIR laser was guided onto the sample, which was situated in the center of a 20 T Bitter magnet, via oversized light

Table 1.1 Lithographically defined dot radii and periodicities of the devices used in this work. Last column lists the carrier densities in the high mobility 2DEG calculated from SdH oscillations in the resistance measured at zero gate voltage.

Sample	Radius R (μm)	Period a (μm)	N_s ($\times 10^{11}$ cm^{-2})
#1	0.50	2.25	3.47
#2	0.37	1.60	1.18
#3	0.20	1.00	2.40

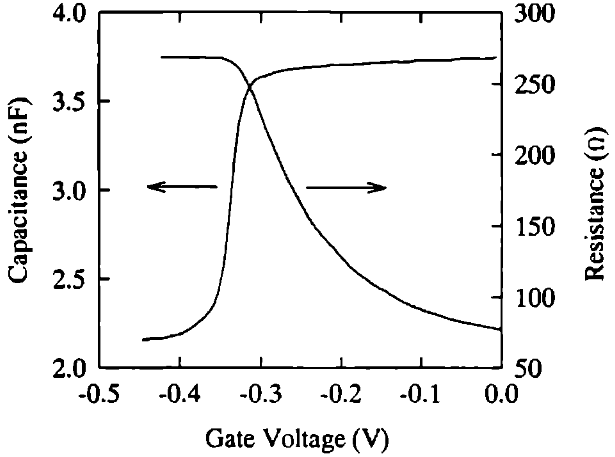

Figure 1.3 The resistance and capacitance of sample #2, shown as a function of gate voltage, showing a transition at a similar gate voltage which corresponds to the formation of isolated dots of electrons in the top most 2DEG.

guides. Various laser energies in the range from 1.77 to 17.74 meV were used and the transmitted signal was detected using a bolometer held at 1.2 K, situated directly below the sample. A reference bolometer was also placed above the sample to measure the incident laser power and allowed for the transmitted signal to be normalized. The capacitance measurements were performed by applying a small oscillating voltage superimposed on the gate voltage. The resulting oscillating current was measured between the gate and the conducting layers using a lock-in amplifier with the out-of-phase signal used to measure the capacitance between gate and the 2DEG. In the limit of a pure capacitance, the out-of-phase signal is directly proportional to the capacitance and this is valid as long as the resistive component, measured by the in-phase signal, is small. To ensure that the in-phase signal was negligible, a frequency around 10 kHz was used.

Characterization of the samples by transport measurements was carried out in order to extract mobilities of the two separate conducting layers, this indicated the presence of the two separate conducting layers. A large positive magneto-resistance followed by Shubnikov-de Haas (SdH) oscillations was observed. Analysis of the magneto-resistance data [28], results in values for the mobility of 1×10^6 and 1×10^4 $\mathrm{cm^2V^{-1}s^{-1}}$ for the top 2DEG and lower back contact respectively, with carrier densities of 2.7×10^{11} and 2×10^{12} $\mathrm{cm^{-2}}$ (in the dark for sample #1). The resistance and capacitance of the devices show a clear *turn-on* when the gate voltage is applied. The resistance increases and then remains virtually constant below a gate voltage of ≈ -0.3 V in sample #2 and #3 (≈ -0.2 V in sample #1), due to depletion of the top 2DEG while the δ-doped layer remains unaffected by the gate. Simultaneously, the depletion of the top 2DEG causes a decrease in the capacitance as shown in Fig. 1.3 for sample #2. This effect is easily understood as a reduction of the effective area that contributes to the sample capacitances: if the gate voltage is sufficient to completely deplete the 2DEG between the photoresist dots, the corresponding area no longer contributes to the capacitance.

1.3 Experimental results

1.3.1 Capacitance measurements

The capacitance measurements are primarily used to accurately monitor the carrier density, both before and after the dots are defined. As shown by Smith *et al.* [29], the magneto-capacitance (MC) of the 2DEG in a GaAs-(Ga,Al)As heterojunction is related to the density of states; oscillations in the capacitance are observed as a function of magnetic field, similar in many respects to SdH oscillations in the longitudinal conductivity. Such oscillations in the capacitance have been observed in our devices and are shown for various gate voltages in Fig. 1.4(a) and (b) for sample #1 and #2, respectively. For V_g=0.0 V our oscillations resemble those observed by Smith *et al.* [29] in a homogeneous 2DEG. However, as V_g decreases (more negative) the oscillations in the capacitance shift down in field, corresponding to a decrease in carrier density as the 2DEG electron density becomes more heavily modulated. For sample #1, at a gate voltage of −0.2 V the MC becomes unclear with the oscillations disappearing. As the gate voltage is further decreased, the MC oscillations reemerge. This transition corresponds to the regime where the 2DEG surrounding the dots is completely depleted; the capacitance is now due solely to the electrons in the dots [16,30]. The carrier densities for sample #1 extracted from these data, are shown in Fig. 1.5 as open triangles before the dots are isolated; an extrapolation to $N_s = 0$ indicates that the dots become isolated at $-0.3\text{ V} > V_g > -0.35\text{ V}$, below this voltage (denoted as V_{th}) the carrier density inside the dots is shown as filled squares.

The MC of sample #2 (see Fig. 1.4(b)), and sample #3 (not shown) shows a different behaviour: the amplitude of the oscillations also falls with decreasing gate voltage, with a dramatic reduction occurring at $V_g = -0.3$ V, until at $V_g = -0.35$ V they disappear and capacitance is seen to decrease with increasing magnetic field. However, no new period of oscillations appears on further decreasing the gate voltage below V_{th}, except for some very shallow structure at low fields.

The results of the capacitance experiment can be contrasted with those of other investigators. Smith *et al.* [30] also observed SdH-like capacitance oscillations in their quantum dots. Distinct oscillations in the MC occurred only at $B \geq 3.5$ T, a region inaccessible in our sample #2 because of the low carrier concentration. In addition, Hansen *et al.* [16] measured differential capacitance of an array of quantum dots. This array was similar in many respects to that utilized by us, with the important difference being that the radii of their dots was $R \sim 100$ nm. They observed an increase in the oscillation amplitude of the differential capacitance at high magnetic fields, which was attributed to a condensation of complex magneto-electric subbands [31] (influenced by

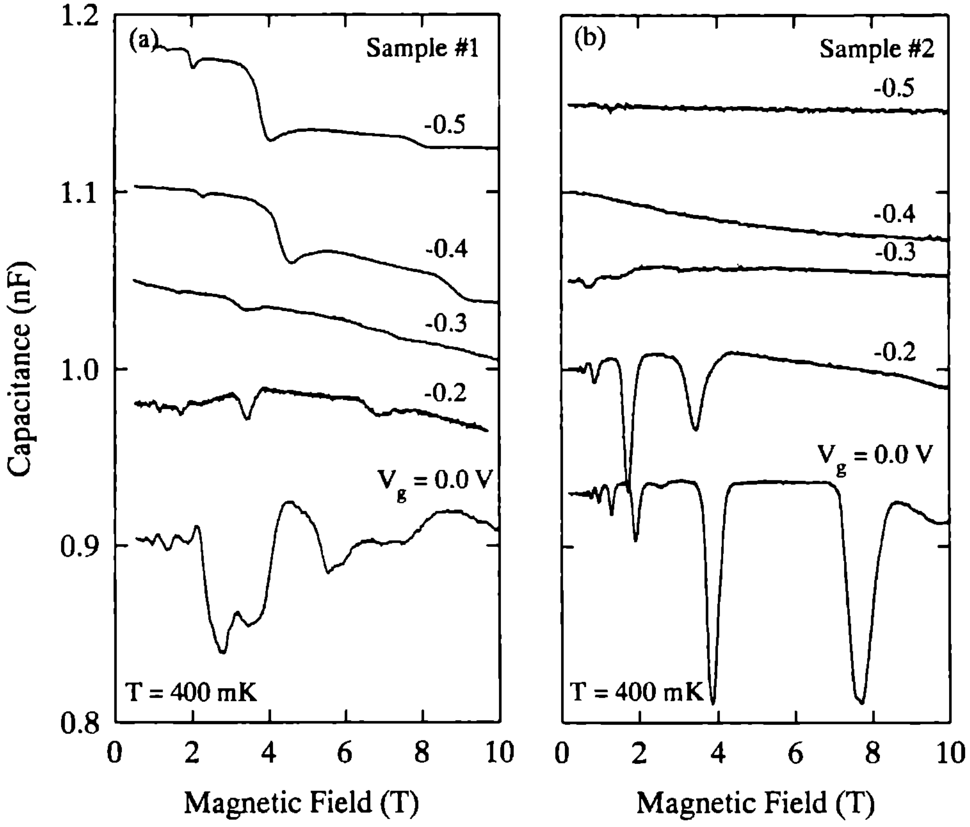

Figure 1.4 The magneto-capacitance shown as a function of magnetic field for different gate voltages (a) sample #1, and (b) sample #2. The traces are offset for clarity. The shift to lower fields of the oscillations is caused by a decrease in 2DEG carrier density. For the larger sized dots of sample #1 a new period of oscillations emerges after the dots become isolated, for the smaller sized dots of sample #2 no additional oscillations were observed.

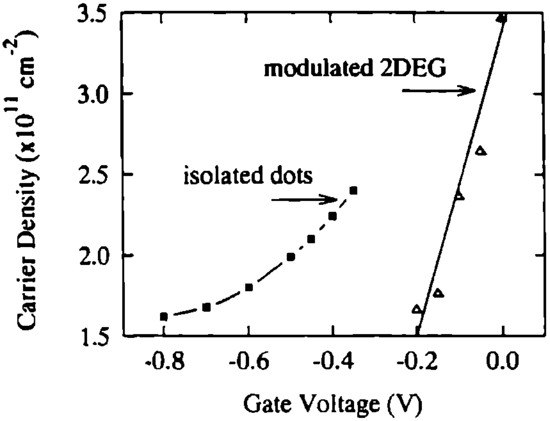

Figure 1.5 Carrier densities extracted from the magneto-capacitance data for sample #1 of Fig. 1.4(a). A clear transition occurs around $V_g \approx -0.3$ V: above this threshold the density of electrons in the 2DEG is measured, below the threshold only the signal from the electrons in the dots is observed.

samples #2 and #3 (with larger radius than those of the above mentioned workers) no SdH oscillations are observed indicates that the Landau levels in these samples must be considerably perturbed in comparison with the larger dot sample #1. We will return to this point below in section 1.3.3 where the optical measurements on these samples will be discussed.

1.3.2 Optical measurements on a modulated 2DEG

In this section we will present the results of optical experiments on sample #1 at gate voltages above V_{th}. In this regime the carrier density is laterally modulated, although still continuous. The transmission spectrum of sample #1 taken with a laser energy of 2.65 meV and zero gate voltage is shown as a function of the magnetic field in Fig. 1.6. The prominent feature is the cyclotron resonance dip that has a narrow linewidth and nearly 50% absorption, close to the maximum expected for unpolarized light [32]. The narrow linewidth indicates the high mobility of the heterostructures used in the experiment and the impedance matching by the metal NiCr gate [33]. Using the standard relationship for the cyclotron frequency $\omega_c = eB/m^*$, we obtain a value of 0.069 m_e for the effective mass that agrees with the value quoted for GaAs-(Ga,Al)As heterojunctions of this carrier density. Two side resonances are also observed at the low field side in the spectra, which can be identified as 2D magnetoplasmons [34,35]. These resonances are observed because the array of dots acts as a 2D grating coupler, resulting in the coupling of radiation to plasmons with finite wavevectors given by $q = 2\pi i/a$ where a is the array period and i is an integer. The dispersion of this 2D magnetoplasmon is given by,

$$\omega_p(B)^2 = \omega_p(0)^2 + \omega_c^2. \tag{1.1}$$

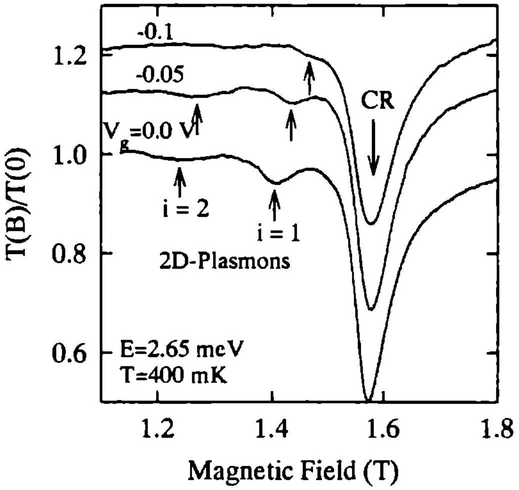

Figure 1.6 The transmission spectrum for three different gate voltages (corresponding to a modulated 2DEG) using a laser energy of 2.65 meV. The cyclotron resonance has nearly 50% absorption and the 2D plasmon about 5%. The grating induced harmonic $i = 2$ plasmon is also observed. As the gate voltage is applied the plasmon dips move to higher field due to the reduction in carrier density, leaving the cyclotron resonance position unchanged.

The plasmon energy in zero magnetic field can be calculated using a simple classical model [33]:

$$\omega_p(0)^2 = \frac{N_s e^2 q}{2m^* \epsilon_0 \epsilon_{\text{eff}}}, \tag{1.2}$$

where N_s is the carrier density and ϵ_{eff} is the effective dielectric constant. For the dielectric constant we need to take into account the screening of the metal gate and the media surrounding the 2DEG; this effective screening is obtained by using the following formula [33,36] that models our system closely

$$\epsilon_{\text{eff}} = \frac{[\epsilon_1 + \epsilon_2 coth(qd)]}{2}, \tag{1.3}$$

where ϵ_1 is the dielectric constant for GaAs, ϵ_2 the dielectric constant for AlGaAs and $d = 900$ Å is the distance between the 2DEG and the metal gate. Using the above relationships, taking $i = 1$ and using the value of the carrier density determined from the capacitance data, experimental and theoretical values of ω_p within 10% of each other were obtained. This is a very reasonable agreement, since no fitting parameters are used. The second shallow dip at lower magnetic field corresponds to the $i = 2$ value for the wavevector. This type of harmonic has been observed in experiments using conventional 1D grating couplers [33]. The experiments were repeated using different FIR wavelengths strengths when illuminated with long wavelength radiation. The energies of the plasmons obtained for the different wavelengths all agreed to within the experimental accuracy. A further confirmation of the identity of the 2D plasmons was obtained by flashing a LED whilst the sample was cold and repeating the measurements. The LED induces carriers by the persistent photoconductivity effect and enhances the mobility, this was observed as an increase in the percentage absorption and also a narrowing of the cyclotron resonance. The higher carrier density caused the magnetoplasmon peaks to move to lower field which corresponds to a higher energy, as expected from Eq. 1.2.

Applying a small negative gate voltage (above V_{th}) has the effect of reducing the carrier density, as obtained from analyzing the capacitance data. Correspondingly, the energy of the plasmons is reduced according to Eq. 1.2. This is seen in Fig. 1.6 where for a gate voltages of -0.05 and -0.1 V both magnetoplasmon resonances have moved closer to the cyclotron resonance. This effect continues for more negative gate voltages until the dots are isolated and all traces of 2D magnetoplasmons disappear.

1.3.3 Optical measurements on isolated dots

Upon decreasing the negative gate voltage to below V_{th} the area between the dots becomes fully depleted. Figure 1.7(a) shows the transmission spectra at $E = 2.65$ meV for several different gate voltages in this region. As the dots are formed in the top 2DEG a new absorption peak appears in the transmission spectra. Here we choose to plot the relative change in transmission as,

$$
\begin{aligned}
-\frac{\Delta T}{T} &= \frac{T(B) - T(0)}{T(0)} \qquad (1.4)\\
&\propto \operatorname{Re}\left[\sigma(\omega, B) - \sigma(\omega, 0)\right], \qquad (1.5)
\end{aligned}
$$

where $T(B)$ and $T(0)$ are the transmission spectra in finite field and zero field, respectively. In the small signal approximation this expression is proportional to the difference in the real parts of the dynamic conductivity $\sigma(\omega)$. A new absorption peak appears in the spectra which must originate from the confinement of electrons in the dots. Hereafter we will call this the dimensional resonance of the dots. The resonance in Fig. 1.7(a) moves to lower fields as the gate voltage is lowered, which is opposite to the 2D magnetoplasmon which moved to higher fields as the gate voltage is lowered (and which cannot exist in a system of isolated dots). For all gate voltages the cyclotron resonance absorption remains present in the spectra, but much diminished in magnitude. This is an artifact of our devices and is due to the presence of ungated regions on the sample, and appeared for all samples. For sample #1 the new side absorption was observed for all laser energies studied. The experimental resonance positions are plotted in Fig. 1.7(b) for two different gate voltages.

The lines drawn in Fig. 1.7(b) are the result of a calculation of the magnetic field dependent dispersion which is well described by the relation

$$
\omega_{\pm} = \frac{\pm\omega_c}{2} \pm \left(\left(\frac{\omega_c}{2}\right)^2 + \omega_0^2\right)^{1/2}, \qquad (1.6)
$$

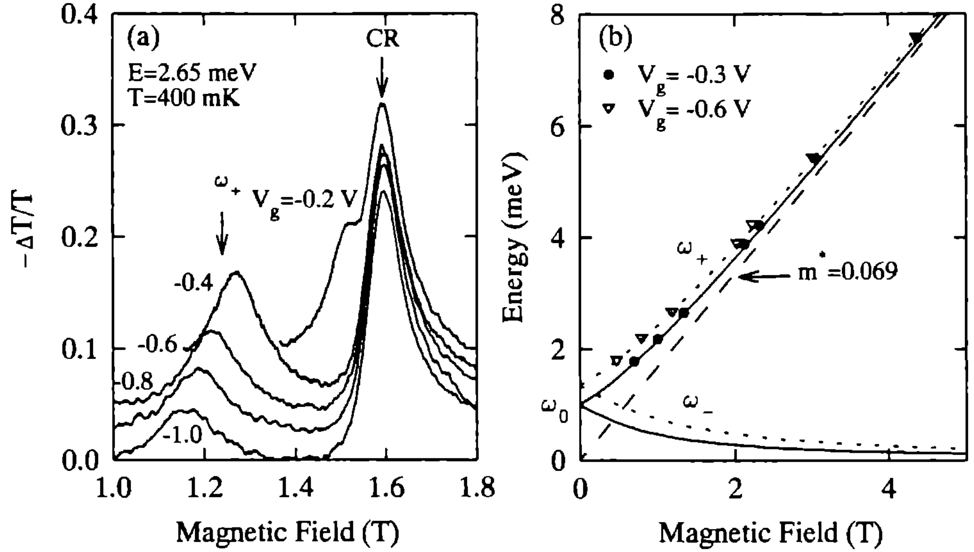

Figure 1.7 The relative transmission $-\Delta T/T$ taken at 2.65 meV is shown in (a) for different gate voltages. The traces are offset for clarity. The cyclotron resonance (CR) is unaffected while the dimensional resonance ω_+ (see text) moves to lower field. (b) The resonance positions of ω_+ for different energies from (a) plotted for two values of the gate voltage. The dashed line corresponds to $\hbar\omega_c = eB/m^*$ with $m^* = 0.069\ m_e$. The full and dotted lines correspond to $\hbar\omega_0 = 1$ meV and 1.3 meV (see text), respectively.

where ω_0 is the characteristic frequency of the dimensional resonance in the dots. This relation has been derived for harmonically confined electron dots by Allen *et al.* [4] and also follows with the correct dipole selection rules from a quantum mechanical calculations of the energy levels [37,38,39]. The ω_+-mode corresponds to electrons moving in the centre of the dot and becomes the usual bulk cyclotron resonance for high magnetic fields. The ω_--mode corresponds to electrons moving along the circumference of the dot and tends to zero for high magnetic fields. At zero magnetic field only the bare dimensional resonance ω_0 can be observed. The interpretation of the dimensional resonance frequency will be discussed below. In our measurements we only observe the positive branch, whereas in Fourier transform interferometer measurements also the lower ω_--branch was detected [4,8,9]: the magnetic field dependence of this branch is small and would therefore result in a resonance in the transmission spectrum too broad to measure in our devices.

We repeated the experiment for the smaller dot samples #2 and #3. Some of the resonances observed are shown in Fig. 1.8. The behaviour of these samples was found to be different in many respects compared with sample #1; the dimensional resonance could only be observed for high energies. There is some suggestion for a developing

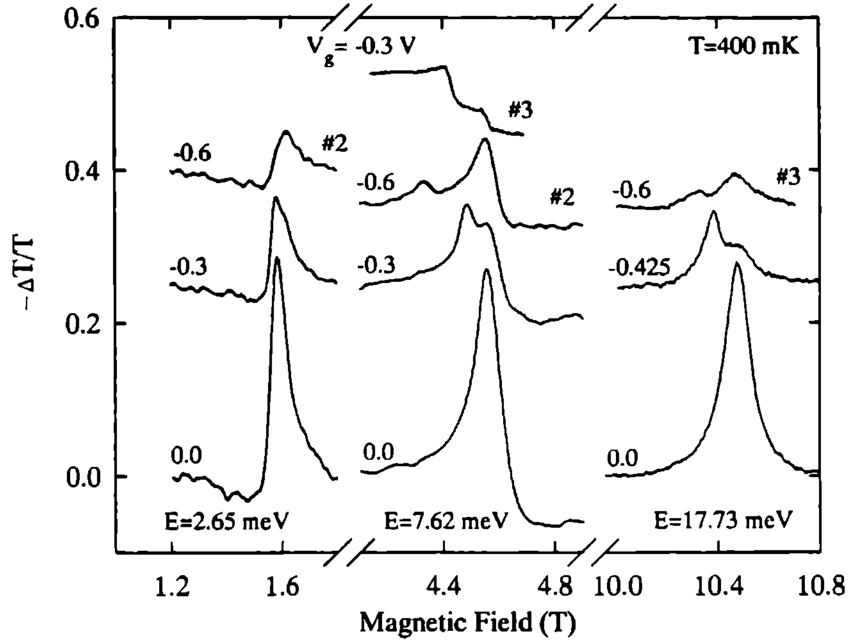

Figure 1.8 A comparison between transmission spectra taken at different energies for sample #2 and #3, showing cyclotron resonance and emerging dimensional resonance. The spectra for various gate biases V_g are offset for clarity.

resonance from the shape of the cyclotron resonance peak at $V_g = -0.3$ V for sample #2 at E=2.65 meV, but no new structure arises for more negative gate voltages. A distorted resonance is observed at E=7.62 meV for sample #3, whereas for sample #2 at the same energy a clear side peak occurs. For the higher energies both samples display a similar behaviour as observed for sample #1; a new side resonance appears after dots are formed and this resonance moves to lower magnetic fields when the gate voltage is further lowered, following the same dispersion as plotted in Fig. 1.7(b). The energy limit above which resonances are observed is found to scale with the lithographically defined dot radii for sample #2 and #3. We must therefore conclude that the cyclotron radius ($r_c = \sqrt{\hbar/eB}$) must be about 15 times smaller than the radius of the dot. The fact that for higher energies and thus higher magnetic fields dimensional resonances do occur, indicates that the confining boundary is responsible. These effects appear to be connected with the absence of SdH oscillations which should have been present for low magnetic fields in these samples as discussed before. The most probable cause is a non-uniform dot radius in our devices, as observed from SEM pictures. The samples are produced by "drawing" each dot separately with an electron beam, which takes a long time for roughly 10^6 dots. During this time the electron beam defocuses leading to smearing of the dot dimensions. This is an unfortunate draw-back as opposed to techniques where the dots are generated

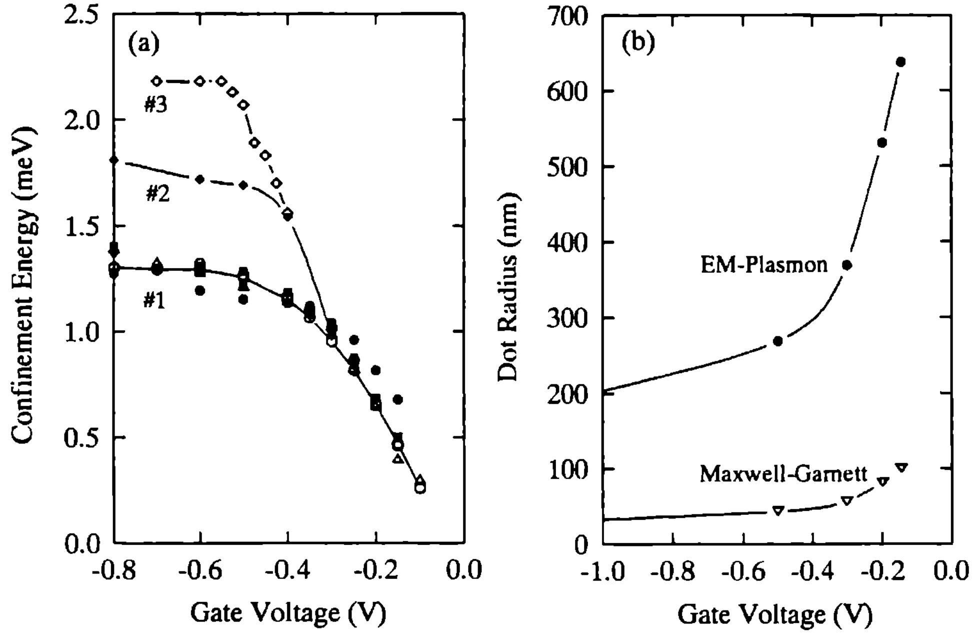

Figure 1.9 Confinement energy $\hbar\omega_0$ (a) and dot radius R (b) versus gate voltage. In (a) ◇ : sample #3, ◆ : sample #2, ○, ●, ▾, ■ : sample #1 at different energies. In (b) the calculated dot radius for sample #1 is plotted using two different models; the edge-magnetoplasmon model (●) and the classical Maxwell-Garnett theory (▽) for depolarization in a metal disk. In both figures, the lines are a guide for the eye.

using the interference pattern of a laser, which "draws" a complete array of very uniform dots in a few seconds. The non-uniformity will become more important for smaller dot sizes and lower magnetic fields where the cyclotron radius is larger, leading to considerable smearing and even disappearance of the resonances and SdH oscillations for low magnetic fields.

In Fig. 1.9(a), $\hbar\omega_0$ (evaluated from Eq. 1.6) is plotted against V_g for different laser energies, measured on all three samples. For sample #1 no energy dependence was observed for three different laser energies, indicating that the method of summing the cyclotron and dot energies in Eq. 1.6 has some validity for a real potential [40]. In all samples ω_0 shows the same V_g dependence, indicating that the action of the gate is similar for the different devices. A steep rise with approximately the same slope is observed, then a reduced slope after the dots are isolated. The energies of the flat parts, where the curves saturate, scale with the lithographically defined dot radii. Furthermore, we notice that the transition between the two regimes becomes increasingly sharper for smaller dot sized samples.

1.4 Discussion

Large Dots

We now first concentrate on the dimensional resonance which appears concurrently with the formation of the dots in the larger sample #1. If we evaluate the number of electrons in the dots from their size and carrier density around V_{th}, we find approximately 1000 electrons/dot. Hence, the dot is similar in many respect to a small bounded 2DEG. Dots of this type have been studied previously by Allen *et al.* [4]. They used a classical theory for *depolarization* in arrays of 2D metallic disks formulated by Maxwell-Garnett [41] to describe the response. In this model ω_0 is given by

$$\omega_0^2 = \frac{1}{8}\frac{N_s e^2}{2m^*\epsilon_0\epsilon_{\mathrm{eff}}R}, \tag{1.7}$$

where R is the radius, and N_s is the carrier density of the dot. From the experimentally obtained values of ω_0, N_s, and ϵ_{eff}, chosen the same as in Eq. 1.2, we can calculate the radius of the dot. Figure 1.9(b) shows the values of R extracted in this way. When the dots are first formed we expect a radius of 0.5 μm, as measured in SEM photographs of the sample. This corresponds to an energy of only 0.45 meV using the above model, which is lower than the measured value if we assume the dots are first formed at -0.30 V. Hence, this classical model considerably underestimates the observed confinement energy.

A better agreement can be found if we use the *edge magnetoplasmon model* [22,36,42] for a bounded plasmon in a 2DEG. In this model the circumference of the dot quantizes the 2D plasmon wavevector to $q = i/R$, which can be thought of as a standing wave. This model yields for ω_0 the result

$$\omega_0^2 = \left(\frac{2}{3}\right)^{1/2} \frac{N_s e^2}{2m^*\epsilon_0\epsilon_{\mathrm{eff}}R}. \tag{1.8}$$

This is essentially the same equation as obtained in the classical depolarization model except for the different prefactor. In this treatment the ω_--mode in Eq. 1.6 corresponds to a plasmon propagating at the edges of the dot with its frequency tending to zero for large magnetic fields.

Using Eq. 1.8 we find an energy of 1.15 meV for a 0.5 μm dot radius, which is close to the value we obtain experimentally. This indicates that the edge magnetoplasmon model is better suited to describe our data than the classical Maxwell-Garnett theory. Using this model further we see in Fig. 1.9(b) that the radius of the dots is reduced by nearly 50% due to the application of the gate voltage.

Small Dots

An analysis as used above for the larger sample #1 is not possible for the smaller dot samples #2 and #3, due to the lack of knowledge on the carrier densities in the latter case. However, Sikorski and Merkt [7] have shown that the number of electrons per dot, n_0 (with $N_s = n_0/a^2$, and a the dot periodicity), can be very accurately determined from the FIR absorption strength, similar to the case of cyclotron resonances in a homogeneous

2DEG. Below we will calculate this number for sample #1 and #3 using a lineshape analysis. In the case of sample #2 a calculation is more difficult due to the asymmetric ineshapes observed in the experimental traces (*e.g.* Fig. 1.8) which leads to large errors n the electron numbers and therefore these results are omitted. The results of sample #1 can be used as an independent check of the analysis in the previous part. To model the lineshapes, we first calculate the classical conductivity of the dot using [43],

$$\sigma_{\pm}(\omega) = \frac{e n_0 \mu}{1 + \left[(\omega_0^2/\omega) - \omega \pm \omega_c\right]^2 \tau^2} \tag{1.9}$$

for circular light polarizations with a phenomenological relaxation time τ, mobility $\mu = e\tau/m^*$, and n_0 the number of electrons in one dot. The relation between conductivity and relative change of transmission in the limit of small signal changes is given by [7,44],

$$-\frac{\Delta T}{T} \cong \frac{1}{a^2} \frac{2\sigma(\omega)/Y_0}{1 + \sqrt{\epsilon} + \sigma_\Box/Y_0} \tag{1.10}$$

with ϵ the dielectric constant, Y_0 the wave admittance of the vacuum, and $\sigma_\Box$ is the sheet conductivity of the NiCr gate and δ-doped layer. These parameters can be deduced from the cyclotron resonance with zero gate voltage applied, where the carrier density s accurately known from SdH data. For high energies only the ω_+-mode contributes to the conductivity and is included to calculate the relative transmission. Equation 1.10 can describe the observed lineshapes very well as illustrated in Fig. 1.10. Note that for sample #3 the dimensional resonance and the cyclotron resonance are not yet well resolved (*c.f.* Fig. 1.8), and consequently we had to take account of the cyclotron resonance originating n the ungated area of sample. From these fits one can determine directly the number of electrons per dot, n_0, and the results are listed in Table 1.2.

In Table 1.2 also the number of electrons per dot, N_0, is listed, calculated from the carrier densities and radii obtained in the previous sections (for sample #1). Good agreement is found between the values of N_0 and n_0 within the experimental accuracy, ndicating that the observed dimensional resonance can be properly accounted for in a plasmon model. Further proof for this statement is found in the transmission curves displayed in the inset of Fig. 1.10, for the same gate voltage before and after we flashed a LED. After the flash with the LED the maximum is shifted to lower magnetic fields corresponding to an increase in plasmon energy as expected from Eq. 1.8.

The results in Table 1.2 indicate that for sample #3 the number of electrons per dot decreases to only 30 at the most negative gate voltage. In dots containing even less electrons, it has been found by other workers [7,9,15], that quantization of the single particle motion becomes increasingly more important towards the extreme limit of one single electron per dot. In that case the system will represent an artificial atom, with a single particle energy spacing given by $\hbar\omega_{sp}$ (assuming a harmonic confinement potential). Simultaneously the edge magnetoplasmon energy given by Eq. 1.8 tends to zero. For two electrons per dot theoretical predictions indicate that $\hbar\omega_{sp}$ will be reduced due to mutual screening of the electrons [45,46]. When the electron number is increased further the

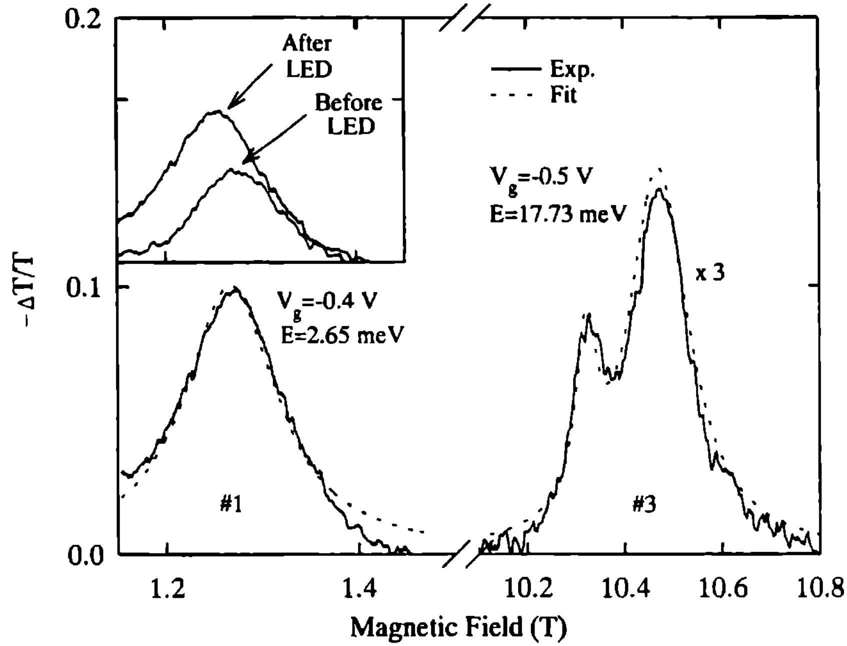

Figure 1.10 Measured (solid line) and fitted (dashed line) absorption curves form sample #1 and #3. For sample #3 the larger peak is the cyclotron resonance absorption originating from the ungated regions of the sample. The inset shows two transmission curves for sample #1 before and after a flash with a LED. The absorption is seen to increase and shift to lower magnetic fields corresponding to Eq. 1.8.

the character of local plasmons, as observed for sample #1. The observed dimensional resonance frequency ω_0 can thus be expressed as

$$\omega_0^2 = \omega_{sp}^2 + \omega_{mp}^2, \tag{1.11}$$

with ω_{mp} the edge magnetoplasmon term describing the collective effects. The single particle energy for sample #3 can be calculated from [7],

$$\hbar\omega_{sp} = 2\hbar^2 (n+1) / m^* r_F^2, \tag{1.12}$$

with r_F the radius of the electron orbits at the Fermi energy, and n the quantum number of the highest occupied level (for sample #3 at $V_g = -0.6$ V, $n \cong 5$ for $N_0 = 30$). For the radius we assume a value of 100 nm, which is 50% from the lithographically defined dot radius, and is the minimum value obtained by the squeezing action of the gate, *c.f.* Fig. 1.9(b) for sample #1. Equation 1.12 than yields $\hbar\omega_{sp} \cong 1.3$ meV, which is about 50% of the observed dimensional resonance energy ω_0. This estimate indicates that the

Table 1.2 Numbers of electrons per dot (n_0) evaluated from lineshape fits (see text) together with (for sample #1 only) the carrier densities (N_s) from SdH-data, dot radii (R) from edge magnetoplasmon model, and the number of electrons per dot N_0 calculated from these two parameters.

Sample #1					Sample #3	
V_g (V)	N_s ($\times 10^{11}$ cm^{-2})	R (nm)	N_0	n_0	V_g (V)	n_0
-0.40	2.24	325	745	735	-0.40	250
-0.50	1.99	270	460	465	-0.45	130
-0.60	1.80	225	425	430	-0.50	85
-0.80	1.62	210	225	305	-0.55	40
					-0.60	30

single particle and collective effects, at the most negative gate voltage in this sample, are of comparable size.

Recently, a somewhat different understanding about the FIR response of periodically confined systems has been triggered by Brey, Johnson, and Halperin [47]. In an argument quite similar to the one used by Kohn [48] to show that cyclotron resonance in a homogeneous system is unaffected by electron-electron interaction, Brey and coworkers showed for the particular case of a harmonically bound 3D electron gas that the long wavelength response of such a system occurs at the characteristic frequency ω_0 of the bare confining potential and is unaffected by electron-electron effects. This can be understood as due to the fact that the resonance mode driven by a uniform infrared field ($q = 0$) is associated with the center of mass motion of all electrons in the bare confining potential. The Hamiltonian for this center of mass motion is exactly like that for a single electron in a parabolic potential, except that the mass and charge are replaced by their N-fold value (N is the number of confined electrons). This argument applies equally well for electrons harmonically bound in a 1D and 0D potential, as was shown almost simultaneously by other workers [40,49]. The same results have been reached using the random phase approximation (RPA) [50] to calculate the FIR response. In that language the result means that, with increasing number of electrons per dot, again for a purely harmonic potential, the decrease in the single particle energy level separation is exactly compensated by the increasing depolarization shift, always yielding a single excitation at the frequency of the bare potential. If we assume that the electrostatic confining potential in our devices is of harmonic shape the increase of the resonance frequency, as observed in Fig. 1.9(a), must be interpreted as the combined result of a reduced radius and a stiffening of the bare confining potential when the gate voltage becomes more negative.

1.5 Summary

In summary, our experiments show that simultaneous measurements of capacitance and FIR transmission is possible in specially designed quantum dot samples. We have observed 2D magnetoplasmons, due to the action of the 2D array of dots as a grating coupler, and their characteristics agree accurately with theoretical predictions. More specifically, the energies of the plasmons scale as expected with applied magnetic field and carrier density. Once the dots are isolated, by fully depleting the area around them, an absorption peak is seen to arise which, for the larger dot sample, can be described by an edge magnetoplasmon model. Using this model and the carrier densities derived from the capacitance data, we calculate that the dot radius of our devices can be reduced by up to 50% by increasing the magnitude of the gate voltage. Hence, the action of the gate voltage on the dots is twofold: it reduces both the radius and the carrier density. The number of electrons could be determined independently from the calculated lineshapes of the dimensional resonances for the various gate voltages, and the agreement of the values obtained is a good confirmation of the validity of our models. For the smaller dot samples it is found that quantum confinement is becoming more important; for our smallest dot sample and at the most negative gate voltage we can estimate that the single particle and collective contribution to the dimensional resonance are becoming of equal magnitude. The absence of Shubnikov-de Haas oscillations and resonances at low energies in our smaller dot samples indicate that the dimensions of the dots in this case were not very uniform. A further improvement of the devices with more uniform dot radii, together with the use of wide band interferometer techniques at fixed field in order to also detect the lower branch of the dispersion relation, would be desirable.

References

1. *Nanostructured Systems*, edited by M.A. Reed, Semiconductors and Semimetals, Vol. **35** (1992).
2. *Granular Nanoelectronics*, edited by D.K. Ferry, Plenum Press, New York, 1991.
3. J.J. Harris, J.A. Pals, and R. Wolter, Rep. Prog. Prog. **52**, 1217 (1989).
4. S.J. Allen, H.L. Stormer, and J.C.M. Hwang, Phys. Rev. B **28**, 4875 (1983).
5. T.Demel, D. Heitmann, P. Grambow, and K. Ploog, Appl. Phys. Lett. **53**, 2176 (1988).
6. T. Demel, D. Heitmann, P. Grambow, and K. Ploog, Appl. Phys. Lett. **62**, 2168 (1989).
7. Ch. Sikorski and U. Merkt, Phys. Rev. Lett. **62**, 2164 (1989).
8. J. Alsmeier, E. Batke, and J.P. Kotthaus, Phys. Rev. B **41**, 1699 (1990).
9. A. Lorke and J.P. Kotthaus, Phys. Rev. Lett. **64**, 2559 (1990).
10. N.K. Patel, Ph.D. thesis, University of Cambridge (1991), unpublished.
11. T.J. Thornton, M. Pepper, H. Ahmed, D. Andrews, and G.J. Davies, Phys. Rev. Lett. **56**, 1198 (1986).

12. W. Hansen, M. Horst, J.P. Kotthaus, U. Merkt, C. Sikorski, and K. Ploog, Phys. Rev. Lett. **58**, 2586 (1987).
13. F. Brinkop, W. Hansen, J.P. Kotthaus, and K. Ploog, Phys. Rev. B **37**, 6547 (1988).
14. T. Demel, D. Heitmann, P. Grambow, and K. Ploog, Phys. Rev. B **38**, 12732 (1989).
15. J. Alsmeier, E. Batke, and J.P. Kotthaus, Phys. Rev. B **40**, 12574 (1989).
16. W. Hansen, T.P. Smith, K.Y. Lee, J.A. Brum, C.M. Knoedler, J.M. Hong, and D.P. Kern, Phys. Rev. Lett. **62**, 2168 (1989).
17. K. Ismail, T.P. Smith, W.T. Masselink, and H.I. Smith, Appl. Phys. Lett. **55**, 2766 (1989).
18. T. Demel, D. Heitmann, P. Grambow, and K. Ploog, Phys. Rev. Lett. **64**, 788 (1990).
19. B.J. van Wees, L.P. Kouwenhoven, C.J.P.M. Harmans, J.G. Williamson, C.E. Timmering, M.E.I. Broekaart, C.T. Foxon, and J.J. Harris, Phys. Rev. Lett. **62**, 2523 (1989).
20. D.C. Glatti, E.Y. Andrei, G. Deville, J. Poitrenaud, and F.I.B. Williams, Phys. Rev. Lett. **54**, 1710 (1985).
21. D.B. Mast, A.J. Dahm, and A.L. Fetter, Phys. Rev. Lett. **54**, 1710 (1985).
22. A. Fetter, Phys. Rev. B **32**, 7676 (1985).
23. T. Demel, D. Heitmann, P. Grambow, and K. Ploog, Superlattices and Microstructures **9**, 285 (1991).
24. R.C. Ashoori, H.L. Stormer, J.S. Weiner, L.N. Pfeiffer, S.J. Pearnton, K.W. Baldwin, and K.W. West, Phys. Rev. Lett. **68**, 3088 (1992).
25. B. Meurer, D. Heitmann, and K. Ploog, Phys. Rev. Lett. **68**, 1371 (1992).
26. K. Kern, D. Heitmann, P. Grambow, Y.H. Zhang, and K. Ploog, Phys. Rev. Lett. **66**, 1618 (1991).
27. G. Abstreiter, J.P. Kotthaus, J.F. Koch, and G. Dorda, Phys. Rev. B **14**, 2840 (1976).
28. M.J. Kane, N. Apsley, D.A. Anderson, L.L. Taylor, and T. Kerr, J. Phys. C: Solid State Phys. **18**, 5629 (1985).
29. T.P. Smith, B.B. Goldberg, P.J. Stiles, and M. Heiblum, Phys. Rev. B **32**, 2696 (1985).
30. T.P. Smith, K.Y. Lee, C.M. Knoedler, J.M. Hong, and D.P. Kern, Phys. Rev. B **38**, 2172 (1988).
31. A. Kumar, S. Laux, and F. Stern, Phys. Rev. B **42**, 5166 (1990).
32. L. Zheng, W.L. Schaich, and A.H. MacDonald, Phys. Rev. B **41**, 8493 (1990).
33. E. Batke, D. Heitmann, C.W. Tu, Phys. Rev. B **34**, 6951 (1986).
34. D.C. Tsui, S.J. Allen, R.A. Logan, A. Kamgar, and S.N. Coppersmith, Surface Science **73**, 419 (1978).
35. E. Batke, D. Heitmann, J.P. Kotthaus, and K. Ploog, Phys. Rev. Lett. **54**, 2367 (1985).
36. W.M. Que and G. Kircenow, Phys. Rev. B **39**, 5998 (1989).
37. V. Fock, Z. Phys. **47**, 446 (1928).
38. R.B. Dingle, Proc. R. Soc. London, Ser. A **211**, 500 (1952).
39. C.T. Lui, K. Nakamura and D.C. Tsui, Appl. Phys. Lett. **55**, 168 (1989).

41. C. Maxwell-Garnett, Philos. Trans. R. Soc. London **203**, 385 (1904).
42. J.W. Wu, P. Hawrylak, J.J. Quinn, Phys. Rev. Lett. **55**, 879 (1985).
43. B.A. Wilson, S.J. Allen, and D.C. Tsui, Phys. Rev. B **24**, 5887 (1981).
44. U. Merkt, M. Horst, T. Evelbauer, and J.P. Kotthaus, Phys. Rev. B **34**, 7234 (1986).
45. G.W. Bryant, Phys. Rev. Lett. **59**, 1140 (1987).
46. A.V. Chaplik, JETP Lett. **50**, 44 (1989).
47. L. Brey, N.F. Johnson, and B.I. Halperin, Phys. Rev. B **40**, 10647 (1989).
48. W. Kohn, Phys. Rev. **123**, 1242 (1961).
49. P.A. Maksym and T. Chakraborty, Phys. Rev. Lett. **65**, 108 (1990).
50. V. Gudmundsson and R.R. Gerhardts in: *High Magnetic Fields in Semiconductor Physics III*, edited by G. Landwehr, Springer Series in Solid State Sciences **101**, 348 (1990).

Chapter 2

Ballistic transport, and photo-response in a 1D channel

Parts of this work have been published in:

- J. Phys.: Condens. Matter **2**, 7247 (1990).

2.1 Introduction

After the observation of quantized conductance in a very narrow conducting channel, by van Wees *et al.* [1] and Wharam *et al.* [2] in 1988, the field of transport phenomena in nanoscale devices gained a lot of interest and became a "hot topic" in solid state physics [3,4].

These nanoscale structures, called quantum point contacts or split gates, are short and narrow constrictions (several 100 nm) of the order of the Fermi wavelength (λ_F) in a two-dimensional electron gas (2DEG). In the free electron approximation the Fermi wavelength of the conduction electrons can be calculated from $E_F = \hbar^2 k_F^2 / 2m^*$ (with E_F the Fermi energy, m^* the effective mass and using the Fermi wave vector $k_F = 2\pi/\lambda_F$). For the electron transport two characteristic length scales can be defined; the elastic mean free path l_e and inelastic mean free path l_ϕ. The first one defines the length scale on which the momentum of the electrons is conserved (determined by impurity scattering). The second defines the length scale on which the energy of the electrons is conserved (determined by electron-phonon and electron-electron scattering). The length l_ϕ increases as the temperature drops, while l_e is usually independent of the temperature. In high mobility semiconductors at low temperatures both lengths can be made larger than the dimensions of the constriction; this is called the ballistic regime. Scattering is then determined by the geometry of the device, and the mean free path merely gives the length scale on which ballistic transport can be realized.

When the Fermi wavelength is comparable to the size of the constriction in the ballistic regime, the classical description of diffusive transport is not sufficient. The wave-like nature of the electrons will become significant, and their energies become quantized due to the confinement potential in the constriction. This leads to the formation of one-dimensional (1D) subbands, characterized by free motion of the electrons in a single direction. As a result the density of states in the 1D channel is drastically changed from that in two dimensions, and this will in turn be reflected in the electronic properties.

The study of short and narrow constrictions followed the work on 1D wires of which the width W was smaller and the length L generally longer than l_e [5,6,7]. This means that the electrons can move between the boundaries of the channel without being scattered by impurities, but the motion in the direction along the channel is still diffusive. In this quasi-ballistic regime the transport properties are dominated by irregular interference effects related to the phase of the electrons [8]. Thornton *et al.* [5] first demonstrated the presence of quantum confinement from the magnetic depopulation of 1D subbands in a method described by Berggren *et al.* [9]. The problem of the interference effects was circumvented by the use of devices in which both W and L were smaller than the mean free path and the electron motion in both directions was ballistic. The quantum size effect of the confining potential was then directly observed as a quantization of the conductance in units of $2e^2/h$ [1,2].

The common starting point for producing nanoscale devices is the 2DEG in a GaAs-(Ga,Al)As heterostructures [10,11], although Si-based structures are also frequently used surface by the narrow potential well at the GaAs-(Ga,Al)As interface. Generally only the lowest 2D subband is occupied, and the density of states (DOS) is strictly 2D. Additional lateral confinement can be achieved via electrostatic depletion using metal gates on top of the sample surface or via chemical etching techniques [13,14]. The first method is generally preferred, because the dimensions of the constriction can than be tuned by the gate voltage.

In section 2.2, we will first introduce the devices used in this work and demonstrate the quantization of the conductance. In section 2.3, we present a study of the differential conductance of split gate devices under application of high bias voltages across the constriction. In this regime the transport properties are nonlinear and the differential conductance displays a quantization in half integer plateaux. The last section of this chapter is concerned with the photo-response of split gate devices under the application of far-infrared (FIR) radiation. In these experiments the nonlinear behaviour of the conductance leads to a novel rectifying effect of the applied high frequency electric field of the radiation.

2.2 The split gate device; quantization of the conductance

The layout of a split gate device used in our experiments is shown schematically in Fig. 2.1. Here we define the left hand contact as the source and the right hand contact as the drain, with respect to which a negative voltage is applied. The two terminal conductance of the device is measured between the source and drain as a function of increasingly negative gate voltage. The details of the device and measurement technique are given in section 2.3.1 below.

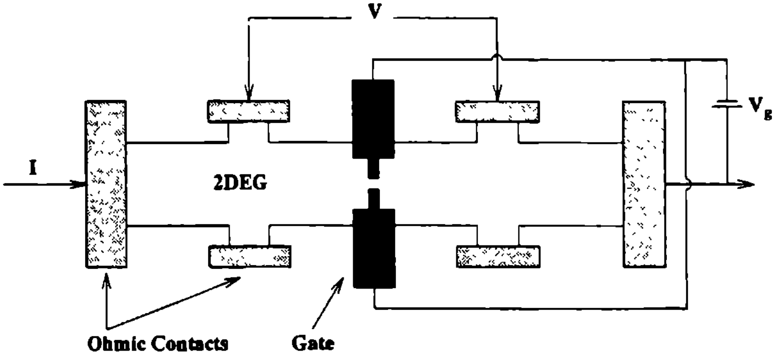

Figure 2.1 Schematic of the split gate device. The lightly shaded areas are the ohmic contacts connected to the 2DEG of the Hall bar geometry. The darkly shaded areas are the metallic gates on which a negative voltage with respect to the drain is applied. Upon depletion of the electrons beneath the gate, only a narrow conducting channel connecting the two wide 2DEG regions will remain.

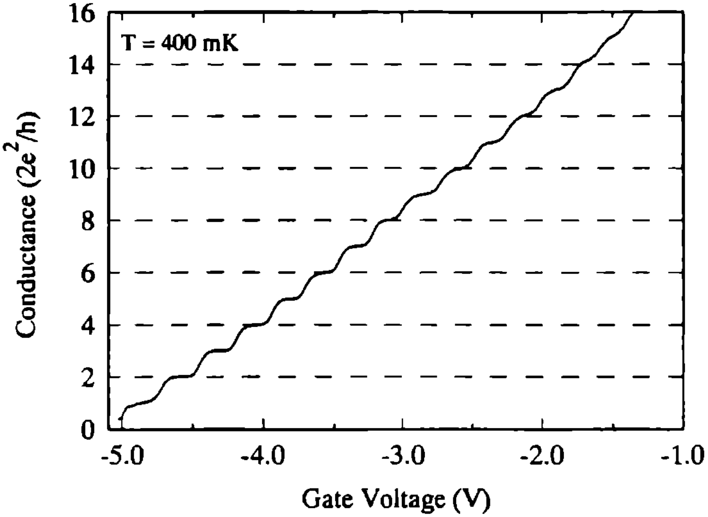

Figure 2.2 Two terminal source-drain conductance, in units of $(2e^2/h)$, of a split gate device as a function of the applied gate voltage. A large number of quantized plateaux are clearly visible.

Figure 2.2 shows the two terminal source-drain conductance as a function of gate voltage. In this experiment the source-drain bias voltage was kept as low as possible to avoid electron heating. The conductance is found to decrease in a sequence of 16 equidistant steps as a function of the gate voltage. At a gate voltage of ~ -5 V the conductance is virtually zero and channel is called to be pinched-off. The plateaux represent the conductance quantization of the split gate in units of $2e^2/h$, and demonstrates the well known result obtained by van Wees *et al.* [1], and Wharam *et al.* [2].

The quantization of the conductance can be most readily understood within the framework of a 1D subband picture. Application of a negative voltage on the gate will first deplete carriers form underneath its surface and so form a narrow channel in between two 2DEG reservoirs. For λ_F comparable to the width of the split gate, the energy in the channel will be quantized. As the gate voltage is decreased this channel will become narrower and simultaneously the number of carriers decreases due to the stronger confining potential. Hence, as a function of gate voltage, the 1D subbands will be pushed above the Fermi level, and simultaneously the 1D subband spacing will be increased. Every time that a 1D subband is depleted, the conductivity is reduced by an equal amount. Or equivalently, all the subbands are observed to carry an equal amount of current.

The explanation for this relation is adopted from Landauer [15]. In the ideal case the channel can be thought of as an electron waveguide connecting two 2DEG regions at different chemical potentials μ_s and μ_d. If the area of 2DEG regions is large, they become reservoirs in which all scattering is assumed to take place and the electronic motion approaches thermal equilibrium. A net current is injected into the channel within a range $\Delta\mu$ $(\mu_s - \mu_d)$ from source to drain into a number of 1D subbands or waveguide modes that can propagate at these energies. The dispersion relation, $E_i(k)$, of these 1D subbands can be expressed as,

$$E_i(k) = E_i + \frac{\hbar^2 k^2}{2m}. \tag{2.1}$$

Here k is the wave vector for propagation along the channel and E_i is the energy associated with the lateral confinement of the ith subband.

The current per unit energy interval injected into a subband is the product of the group velocity and the 1D density of states. The group velocity is $v_i = \mathrm{d}E_i(k)/\hbar \mathrm{d}k$, and the density of states for one velocity direction (including spin degeneracy) is $g_i = (\pi \mathrm{d}E_i(k)/\mathrm{d}k)^{-1}$. The contribution to the current from a single subband is then given by, $I_i = g_i e v_i \Delta\mu$. As the product of v_i and g_i is independent of both energy and subband index i, every subband carries an equal amount of current $I_i = (2e/h)\Delta\mu$. For n subbands below the Fermi energy the total current is

$$I = n(2e^2/h)\Delta V \tag{2.2}$$

(with $\Delta\mu = e\Delta V$ and ΔV the applied source-drain bias) and yields a conductance $G = I/\Delta V$ given by,

$$G = \frac{2e^2}{h} n. \tag{2.3}$$

This semiclassical deviation is supported by a general quantum mechanical formula based on a result due to Landauer [15,16]. In this formalism n is replaced by the trace $\mathrm{Tr}\ \mathbf{t}\mathbf{t}^\dagger \equiv \sum_{n,m=1}^{n} \mid t_{nm} \mid^2$, where $\mathbf{t}$ is the transmission matrix (with elements t_{nm}) of transmission amplitudes at the Fermi energy (from subband m at one reservoir to subband n at the other). In the absence of intersubband scattering , $\mid t_{nm} \mid^2 = \delta_{nm}$, and the conductor can be considered ideal. For this case, $\mathrm{Tr}\ \mathbf{t}\mathbf{t}^\dagger = n$, and the same result as Eq. 2.3 is obtained.

In the short explanation given above the details of the coupling between 2DEG and 1D channel have been totally neglected, moreover, the experimental shape of the constriction is far from that of a proper waveguide. For a fully satisfactory explanation more fundamental approaches have to be considered, which incorporate the detailed properties of electron waves entering and exiting the constriction [4,17,18,19].

2.3 Ballistic transport in one dimension: additional quantization produced by an electric field

The early measurements of which an example is shown in the previous section were performed at source-drain bias voltages, V_{sd}, much smaller than the characteristic energies of the device (Fermi energy and subband spacing). This can be expressed as $eV_{sd}/E_F \ll 1$. In this limit the current-voltage response of the device can be considered *linear*. In more recent work [20,21] the high bias voltage response of split gates have been studied, where

In this limit the current-voltage response is found to be strongly *nonlinear*. In the range of bias voltage $eV_{sd}/E_F \leq 1$, Kouwenhoven *et al.* [20] found the electron transport to be ballistic, and the nonlinear behaviour could be related to the unequal population of current carrying subbands for both velocity directions. In the extremely high bias regime, $eV_{sd}/E_F \gg 1$, and gate voltages close to pinch-off, Brown *et al.* [21] found evidence for negative differential resistance instabilities in the source-drain voltage characteristics. This was explained in terms of a deviation of the transmission coefficient of the channel from its ideal value of unity [22].

Glazman and Khaetskii [23] proposed a theoretical model, using a smoothly shaped potential to model the constriction (known as the adiabatic approach), for the high bias voltage response (in the regime $eV_{sd}/E_F \leq 1$). One of the predictions of this model was that, under the special condition of a symmetrically dropped bias voltage across the 1D channel, the differential conductance as a function of gate voltage should display quantized plateaux exactly in between the normally observed conductance plateaux. However, theoretical predictions for the same regime by Castano *et al.* [24], for a geometry in which the constriction changes abruptly from 2DEG to 1D channel, contradict with those of Glazman *et al.* with regard to the appearance of new plateaux.

In this section we present detailed results on the onset of nonlinear response, in which clear evidence is found for the appearance of new quantized plateaux in between the normally observed plateaux. As a consequence our results agree with the predictions set by Glazman *et al.* [23], and will be discussed in view of this model.

2.3.1 Experimental details and results

The split gate devices used in this work were fabricated at the Cavendish Laboratory of the University of Cambridge, and were defined on a MBE grown GaAs-(Ga,Al)As heterostructure of mobility $\mu > 1 \times 10^6$ cm^{2}V^{-1}s^{-1} and carrier density of 3×10^{11} cm^{-2} (after illumination with a red LED). These values imply an elastic scattering length in excess of 10 μm and a Fermi energy of 10 meV, resulting in a Fermi wavelength of approximately 50 nm. First, a standard mesa-etched Hall bar geometry was defined using wet etching. The split gate was then fabricated using electron beam lithography [25]. The lithographically defined dimensions of the gate opening were 0.3 μm by 0.3 μm, confirmed from SEM photographs of the gates, which were taken after all measurements had been performed.

A source-drain voltage can be applied across the split gate device in two ways: either by voltage biasing in a two-terminal differential conductance measurement or by current biasing in a four-terminal resistance measurement. Four-terminal current biasing measurements eliminate contact resistances and produce more accurate values of the quantized plateaux. However, it is preferable to use voltage biasing because the voltage across the device is independent of the resistance (and hence the gate voltage) of the 1D channel. All the subsequent data is shown in terms of two-terminal differential conductance $g = dI/dV_{sd}$ measured as a function of source-drain voltage V_{sd} and the gate voltage V_g. The applied source-drain voltage consisted of an *ac* and a *dc* component; the *ac* component was fixed at an amplitude of 0.1 mV with a frequency of 83 Hz, while the *dc* component was varied. Standard lock-in techniques were utilized for all measurements. Measurements were either taken in a dilution refrigerator at temperatures down to 30 mK at the University of Cambridge, or in a ^{3}He-insert at temperatures down to 400 mK at the University of Nijmegen. Both the contact resistances of the ohmic pads, and the 2DEG's on the two sides of the split gate device contribute a series resistance which is independent of the gate voltage. This resistance was subtracted from the raw data to give the two terminal conductance shown in the figures.

When a small magnetic field is applied perpendicular to the device it exerts a Lorentz force on the moving electron, thereby forcing it to move through the channel after scattering from an accidental impurity in or near the channel, hence making the electron transport more ideal [16]. This improves the quality of the plateaux considerably, therefore the measurements presented below were performed under application of a small (0.5 T) magnetic field.

The conductance of a device measured with a low source-drain voltage and no *dc* bias was shown in Fig. 2.2 in the previous section (for a different sample). With increasing V_{sd} extra plateaux are observed in the differential conductance characteristics as a function of gate voltage, as shown in Fig. 2.3. These plateaux are sample independent and were found with all samples studied. The new plateaux are half way between the normal plateaux to within an accuracy of a few percent.

In Fig. 2.3 we observe that the half integer plateaux first appear at $V_{sd} = 1.5$ mV in between the values of 7 and 8 times $2e^2/h$ for the normally observed integer plateaux. At increasingly higher V_{sd} new plateaux also start appearing in between lower values of normally quantized plateaux. Furthermore, at large V_{sd}, the new plateaux which first appeared at low V_{sd}, disappear again. We note that in between zero and the lowest quantized plateau there is an indication of a developing new plateau, however not at a half integer value, but somewhat below.

2.3.2 Discussion

The appearance of half integer plateaux in the conductance of a 1D ballistic channel at finite source-drain voltages is a conformation of the model proposed by Glazman and Khaetskii [23]. This model is based on the adiabatic approach for electron transport through a constriction [18]. In this approach they assumed the width W of the constriction to change gradually on the scale of the electron wavelength, and that the entrance and exit of the channel had a gradual taper from the 1D constriction to the 2DEG. Then it was found that no intersubband scattering occurred and that backscattering of entering or exiting electrons was strongly suppressed. In the language of waveguide transmission, one has then impedance-matched the constriction to the 2DEG. Although the split gate defining the constriction is square-like, calculations of the resulting electrostatic potential show [26,27], that the confining potential is very similar to a smooth saddle shape [16].

To describe the electron transport under large applied source-drain biases, we consider the problem in the following way [18,23]. The electrons entering the channel are

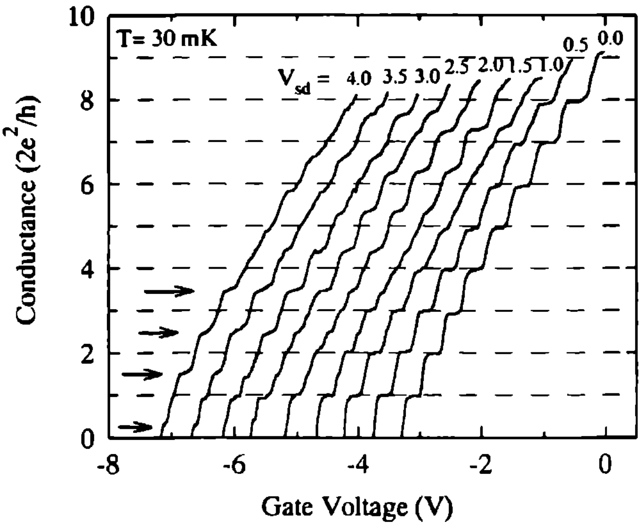

Figure 2.3 Differential conductance, in quantized units of $(2e^2/h)$, as a function of the gate voltage for different fixed values of the source-drain voltage V_{sd} (in mV), and at $B = 0.5$ T. Successive curves are offset horizontally by 0.2 V for clarity.

subject to a smoothly varying saddle-point potential. For n subbands below the Fermi level in the channel, the problem can be equivalently regraded as n channels in parallel, each with its own effective barrier height relative to that subband energy.

To determine the transport properties it is essential to consider how the voltage is dropped across the barrier. Therefore, we define β as the fraction of the voltage V_{sd} that is dropped between the source and the narrowest part of the constriction (assuming a vanishing electric field outside the constriction); then the electrochemical potentials at the source and drain can be defined as [20]

$$\begin{aligned} \mu_{\mathrm{s}} &= E_{\mathrm{F}} + \beta e V_{\mathrm{sd}} \qquad \text{and} &(2.4)\\ \mu_{\mathrm{d}} &= E_{\mathrm{F}} - (1-\beta) e V_{\mathrm{sd}}, &(2.5)\end{aligned}$$

respectively. Glazman and Khaetskii [23] assumed the source-drain voltage to be dropped symmetrically across the constriction, and so hereafter we shall take $\beta = 1/2$.

The energy reference level is taken such that the maximum of the 1D potential barrier, denoted by E_n for the nth subband, remains unaltered by the bias voltage. Then V_{sd} increases the chemical potential μ_{s} in the left hand side reservoir by $eV_{\mathrm{sd}}/2$ and reduces the chemical potential μ_{d} in the right hand reservoir by the same amount. Consequently, taking into account spin degeneracy, the current for each one-dimensional subband is given by

$$I = \frac{2e}{h} \int_{E_{\mathrm{F}}-eV_{\mathrm{sd}}/2}^{E_{\mathrm{F}}+eV_{\mathrm{sd}}/2} T(E)dE \tag{2.6}$$

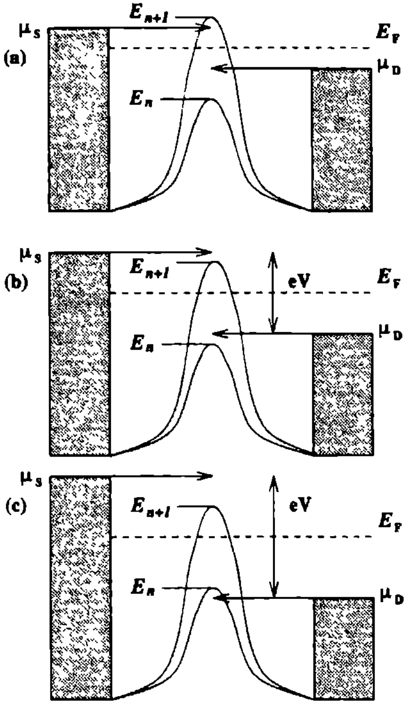

Figure 2.4 Schematic representation of the subbands and chemical potentials at the constriction for three different values of source-drain voltage. The curves represent the barriers due to the different 1D subbands (see text). (a) Shows the low bias case where the values of chemical potentials on each side of the split gate are in the same subband. (b) $n+1$ conducting channels from left to right and n conducting channels from right to left. (c) $n+1$ right going channels and $n-1$ left going channels.

where E_F is the chemical potential at zero bias. We approximate the transmission probability as one for the electrons with energy above the barrier and zero for energy below.

We can now calculate the current and the differential conductance through the constriction as a function of the applied source-drain voltage. Let us first consider values of eV_{sd} sufficiently small that the number of occupied subbands is unaltered, that is when μ_s and μ_d are both between E_n and E_{n+1} as shown in Fig. 2.4(a). Using Eq. 2.6 we can derive the current and the differential conductance to be

$$I = \left(2e^2/h\right) n V_{sd} \tag{2.7}$$

$$g = \mathrm{d}I/\mathrm{d}V_{sd} = \left(2e^2/h\right) n \tag{2.8}$$

where n is the number of occupied 1D subbands. This is the well known result obtained in section 2.2. If we now consider the case where the bias is increased to make the chemical potential μ_s rise above E_{n+1} with μ_d still between E_n and E_{n+1}, we have the situation shown in Fig. 2.4(b). The current in the $(n+1)$ channel is then given by

$$I_{n+1} = (2e/h)\left(E_F + eV_{sd}/2 - E_{n+1}\right) \tag{2.9}$$

with the contribution to the current coming from the other n channels still given by

$$g = \left(2e^2/h\right)\left(n + \frac{1}{2}\right). \tag{2.10}$$

Similarly it can be seen that when the bias causes the chemical potential μ_d to drop below E_n, with μ_s still in between E_n and E_{n+1}

$$g = \left(2e^2/h\right)\left(n - \frac{1}{2}\right) \tag{2.11}$$

when the bias satisfies the conditions in the above two cases, which occurs when there is one subband transporting current in only one direction, new quantized conductance plateaux are predicted. These will appear in between the normal plateaux resulting in steps in conductance e^2/h as opposed to the usual value of $(2e^2/h)$.

Eventually the bias voltage will be large enough that two subbands will be transporting current in one direction. We consider here explicitly the case in which μ_s is larger than E_{n+1} and μ_d is smaller than E_n this is depicted in Fig. 2.4(c). The current is now

$$\begin{aligned} I &= \frac{2e^2}{h} n V_{sd} + \frac{2e}{h}\left(E_F + eV_{sd}/2 - E_{n+1}\right) - \frac{2e}{h}\left(E_n - \left(E_F - eV_{sd}/2\right)\right) && (2.12) \\ g &= \left(2e^2/h\right) n && (2.13) \end{aligned}$$

The first term is the current for n channels as in Eq. 2.8, the second term reflects the increase in current due to the contributions of $(n+1)$ channels as in Eq. 2.9 and the final term is the decrease in contribution of the nth channel. The net result is a normal plateau value for the differential conductance.

On the basis of this simple model we expect to observe different regimes as the source-drain voltage is increased. In more detail, Glazman *et al.* [23] calculated, using a model-constriction, that the new plateaux are first expected to appear in between higher order plateaux, with their width increasing with V_{sd}. This behaviour is clearly observed in Fig. 2.3, with the new half integer plateaux first appearing in between the $n = 7$ and the $n = 8$ plateaux. For increasing source-drain voltage the new plateaux become better developed and also start appearing in between lower order plateaux. The fact that the plateaux appear at approximately half integer values justifies the assumption of the source-drain voltage being dropped symmetrically across the constriction. As the source-drain voltage is further increased we observe plateaux only at half integer values spaced by $2e^2/h$ differential conductance steps (Fig. 2.3; trace for $V_{sd} = 2.5$, 3.0, and 3.5 mV). This results from the chemical μ_s raising above E_{n+1} at a similar gate voltage as μ_d falls below E_n so producing a jump in the differential conductance of $2e^2/h$. A third regime becomes apparent at the highest values of source-drain voltage, where it appears that the integer plateaux may be returning. The new plateau which develops in between zero and the first quantized value, at the highest source-drain voltages in Fig. 2.3, is clearly below the half integer value. This is not an accidental observation: it has also been observed more clearly in a recent measurement by Patel *et al.* [28], however, the reason for this

In an ideal conductor the simple model above results in infinitely sharp steps in the conductance. However, in a quantum mechanical treatment, tunnelling of electrons just below and reflection of electrons just above the barrier will alter the transmission probability and effectively smear the steps at finite source-drain voltages [18,23,29]. This effect is observed in Fig. 2.3, where for increasing V_{sd} a smearing out of the plateaux is observed. This effect is largest for higher order plateaux which start to disappear at bias values as low as 3 mV. Lower order plateaux persist longer but eventually even these disappear.

From Fig. 2.3 and the model we can conclude that the appearance of the half integer plateaux depends critically at any particular gate voltage on the position of the chemical potential with respect to the 1D subbands. We can use this effect to extract the 1D subband spacing from the data. Figure 2.5 shows the differential conductance taken at fixed gate voltages when the source-drain bias is swept. This clearly shows the nonlinear regime is reached at varying biases depending on the gate voltage. When the conductance is initially at a plateau value (trace (h) in Fig. 2.5), the Fermi level is located midway between two adjacent subbands. Therefore, to shift the chemical potentials into the adjacent subbands and observe nonlinear conductance, a bias is needed which exactly equals the subband spacing. Away from a plateau (trace (k) in Fig. 2.5) the chemical potential is closer to one of the adjacent subbands and a lower bias is needed to see the same effects. Using this criteria subband spacings were extracted which are of the same magnitude as data obtained by other workers [20,30]. The half integer plateaux are also evident in the data of Fig. 2.5 as well as a small asymmetry between the positive and negative bias. This is a result of the way the gate voltage is biased relative to the 2DEG which results in an effective increase of the gate voltage for positive biases and so a decrease in the conductance. Similarly negative biases will lower the effective gate voltage with respect to the 2DEG and will increase the conductance.

The data show that the half integer plateaux first appear at low source-drain biases in between the higher index plateaux. This reflects the fact that for the corresponding gate voltages the channel is relatively wide and the 1D subbands are close together. As the gate voltage becomes more negative the channel becomes narrower and the energies of the 1D subbands move further apart. Then a larger source-drain voltage is needed to produce the new plateaux. A square well potential has subbands further apart at higher index n whereas a parabolic potential results in equally spaced values. No sign is seen in our data of an increase in the subband spacing with higher index indicating that a parabolic potential is better suited than a square well potential [9,30].

The high bias regime has also been studied when magnetic fields where applied perpendicular to the sample surface. The effect of a magnetic field on the 1D conductance has been extensively studied in the past [30,31], and is well explained by the Büttiker formalism in terms of reflection of edge states [16,32,33]. However, for our experiment it is only important to realize that the magnetic field quantizes the electron energies into Landau levels, thereby effectively increasing the 1D subband spacing proportional to the magnetic field. As a result the number of subbands below the Fermi level will be

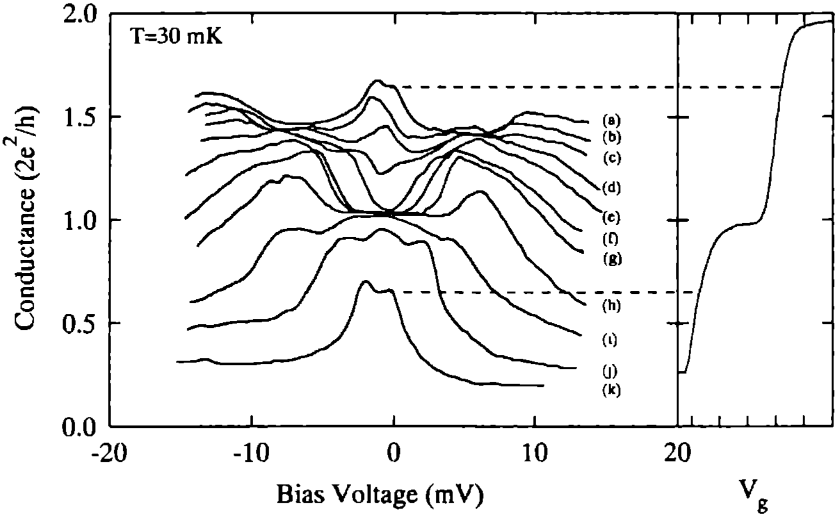

Figure 2.5 Differential conductance at fixed gate voltages as a function of the *dc* bias voltage. The traces are separated by equal increments of 50 mV in gate voltage: curve (a) has gate voltage -4.90 V and curve (k) -5.40 V. The right hand side of the figure displays the corresponding differential conductance measured with zero *dc* bias.

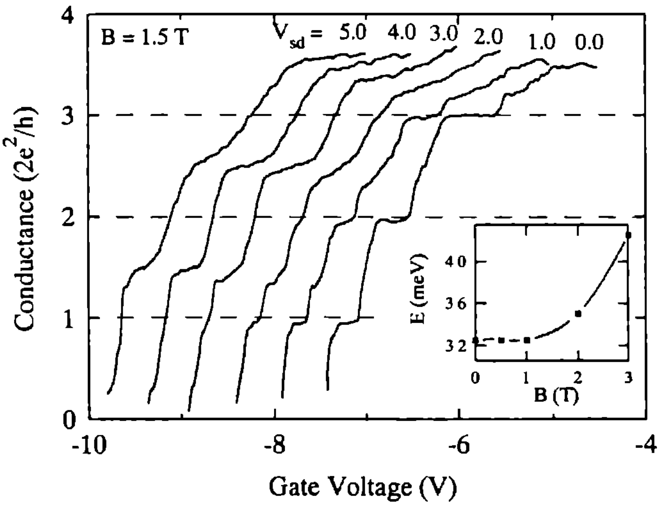

Figure 2.6 The differential conductance plotted as a function of the gate voltage in a magnetic field of 1.5 T. The *dc* source-drain voltage is indicated at the top of the curves (in mV). Values of the extracted subband spacings as a function of the

n the gate voltage sweep are observed. As a source-drain voltage is applied once again the half integer plateaux emerge and show the same behaviour as the zero magnetic field data. Even at 3 T we still see the appearance of half integer plateaux except that a higher bias is needed which directly reflects the increased 1D subband spacing due to the magnetic field. The subband spacings for different magnetic field values, extracted via this method are displayed in the inset of Fig. 2.6 and are in good agreement with the calculated values for an identical device in Ref. [30] (an extensive study of the subband spacings determined by this high bias technique has been performed by Patel *et al.* [28]).

2.3.3 Summary

We have observed well quantized half integer plateaux in the high bias regime of a ballistic split gate in zero magnetic field. These are described in terms of a model incorporating the effect of the bias voltage on the chemical potentials on the two sides of the 1D channel n the adiabatic regime. A smearing out of the plateaux is observed and is expected to be a result of the bias altering the transmission coefficient from the ideal values of one and zero. When a constant transverse magnetic field is applied the voltage bias response is unaltered with the half integer plateaux still appearing at quantized values. At the highest magnetic field of 3 T the bias required to see the half integer plateaux was observed to increase. Values of the subband spacing were extracted from this data and agreed with values obtained from modeling this type of structure.

2.4 Photo-response of a 1D channel

The application of radiation to "classical" point contacts (the precursor of quantum point contacts) is a well established technique, widely used to study the contact's fundamental properties [34,35]. A classical point contact is made by pressing a fine metal wire against a whisker of the same or different type of metal, thereby producing a constriction for the electron transport. When exposed to a radiation field, high frequency currents are generated across the contact by the antenna action of the wire. If the contact has a nonlinear current (I) voltage (V) characteristic, a *dc* voltage response is generated by rectification. Other types of junctions which exhibit nonlinear I-V characteristics, such as for example Josephson junctions [36] and resonant tunnelling barrier structures (RTBS) [37,38,39] also show rectifying behaviour, however the underlying mechanism responsible for the nonlinear behaviour is completely different for each case. In a classical point contact the nonlinearities are a result of inelastic electron-phonon scattering [40] which occur at typical energies of 30 meV.

In this section, we report the observation of a *dc* voltage response of a quantum point contact (QPC) under the application of high frequency FIR radiation, due to an entirely different mechanism. In both the classical and quantum point contact the electron transport is ballistic, however, the crucial difference is the Fermi wavelength which in a semiconductor is in the order of ~50 nm, in contrast to only ~0.5 nm in a metal. The that we observe in the *dc* voltage response as the conductance is varied. The oscillations line up with the steps in the quantized conductance of the QPC. As we will discuss, this novel effect can be explained as classical rectification of the high frequency electric field. The responsible nonlinear *I*-*V* characteristics are a result of the unequal population of velocity directions of the 1D subbands in the constriction which occurs on an energy scale of several meV (see previous section and Ref. [41]), thus directly reflecting the quantum mechanical nature of the QPC.

2.4.1 Experimental details and results

The quantum point contacts used for this work were fabricated at the University of Cambridge and were identical to the devices described in section 2.3.1, with the exception that the gate opening was 0.5 μm by 0.5 μm. The gate voltage response showed up to 16 plateaux in the conductance which is illustrative for its good quality (Fig. 2.2). The sample was mounted in an optical ^{3}He-insert. The device was current biased using a small *ac* current (83 Hz) superimposed on a *dc* current. Chopped unpolarized radiation (11 Hz chopping frequency) from a FIR laser was guided onto the device after passing through cold filters. The electric field was parallel to the sample surface. A photo-response (PR) signal is then detected between two voltage probes on either side of the split gate by using a lock-in amplifier tuned to the chopping frequency of the laser. A second lock-in, tuned to the *ac* current, was used to measure the differential resistance of the device simultaneously with the photo-response. The signal from a bolometer measuring the incident radiation was used to normalize the photo-response.

In Fig. 2.7 we show the resulting PR under application of laser light of energy $E_{\mathrm{FIR}} = 2.18$ meV. The upper curve was measured when no bias was applied; the lower curve was measured with a *dc* bias current of 75 nA fed through the device. The simultaneously measured conductances are also shown for comparison. These curves show the usual behaviour, indicating that the transport properties of the QPC are not significantly affected by the radiation. For increasingly negative gate voltages, where the point contact conductance exhibits quantized plateaux, we observe strong (positive) oscillations in V_{Det} (upper curve). The peaks in V_{Det} occur at gate voltages where the conductance of the point contact changes stepwise because of a change in the number of occupied 1D subbands. When a bias current is applied (lower curve) the peaks in V_{Det} transform into asymmetric oscillations, also going negative, with the largest signal appearing at the low conductance side of the transitions. The shift in V_{g} of the oscillations is also observed in the conductance curves, and is related to the gate voltage being applied with respect to the drain contact of the 2DEG, as was discussed in the previous section. Furthermore, we note that a small photo-voltage was already measured at zero gate voltage (subtracted from the data in Fig. 2.7) when no constriction is present, and the device corresponds to a homogeneous 2DEG. This photo-voltage is likely to be generated in the 2DEG contacts, which were not covered from FIR radiation. The magnitude of this voltage was independent of bias current, gate voltage, and only dependent on the applied laser power. Due to this background the absolute sign of the oscillations is some what arbitrary

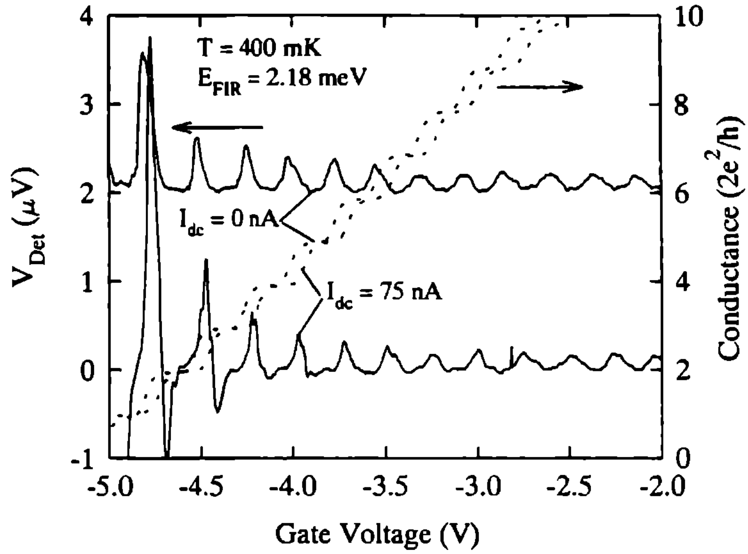

Figure 2.7 Photo-response (left hand scale) under applied FIR radiation of 2.18 meV. The upper curve with no *dc* bias applied is offset by 2 μV from the lower curve for an applied *dc* bias of 75 nA. The simultaneously measured conductances are also shown (right hand scale). The shift of the peak positions in the V_{Det} is equal to the shift in the conductance traces.

We studied this new type of PR for several different FIR energies in the range between 1 and 17.7 meV and *dc* bias currents between 0 and 250 nA. For all energies below 10 meV, oscillations in the gate voltage characteristics were observed. For $E_{FIR} = 1.8$ meV the sign of the peaks in V_{Det} (with no bias applied) was reversed with respect to the 2.18 meV response (compare Fig. 2.7 with the inset of Fig. 2.8(b)). For finite bias currents again positive and negative peaks were observed (Fig. 2.8(b)). It must be noted however that the laser power at 2.18 meV was approximately 5 times higher than at 1.8 meV. We did not perform a systematic study of the laser power dependence of the PR, but a general feature in the experiment was that for higher power laser lines the background and oscillating signal were increased.

In Fig. 2.8(a) and (b) the PR at two different energies are presented for increasingly larger *dc*-bias currents. The amplitude of the oscillations in this range only shows a minor increase, if compared with the change for low biases. The interesting feature in Fig. 2.8 is the appearance of splittings in the peaks for high biases, and is most clearly seen for $E_{FIR} = 2.18$ meV. The position of the splitting coincides with the appearance of half integer plateaux in the resistance (also shown for comparison). For lower biases an indication of this splitting is also present in the PR, although there is no sign for half integer plateaux in the resistance curve (lower trace in Fig. 2.8(a)). From this we can infer that the PR is very sensitive to the detailed characteristics of the channel conductivity.

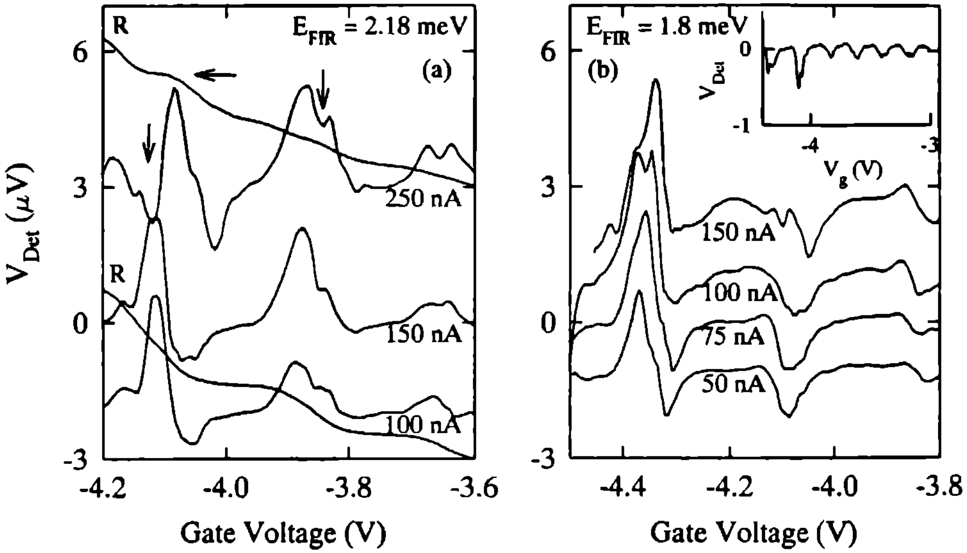

Figure 2.8 Photo-response as a function of gate voltage for several different *dc* bias currents with in (a) an energy of 2.18 meV and in (b) 1.8 meV. In (a) also two resistance curves are plotted, measured with 250 nA and 100 nA *dc* bias current. The inset in (b) shows the photo-response with no *dc* current bias applied for E_{FIR} = 1.8 meV. Note the sign reversal of the the peaks with respect to E_{FIR} = 2.18 meV in Fig. 2.7. All traces are offset for clarity.

2.4.2 Analysis of the experimental results

From the data presented it is obvious that the observed PR signal is closely related to the resistance of the constriction. Most importantly, the fact that the oscillations in the PR line up with the steps between quantized conductance plateaux of the point contact proves that the oscillatory phenomenon is a quantum-size effect associated with the ballistic transport through the constriction. In the case of a classical point contact (with λ_F much smaller than the constriction width), Van der Heijden *et al.* [35] showed that the *dc* voltage response is due to classical rectification of radiation caused by the nonlinear *I*-*V* characteristics. In analogy to this mechanism we propose detection via rectification in a quantum point contact. The nonlinearities responsible have been studied in detail in the previous section. There we found that the nonlinear behaviour is caused by an unequal number of populated 1D subbands for the two velocity directions of current. More specifically, we observed that the transport properties are nonlinear at the steps between quantized plateaux, and linear up to considerably high source-drain voltages when the conductance is quantized, thus commensurate with the observed oscillatory PR signal.

The rectification mechanism can be explained as follows [35]. When exposed to a radiation field, high frequency currents are generated across the contact. The nonlinear I-V characteristics of this contact can be expressed as a series expansion, in which only even terms will give a *dc* voltage after time integration over one frequency cycle. If the junction is current controlled, V_{Det} is given by,

$$V_{\mathrm{Det}} = \frac{1}{4}\frac{d^2V}{dI^2}i_0, \tag{2.14}$$

where the current through the channel is assumed to be modulated as $I = I_0 + i_0 cos\omega t$. I_0 is the *dc* bias current and ω the angular frequency of the radiation. Thus the laser detected voltage is directly proportional to the second derivative of the I-V curves as a function of the source-drain voltage.

Measurements of the second derivative have not been performed on this particular device, but in Fig. 2.5 of the previous section the dI/dV curves were presented on another device. From these curves we can calculate the second derivatives, which are presented in Fig. 2.9. The nonlinear behaviour of point contacts is not expected to change drastically for different samples, because the underlying mechanism is governed by the 1D subbands.

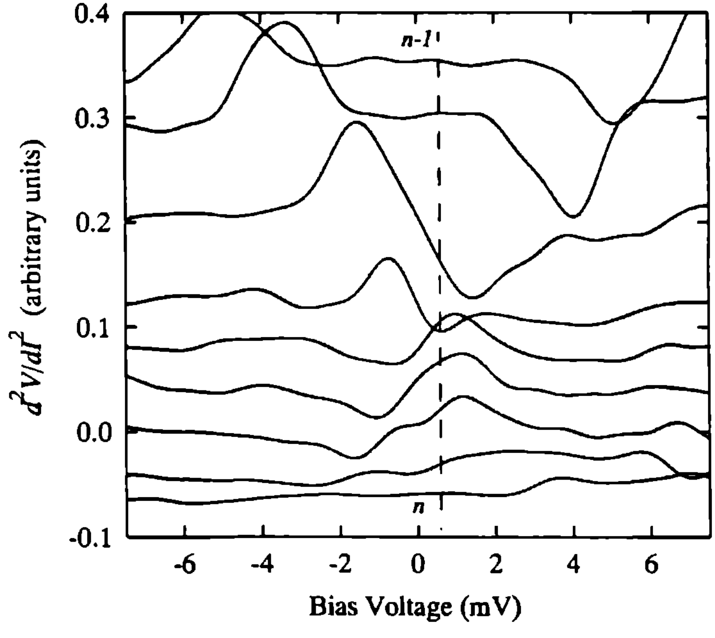

Figure 2.9 Second derivative defined by $d^2V/dI^2 = RdR/dV$ as a function of bias voltage for different values of gate voltage (calculated from data such as displayed in Fig. 2.5). The lowest curve corresponds to a conductance of $n2e^2/h$ and the upper curve to $(n-1)2e^2/h$ (at zero *dc* bias). The curves are offset for clarity. The dashed line is a guide to the eye.

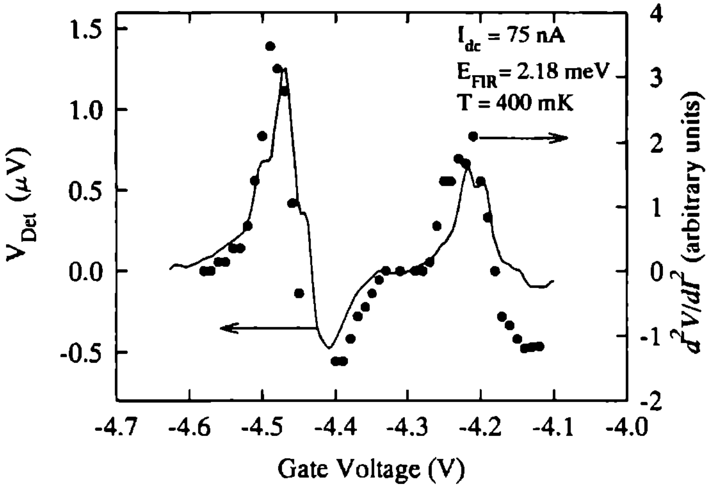

Figure 2.10 Measured PR signal from Fig. 2.7 for an applied bias current of 75 nA and calculated second derivative as a function of gate voltage.

Furthermore, this is justified by observation of half integer plateaux at nearly the same bias conditions for many different samples [28]. A useful measure for the nonlinearity of the I-V characteristics is the current sensitivity S:

$$S = \frac{d^2V/dI^2}{(dV/dI)^2} = \frac{d^2I/dV^2}{dI/dV}. \qquad (2.15)$$

Typical values for S at optimum bias voltage for the lowest order transition $n = 1$ are of the order of 50 V^{-1}. This value is about 5 times that of a classical point contact [34].

The expected PR from Eq. 2.14, as a function of gate voltage, can now be reconstructed from the second derivative curves such as displayed in Fig. 2.9 as a function of source-drain voltage. We use a restricted region of gate voltage because the source-drain voltage generated by the bias current is then approximately constant. We note that the behaviour of the second derivative is the same for the other transitions [28]. The vertical dashed line in Fig. 2.9 corresponds to a bias current of 75 nA. In Fig. 2.10 the values of the second derivative (points) and the measured PR (solid curve) are plotted simultaneously. Comparing the PR and the second derivative in Fig. 2.10 it is immediately seen that the correspondence in shape and position of the oscillations is quite reasonable for this region of gate voltage. This demonstrates the correctness of our understanding of the quantum mechanical origin of the oscillating PR signal in the experiment.

Increasing the source-drain bias corresponds in Fig. 2.9 to shifting the dashed line further to the right. As was found in the experiment (Fig. 2.8) this results in an increase of the amplitude of the oscillations in the PR. However, the increase of the amplitude of the PR as a function of bias will generally not be linear since it is related to the change in second derivative rather then the bias change.

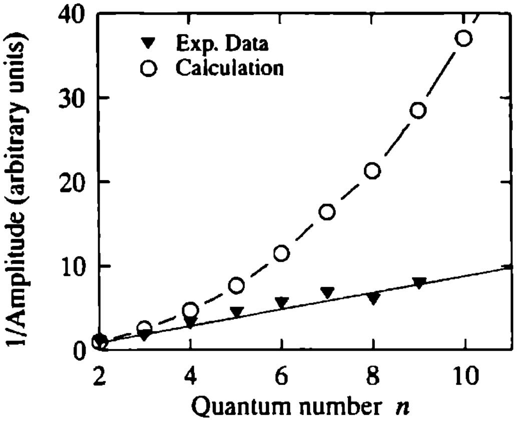

Figure 2.11 Inverse of the normalized amplitude versus quantum number n. ▼ : determined from experiment for $E_{\text{FIR}} = 2.18$ meV and $I_{dc} = 0$ nA. ○ : determined from a bolometric heating model calculation discussed in Sec. 2.4.3

In the experiment a PR was observed at zero bias (Fig. 2.7 upper trace and inset Fig. 2.8), which in terms of Eq. 2.14, implies that a finite second derivative must be present at zero bias. Inspection of Fig. 2.5 shows that the base lines of the curves are all tilted by the same amount, due to the fact that the gate is biased versus one of the current carrying contacts, as discussed before. For the curves at the middle of the transition between quantized plateaux this implies that the second derivative is finite at zero bias. Therefore, exclusively positive (or negative) peaks in the PR should be present for these gate voltages, which fits the experimental data.

In Fig. 2.11 the inverse of the amplitude, normalized to the maximum amplitude of the PR at zero bias of Fig. 2.7, is shown as a function of the corresponding quantum number n. Here n is defined by the transition in resistance from the n subband to the $n-1$ subband. The circles in Fig. 2.11 correspond to the results of a model calculation discussed in Sec. 2.4.3 below. The experimental data (at zero bias) show a linear dependence on the quantum number n. This directly implies that the amplitude of the oscillations is quantized. At non-zero bias the inverse amplitude starts to deviate from the linear curve and the quantization is lost. The result follows naturally from the second derivative where $d^2V/dI^2 = RdR/dV$; R is quantized as a function of the gate voltage and dR/dV is equal and non-zero at the transitions, as discussed above. For non-zero bias this is no longer valid as dR/dV will become a function of the gate voltage. Furthermore, the sign reversal for high power laser energies in a limited range of *dc* bias currents, could be caused by the effect of overmodulation [34]. In this case the high frequency voltage swing across the constriction becomes larger than the structure in the dI/dV curves around zero bias and could imply a polarity change.

The appearance of a splitting of the peaks in the PR in Fig. 2.8 for increasing *dc* biases constitutes a further confirmation of the rectification model. The dI/dV curves in

Fig. 2.5 show a flattening at half integer values of the conductance for increasing bias, and correspondingly a change in the second derivative in Fig. 2.9 is observed. The fact that the splitting is already observed at biases for which in the resistance no half integer plateaux are present, confirms the assumption of a considerable voltage swing across the channel.

2.4.3 Bolometric heating effects

Among the problems in assessing the rectification process often encountered in experiments are spurious signals due to thermo-electric and bolometric heating effects. The thermo-power of a quantum point contact has been predicted by Streda [42] to oscillate as the number of 1D subbands in the point contact is changed by the gate voltage. In addition, he derived that the local maxima of these oscillations would be quantized. These predictions have been confirmed by Molenkamp and coworkers [43], who observed oscillations in the transverse voltage across a quantum point contact when heating one side with a large *dc* current. The oscillating nature and quantized amplitude observed in our experiment do show a superficial similarity with those predicted for the thermo-power. However, if thermo-power is the origin, it would imply a FIR-induced temperature difference of at least 0.3 K [42] across the constriction. This is a condition which is hard to realize in practice since the device geometry is symmetric and the orifice of the cone at the end of the light pipe above the sample is comparable to the total size of the device [44].

The second effect, bolometric heating of the electron gas, is well known from photo-conductivity measurements on 2DEG systems [45,46,47,48] (although not rigorously understood). These photo-conductivity experiments on 2DEG systems in magnetic field showed non-resonant oscillations when the Fermi level passes through the Landau levels and so reflected the Shubnikov-de Haas oscillations in the resistance. A similar mechanism might occur as well in our experiment, and could contribute a photo-conductivity signal to the measured PR. Below we will estimate the importance of this effect.

A treatment of the non-resonant absorption of radiation by free carriers is quite involved [49], however, here we will use a simplified view of the mechanism. We will assume that absorption of FIR radiation leads to a non-uniform distribution of electrons over the available states. Electron-electron scattering will probably thermalize this distribution so that the system can be characterized with an effective electron temperature [50]. As the resistance is temperature dependent, one simply measures a signal proportional to $dR/dT \propto dR/dI_{\mathrm{FIR}}$, with I_{FIR} the intensity of the FIR radiation. In a photo-conductivity experiment where the PR is measured via a lock-in detector tuned to the chopping frequency of the laser, V_{Det} can be expressed as,

$$V_{\mathrm{Det}} \propto (R(T_{\mathrm{FIR}}) - R(T_0)) I_{\mathrm{bias}}, \tag{2.16}$$

with I_{bias} the applied bias current and $R(T_0)$ the resistance without FIR radiation (this is actually the principle of the bolometric technique used throughout this thesis to detect FIR radiation).

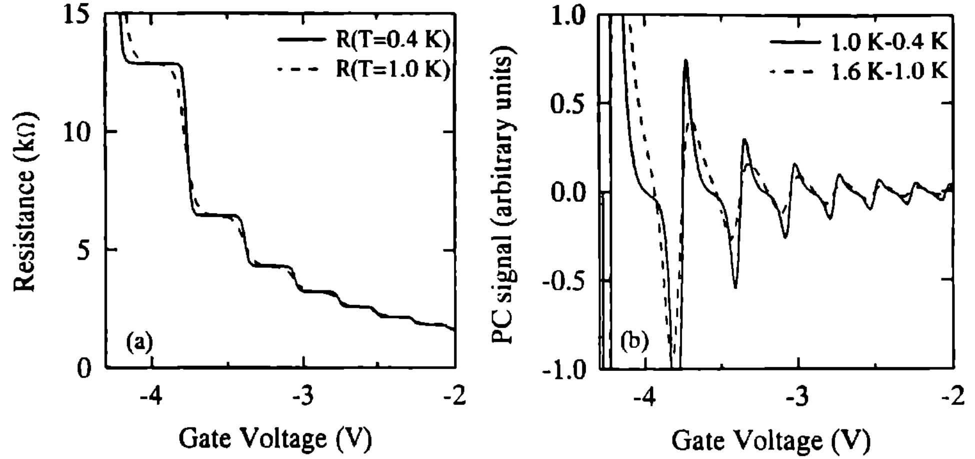

Figure 2.12 (a) Resistance as a function of gate voltage for two different temperatures calculated from Eq. 2.18. (b) Resulting photo-conductivity signal as a function of gate voltage. The temperatures used are listed in the figure.

The effect of temperature on the resistance of a ballistic 1D channel has been considered theoretically by Bagwell and Orlando [51]. They derived a generalized form of the Landauer equation by incorporating the energy averaging around the Fermi level at finite temperatures. The temperature dependent resistance in this situation can be described as,

$$R(T) = \frac{h}{2e^2}\frac{1}{n(T)}, \qquad \text{with} \qquad (2.17)$$

$$n(T) = \sum_{i=1}^{n} \int_0^\infty \frac{df(E,T)}{dE} T_i(E)dE. \qquad (2.18)$$

Here the convolution is taken of the (assumed) temperature independent transmission coefficient $T_i(E)$ and df/dE, which is just the standard thermal broading of the conductance (with f the Fermi Dirac distribution function defined as: $f = \left[1 + \exp\left(\frac{E-E_F}{k_B T}\right)\right]^{-1}$.

First the temperature dependent channel resistance is calculated using Eq. 2.18 for two different temperatures. For the transmission probability $T(E)$ the definition from Ref. [43] is used. The results of the calculations are shown in Fig. 2.12(a). The photo-conductivity signal should then (via Eq. 2.16) be proportional to the resistance difference of these two curves, which is depicted in Fig. 2.12(b). The results in Fig. 2.12(b) imply an oscillating signal, which is clearly more symmetric than observed in the experiment (see *e.g.* Fig. 2.7 lower curve). A more fundamental deviation from the experiments is the fact that Eq. 2.16 implies zero photo-conductivity signal at zero bias current. If an accidental small current would have been present in the experiment it is still contradicting with the calculations, because at zero bias exclusively positive oscillations are observed (*c.f.* Fig. 2.7). For increasing current bias the PR data does not suggest a simple linear dependence, as would be expected from Eq. 2.16. Also the sign reversal of the oscillations, between 2.18 and 1.8 meV at zero and low biases, can not be understood with the simple model presented here. The inverse amplitude determined from the calculations is also plotted in Fig. 2.11 (open circles). It is seen that the calculated amplitude lacks the quantized behaviour of the data. This result is independent of the temperatures used.

2.4.4 Discussion

From the above analysis we conclude that the photo-response is dominated by rectification. At finite source-drain biases, heating could in principle contribute to the observed response, however, the asymmetry of the oscillations and the dependence of the amplitude on the bias suggest that this contribution can only be of minor magnitude.

The presence of rectifying behaviour in a ballistic 1D channel exhibiting quantized conductance is entirely new and implies many interesting applications for both fundamental and technological studies. At this point it is of interest to compare the rectifying mechanism in a quantum point contact more closely with other devices, exhibiting the same behaviour, such as classical point contacts and RTBS's. Equation 2.14 implies that for classical rectification, the high frequency response is proportional to the second derivative of the I-V curves. Hence, classical rectification is independent of the frequency (in the limit of low radiation power levels, for which no overmodulation occurs). Based on extensive past experience it is well established that a change from classical to quantum detection occurs when the nonlinearity in the I-V curves become large on a voltage scale comparable to the radiation energy ($\hbar\omega/e$). This quantum detection is characterized by the observation that the high frequency response is energy dependent. For this regime it was shown that Eq. 2.15 for the current sensitivity of the rectifier can be redefined as [35,52],

$$S_q = -\frac{e}{\hbar\omega}\left[\frac{I_{dc}(V_0+\hbar\omega) - 2I_{dc}(V_0) - I_{dc}(V_0-\hbar\omega)}{I_{dc}(V_0+\hbar\omega) - I_{dc}(V_0-\hbar\omega)}\right] \tag{2.19}$$

where I_{dc} is the current without applied radiation, V_0 is the voltage bias, and $\hbar\omega$ the photon energy. The high frequency response is thus determined by three points on the I-V characteristic: at V_0 and $V_0 \pm \hbar\omega$. Whenever the resistance varies considerably on a voltage scale compared to $\hbar\omega$, the response according to the quantum mechanical model of Eq. 2.19 may differ considerably from the classical expression of Eq. 2.15. From Eq. 2.19 it follows that S_q is always smaller than $e/\hbar\omega$, corresponding to a quantum efficiency of unity (one electron per absorbed photon). Thus, when S in Eq. 2.15 approaches $e/\hbar\omega$, quantum detection might be expected. Equation 2.19 was first derived by Tucker *et al.* [52] for nonlinear tunnelling devices. However, van der Heijden *et al.* [34] experimentally proved that quantum detection is also possible in a classical ballistic point contact, without a tunnel barrier. Thus a ballistic point contact is similar in many respects to a tunnel junction, however, with tunnelling probability equal to unity. It is important to note that quantum detection implies that the phase of the electrons should be maintained during *al.* [39] for a RTBS with a nonlinear *I*-*V* characteristic clearly in the quantum limit. However, the response lacked energy dependence, due to the loss of phase coherence during tunnelling. For a ballistic quantum point contact with both l_e and l_ϕ larger than the constriction dimensions, phase coherence is implicit.

The data presented in this study were measured up to the last transition in the conductance, for which we found $S = 50\ \mathrm{V}^{-1}$. In terms of S_q this yields, for an energy of 2.18 meV, a value of $0.1e/\hbar\omega$. Clearly, we are in the regime where classical rectification applies for the energies studied in our experiment. If the gate voltage is increased beyond pinch-off, the conductance of the channel is virtually zero (except for a small leakage current through the gate). When the source-drain bias is increased to a certain value (dependent on the gate voltage), the chemical potential in the drain is lifted above the barrier, and one velocity direction of the lowest subband will switch into conductance [20]. At this point the nonlinearity in the *I*-*V* characteristic is dramatically increased, and S_q is close to $e/\hbar\omega$ (limited by the amount of leakage current). In this regime, quantum detection should be feasible if the electron transport remains ballistic. The experiments in the previous section show that this will indeed be the case for the range of source-drain biases needed to drive the transport nonlinear.

A last point of consideration involves the high frequency detection limit of a quantum point contact. A very fundamental limitation based on a classical argument is that the phase of the high frequency field should not change during the passage of electrons through the constriction region. However, the explanation of quantized conductance is based on a quantum mechanical description of the wave-like nature of electrons, which in essence is non-local. The classical limit can be estimated from the transit time, and is given by $\omega \leq v_\mathrm{F}/L$, with v_F the Fermi velocity and L the length of the constriction. For typical values of v_F and L this corresponds to a frequency in the range of $10^{12} - 10^{13}$ Hz. This is a rather low value if compared with metal point contacts and RTBS's. This is due on the one hand to the low Fermi velocity in comparison to a metal and on the other hand to the relatively long constriction length in comparison with the barrier widths of RTBS's. This limit might explain the absence of oscillations in the PR above energies of 10 meV (2.5 THz), although in this regime, a poor coupling of radiation to the device could also account for this. Nonetheless, the well defined ballistic transport properties of quantum confined devices could offer an excellent system to study such problems in more detail.

2.4.5 Summary

We have for the first time studied the FIR photo-response of a ballistic quantum point contact. Clear effects are observed which indicate that the dominating mechanism in the response is the classical rectification of the applied high frequency electric field. This rectification is generated by the strong nonlinear current voltage characteristics at the transition between quantized resistance plateaux, which are the result of an unequal number of populated 1D subbands for the two opposite directions of current in the channel. We estimate that quantum detection should be feasible which can in principle imply many interesting applications for studying the fundamental properties of ballistic charge transport at ultra high frequencies in quantum confined electron devices.

References

1. B.J. van Wees, H. van Houten, C.W.J. Beenakker, J.G. Williamson, L.P. Kouwenhoven, D. van der Marel, and C.T. Foxon, Phys. Rev. Lett. **60**, 848 (1988).
2. D.A. Wharam, T.J. Thornton, R. Newbury, M. Pepper, H. Ahmed, J.E.F. Frost, D.G. Hasko, D.A. Ritchie, D.C. Peacock, and G.A.C. Jones, J. Phys. C: Solid State Phys. **21**, 209 (1988).
3. C.W.J. Beenakker and H. van Houten, Solid State Physics **44**, edited by H. Ehrenreich and D. Turnbull, (Academic Press, Boston, 1991).
4. For a review see *Nanostructured Systems*, edited by M.A. Reed, Semiconductors and Semimetals **35** (Academic Press Inc.) (1992).
5. T.J. Thornton, M. Pepper, H. Ahmed, D. Andrews, and G.J. Davies, Phys. Rev. Lett. **56**, 1198 (1986).
6. M.L. Roukes, A. Scherer, S.J. Allen, H.G. Graighead, R.M. Ruthen, E. Beebe, and J.P. Harbison, Phys. Rev. Lett. **59**, 3011 (1987).
7. K. Ismail, D.A. Antoniadis, and H.I. Smith, Appl. Phys. Lett. **54**, 1130 (1989).
8. P.A. Lee, A.D. Stone, and H. Fukuyama, Phys. Rev. B **35**, 1039 (1987).
9. K.F. Berggren, T.J. Thornton, D.J. Newson, and M. Pepper, Phys. Rev. Lett. **57**, 1769 (1986).
10. T. Ando, A.B. Fowler, and F. Stone, Rev. Mod. Phys. **54**, 437 (1982).
11. J.J. Harris, J.A. Pals, and R. Woltjer, Rep. Mod. Phys. **52**, 1217 (1989).
12. J.R. Gao, C. de Graaf, J. Caro, S. Radelaar, M. Offenberg, V. Lauer, J. Singleton, T.J.B.M. Janssen, and J.A.A.J. Perenboom, Phys. Rev. B **41**, 12315 (1990).
13. *Granular Nanoelectronics*, edited by D.K. Ferry, (Plenum Press, New York, 1991).
14. *Nanostructure Physics and Fabrication*, edited by M.A. Reed and W.P. Kirk, (Academic Press, Boston, 1989).
15. R. Landauer, IBM J. Res. Dev. **1**, 223 (1957).
16. M. Büttiker, Phys. Rev. B **38**, 9375 (1988), and Phys. Rev. B **41**, 7906 (1990).
17. Y. Imry in: *Directions in Condensed Matter Physics*, Vol. 1, edited by G. Grinstein and G. Mazenko, (World Scientific Publishing Co., Singapore, 1986).
18. L.I. Glazman, G.B. Lesovik, D.E. Khmel'nitskii, and R.I. Shekter, JEPT Lett. **48**, 239 (1988).
19. A.D. Stone and A. Szafer, IBM J. Res. Dev. **32**, 384 (1988).
20. L.P. Kouwenhoven, B.J. van Wees, C.P.J.M. Harmans, J.G. Williamson, H. van Houten, C.W.J. Beenakker, C.T. Foxon, and J.J. Harris, Phys. Rev. B **39**, 8040 (1989).
21. R.J. Brown, M.J. Kelly, M. Pepper, H. Ahmed, D.G. Hasko, D.C. Peacock, J.E.F. Frost, D.A. Ritchie, and G.A.C. Jones, J. Phys.: Condens. Matter **1**, 6285 (1989).
22. M.J. Kelly, J. Phys.; Condens. Matter **1**, 7643 (1989).

24. E. Castano and C. Kirczenow, Phys. Rev. B **41**, 3874 (1990).
25. D.A. Wharam, Ph.D. thesis, University of Cambridge (1989), unpublished.
26. J.H. Davies, unpublished.
27. A. Kumar, S.E. Laux, and F. Stern, Appl. Phys. Lett. **54**, 1270 (1989).
28. N.K. Patel, J.T. Nicholls, L. Martin-Moreno, M. Pepper, J.E.F. Frost, D.A. Ritchie, and G.A.C. Jones, Phys. Rev. B **44**, 13549 (1991).
29. K.B. Efetov, J. Phys.: Condens. Matter **1**, 5535 (1989).
30. D.A. Wharam, U. Ekenberg, M. Pepper, D.G. Hasko, H. Ahmed, J.E.F. Frost, D.A. Ritchie, D.C. Peacock, and G.A.C. Jones, Phys. Rev. B **39**, 6283 (1989).
31. B.J. van Wees, L.P. Kouwenhoven, H. van Houten, C.W.J. Beenakker, J.E. Mooij, C.T. Foxon, and J.J. Harris, Phys. Rev. B **38**, 3625 (1988).
32. R.J. Brown, C.J. Smith, M. Pepper, M.J. Kelly, R. Newbury, H. Ahmed, D.G. Hasko, D.C. Peacock, J.E.F. Frost, D.A. Ritchie, and G.A.C. Jones, J. Phys.: Condens. Matter **1**, 6291 (1989).
33. B.R. Snell, P.H. Benton, P.C. Main, A. Neves, J.R. Owers-Bradley, L. Eaves, M. Henini, O.H. Hughes, S.P. Beaumont, and C.D.W. Wilkinson, J. Phys.: Condens. Matter **1**, 7499 (1989).
34. R.W. van der Heijden, Ph.D. thesis, University of Nijmegen (1982), unpublished.
35. R.W. van der Heijden, A.G.M. Janssen, J.H.M. Stoelinga, H.M. Swartjes, and P. Wyder, Appl. Phys. Lett. **37**, 245 (1980).
36. P.L. Richards in: *Semiconductors and Semimetals* **12**, edited by R.K. Willardson and A.C. Beer, (Academic, New York, 1977) p. 395.
37. T.C.L.G. Sollner, W.D. Goodhue, P.E. Tannerwald, C.D. Parker, and D.D. Peck, Appl. Phys. Lett. **43**, 586 (1983).
38. E.R. Brown, T.C.L.G. Sollner, C.D. Parker, W.D. Goodhue, and C.L. Chen. Appl. Phys. Lett. **55**, 1777 (1989).
39. V.A. Chitta, R.E.M. de Bekker, J.C. Maan, S.J. Hawksworth, J.M. Chamberlain, H. Henini, and G. Hill, Semicond. Science and Techn. **7**, 432 (1992).
40. A.G.M. Janssen, F.M. Mueller, and P. Wyder, Phys. Rev. B **16**, 1325 (1977).
41. N.K. Patel, L. Martin-Moreno, M. Pepper, R. Newbury, J.E.F. Frost, D.A. Ritchie, G.A.C. Jones, T.J.B.M. Janssen, J. Singleton, and J.A.A.J. Perenboom, J.Phys.:Condens. Matter **2**, 7247 (1990).
42. P. Streda, J. Phys.: Condens. Matter, **1**, 1052 (1989).
43. L.W. Molenkamp, H. van Houten, C.W.J. Beenakker, R. Eppenga, and C.T. Foxon, Phys. Rev. Lett. **65**, 1052 (1990).
44. B. Tieke, private communication.
45. J.C. Maan, Th. Englert, D.C. Tsui, and A.C. Gossard, Appl. Phys. Lett. **40**, 609 (1982).
46. R.E. Horstmann, E.J. v.d. Broek, J. Woltjer, R.W. van der Heijden, G.L.J.A. Rikken, H. Sigg, P.M. Frijlink, J. Maluenda, and J. Hallais, Solid State Commun. **50**, 753 (1984).
47. F. Thiele, E. Batke, J.P. Kotthaus, V. Dolgopolov, V.N. Ovsyuk, G. Gusev, G. Weimann, and W. Schlapp, Solid State Electron, **32**, 1503 (1989).

48. D. Stein, G. Ebert, and K. von Klitzing, Surface Science **142**, 406 (1984).
49. See *e.g.* K. Seeger in: *Semiconductor Physics*, Springer Series in Solid State Sciences **40**, 343 (1985).
50. T. Ando, Z. Phys. B **24**, 33 (1976).
51. P.F. Bagwell and T.P. Orlando, Phys. Rev. B **40**, 1456 (1989).
52. J.R. Tucker and M.F. Millea, Appl. Phys. Lett. **33**, 611 (1978).

Chapter 3

Cyclotron resonance of high mobility GaAs-(Ga,Al)As (311) 2D hole gases

---

Parts of this work have been published in:

- Semicond. Sci. Technol. **8**, 1465 (1993).

3.1 Introduction

The key differences between two-dimensional hole gases (2DHG's) and two-dimensional electron gases (2DEG's) are that the former have much higher effective masses and exhibit greater subband anisotropy. In addition, the electron-phonon interaction in 2DHG systems is rather stronger than in the companion electron gas. Until recently, the general quality of available 2DHG GaAs-(Ga,Al)As material (largely grown onto (100) surface substrates) has been rather poor. As a consequence, the exploration of effective masses and valence band anisotropy, using the proven technique of cyclotron resonance (CR) spectroscopy in the far infrared (FIR), have not been possible. Recent advances in growth procedures [1] has enabled very high mobility 2DHG layers to be produced by growth n non-conventional directions (*e.g.* onto the (311)A plane). Using this technique, hole mobilities exceeding 300,000 cm^{2}V^{-1}s^{-1} at low temperatures have been achieved [2], and transport studies [3,4] in both low-and high-density 2DHG samples have revealed fractional quantum Hall states and indications for a magnetically-induced Wigner solid.

The valence band structure in GaAs-(Ga,Al)As quantum well (QW) systems exhibits a richness and complexity even for the high symmetry plane (100) [5]. For layers grown onto the lower symmetry (311)A direction, magnetotunnelling spectroscopy studies [6] and calculations [7,8] of the valence band anisotropy in quantum wells indicate an even greater degree of mixing leading to "camel's back" behaviour of certain valence subbands. A knowledge of hole masses in such QW systems remains of practical importance in view of the dependence of the threshold current required for population inversion in QW lasers on densities of states and therefore on the effective mass [9].

In the case of 2DHG heterostructure systems, a triangular function may be used to approximate the confining potential, and the absence of inversion symmetry for this potential leads to the lifting of the Kramers' degeneracy for each subband [10]. Several early calculations of the subbands and Landau levels for the 2DHG at the GaAs-(Ga,Al)As interface have been reported [11,12]. The most complete [13] utilizes a fully self-consistent treatment which provides theoretical evidence for the strongly non-linear magnetic field dependence of the Landau level energies but which does not invoke the many-body effects which had been considered by previous workers. These calculations [13] have been reported only for the high symmetry (100) direction, and have generally used an axial approximation which introduces a cylindrical symmetry into the 4×4 Luttinger Hamiltonian. Extension of these calculations to the lower symmetry (311) direction represents a considerable complication, since the axial approximation cannot be made for the lower symmetry Hamiltonian.

Several early experimental CR studies have been reported for the (100) direction GaAs-(Ga,Al)As 2DHG systems [10,14,15]. Although agreement with theory is only partial, these reports demonstrate that strong anisotropy and subband mixing occurs even for the high symmetry direction, and that the classification into light- and heavy-holes has lost its meaning. There appears to be only one previous account of an experimental study of CR for the (311) direction [16]; these authors, working with two samples of 2D n the CR at a magnetic field value which increases with increasing 2D density. This splitting originated, it was suggested, in either an excited-state anti-crossing effect or in a many-body effect of a type previously considered for a 2DEG [17].

In this chapter, we present an experimental investigation of CR splitting effects in a arger number of samples than hitherto used [16], which permits a systematic analysis of the hole density dependence of the anomalous line splitting. Since no theory for the (311)A direction is currently available, the previous calculation [13] for the high symmetry (100) direction is extended to magnetic fields and 2D hole carrier densities appropriate to our measurements. It is shown that the discontinuity effects noted in the present and previous [16] measurements can be reasonably well accounted for by appropriate CR transitions taken from the Landau fan diagram for the (100) direction; discrepancies between theory and experiment are also discussed in terms of the anticipated changes in the theory for the (311) direction.

3.2 (311)A Hole gas heterostructures

Most experimental studies in the past have been performed on modulation doped heterostructures grown on (100) oriented substrates. However, the quality of these devices has been rather poor due to the limited mobility which can be achieved on this surface. The mobility of these modulation doped heterostructures is in general limited by the total ionized impurity density [18] in and near the 2DEG region. During the MBE growth process carbon and sulphur are the two prevalent contaminations present in the growth chamber. The bonding between these impurities and the substrate is weaker at a single dangling bond site than at a double dangling bond site. Hence, the limiting factor during MBE growth is the incorporation of impurities on the single dangling bond sites [1]. The GaAs (311)A structure, which is shown in Fig. 3.1, contains one single and one double dangling bond site per surface unit cell, whereas for the (100) orientation every site is a double dangling bond site. The (311) orientation therefore has benefits for the growth of high purity GaAs.

Doping can be obtained by incorporating silicon (Si) or beryllium (Be) in the lattice.

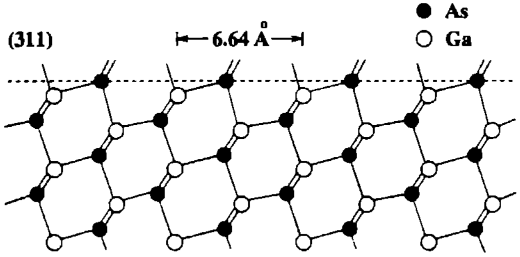

Figure 3.1 GaAs (311)A viewed along the [01$\bar{1}$] direction showing the single dangling and double dangling bonds (after Ref [1]).

Table 3.1 Characteristics of the samples used in this study with areal carrier density N_s, and mobility μ at approximately 100 mK [4].

Sample	Dopant	N_s ($\times 10^{11}$ cm^{-2})	μ (cm^{2}V^{-1}s^{-1})
NU738	Si	1.0	150,000
NU740	Si	1.1	150,000
NU703	Si	1.4	300,000
NU704	Be	1.7	300,000
NU811	Be	2.1	

On the (311)A surface Si takes up sites in the As sublattice and thus acts as a p-type dopant. On the (311)B surface Si takes up Ga lattice sites and acts as a n-type dopant 19]. On the (100) surface Be is used as a p-type dopant. However, since Si MBE sources are generally purer than Be sources, the (311) structures are also of benefit in this respect, and Si does not have the tendency to diffuse during growth as much as Be.

In this study we used a series of modulation doped heterostructures all grown at the University of Nottingham onto (311)A oriented semi-insulating substrates. The electrical characteristics of the samples are listed in Table 3.1.

A typical magnetoresistance trace is shown in Fig. 3.2, reproduced from experiments performed by Rodgers *et al.* [4]. This sample was cut from the same wafer as sample NU703 listed in Table 3.1. Fractional states up to 1/3 are observed in this plot and demonstrate the high quality of structures grown onto the (311)A surface. The data shown in Fig. 3.2 is similar to previous results of Davies *et al.* [2], but the samples of Ref. [4] in addition revealed evidence for a transition to an insulating state consistent with a magnetically induced Wigner crystal [3,4] at high magnetic fields. The experiments presented in this work are well below the field range for which these transitions occur. Furthermore, we notice that the quantum limit, $\nu \leq 1$ (with $\nu = hN_s/eB$), for which only the lowest Landau level is occupied, is already reached between 4 and 8 T in all our samples.

3.3 Experimental results

In the present work we used a combination of Fourier transform spectroscopy at fixed magnetic fields and FIR laser/swept magnetic field techniques to study the transmission of the samples. The samples were mounted in an optical ^{3}He-insert operating at 400 mK. The Faraday configuration was used, and particular care was taken to ensure that the magnetic field was exactly perpendicular to the sample surface. The sample substrates were slightly wedged to avoid Fabry-Pérot interference effects. Magnetic fields were provided by either a 20 T Bitter magnet or a 18 T superconducting magnet. The transmission spectra at $B = 0$ are used as a reference for the spectra at finite fields to obtain normalized CR

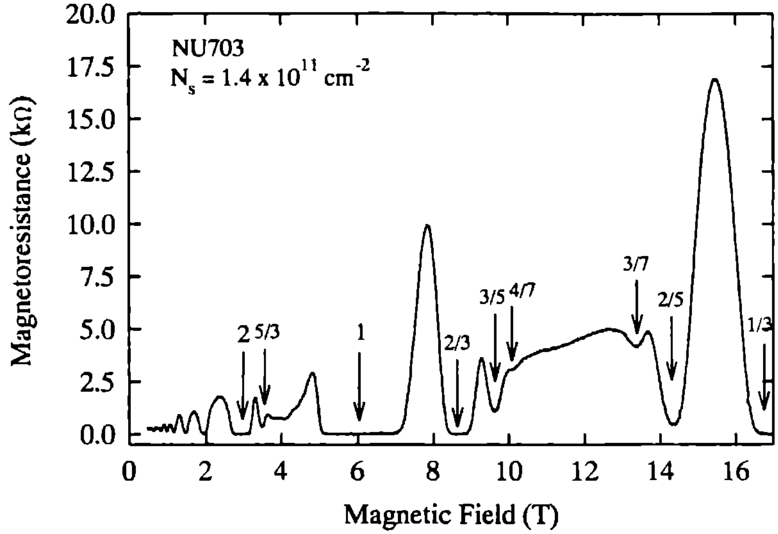

Figure 3.2 Magnetoresistance R_{xx} for sample NU703 at 50 mK. The numbers indicate the filling factor ν. Fractional states up to 1/3 are observed in this plot; after Rodgers *et al.* [4]

transmission spectra. In this method one directly measures the real part of the in-plane finite frequency conductivity of the 2DHG [20].

Figure 3.3 shows a compendium of CR transmission spectra at several different laser energies for NU704 with $N_s = 1.7 \times 10^{11}$ cm^{-2}. A considerable variation of integrated absorption strength and linewidth is observed as a function of magnetic field for this particular sample. The same general pattern is repeated for the other samples studied by swept field FIR laser techniques. Particularly noteworthy is the weakness of the CR absorption at 3.88 meV; this results from the laser energy lying at the centre of the anticrossing region for two Landau levels, as will be discussed later.

In the Fourier transform experiment we concentrated on this particular region of energy and magnetic field. Figure 3.4 shows normalized spectra taken at a series of magnetic fields for the same sample. Similar results are also obtained for the other samples shown in Table 3.1. Two resonances are now generally apparent; the transfer of oscillator strength from the low-energy resonance to the high-energy resonance is particularly striking. At the lowest fields, there only appears to be one absorption; with increasing magnetic field a smaller absorption feature appears at higher energies which grows in strength as the field is increased. The higher energy feature dominates the spectral response at the highest fields investigated, when the low-energy feature has virtually disappeared. The inset of Fig. 3.4 shows the splitting region of the spectra at two different temperatures for sample NU703. It is seen that the linewidth decreases for the lower temperature but the central

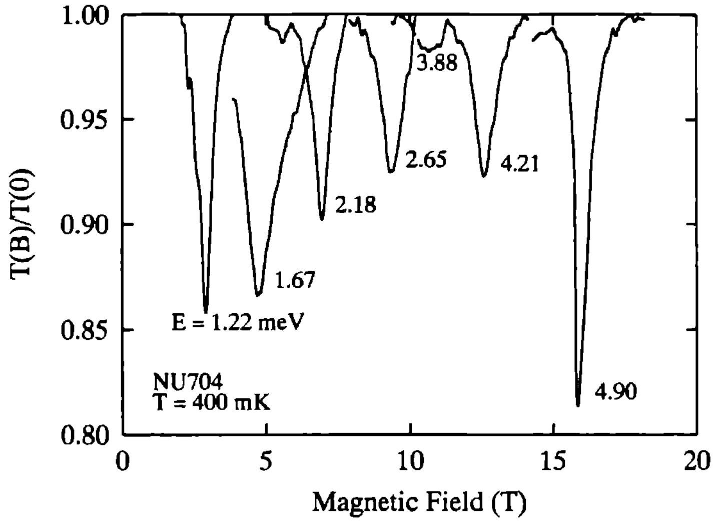

Figure 3.3 Normalized transmission spectra (using the transmission at zero magnetic field) for sample NU704 as a function of magnetic field for several different energies. Note the linewidth oscillations in the low magnetic field region.

mobility increase of the 2DHG at lower temperatures. Another point to be noticed are the strong variations in linewidth at low magnetic fields in both Fig. 3.3 and 3.4. These features coincide with the changes in filling factor as determined from the Shubnikov-de Haas data in Fig. 3.2. Such behaviour is well known from CR measurements on very high mobility 2DEG systems and has been explained in terms of filling factor dependent scattering mechanisms with impurities and disorder [21,22]. A discussion of these effects is beyond the scope of this chapter, and will be omitted.

The cyclotron resonance positions as deduced from these two types of experiments are shown in Fig. 3.5 for three different samples. We note that for low magnetic fields (below 4 T) the CR energy strongly decreases, which is demonstrated in more detail for sample NU703 in the inset. The curve nearly extrapolates to zero frequency; however, the results in this regime are limited by the reduced performance of the spectrometer below 5 cm^{-1} (0.6 meV). The presence of a localization or pinning frequency, which was hard to identify from earlier work [16], can therefore be excluded. From Fig. 3.5 the cyclotron effective mass can be obtained using the standard relationship $\omega_c = eB/m^*$. The cyclotron effective mass obtained in this way is shown in Fig. 3.6 for two different samples. It is observed from this plot that the effective mass is strongly dependent on the magnetic field; the mass initially rises steeply with magnetic field for one branch, and a second branch starts appearing around 6 T which shows a much weaker increase with magnetic field. All the samples investigated exhibited this behaviour, and also all had the characteristic anti-crossing in the mass/field curve at approximately the magnetic field

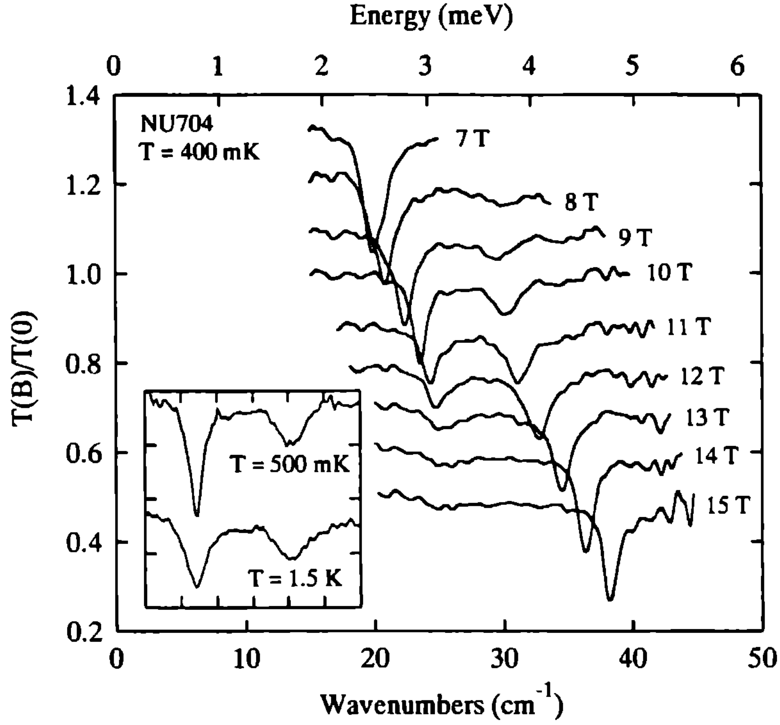

Figure 3.4 Transmission spectra for sample NU704 obtained with Fourier spectrometer at fixed magnetic fields and normalized to the zero field spectra. Lefthand inset: spectra for two different temperatures on sample NU703. Traces are offset for clarity; one division corresponds to 10% change in transmission.

for which the absorption strength is a minimum. Figure 3.6 shows that the effective mass is larger for the sample with the lower carrier density. This increase in mass might very well be associated with the effect of an enhanced repulsion interaction with unoccupied subbands, which will be discussed below in more detail.

Furthermore, from Fig. 3.4 we can define the mean energy where the two CR absorptions have equal strength (*e.g.* the middle of the splitting in the curve for 11 T in Fig. 3.4). These results are plotted as a function of areal carrier density for all samples in Fig. 3.7(a), together with data taken from Ref. [16]. One of the data points shown in Fig. 3.7(a) is of an experiment in which the sample plane was deliberately tilted 2° from the horizontal; the purpose of this experiment was to demonstrate that the presently observed coupling effects did not originate from a tilted magnetic field [23]. Similarly, we can define the magnetic field at which the splitting occurs by the closest approach field of the two branches in Fig. 3.5. A smooth increase in this "closest-approach" field with rising areal density is noted, as may be seen from Fig. 3.7(b). Furthermore, it is seen that the

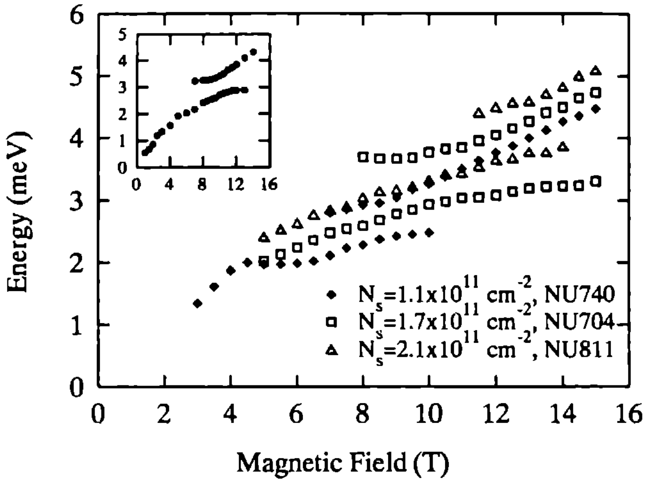

Figure 3.5 Plot of the cyclotron resonance energies for three different samples obtained from swept and fixed magnetic field experiments (*c.f.* Fig. 3.3 and 3.4). The inset demonstrates for sample NU703 that in the low field region the curves nearly extrapolate to zero.

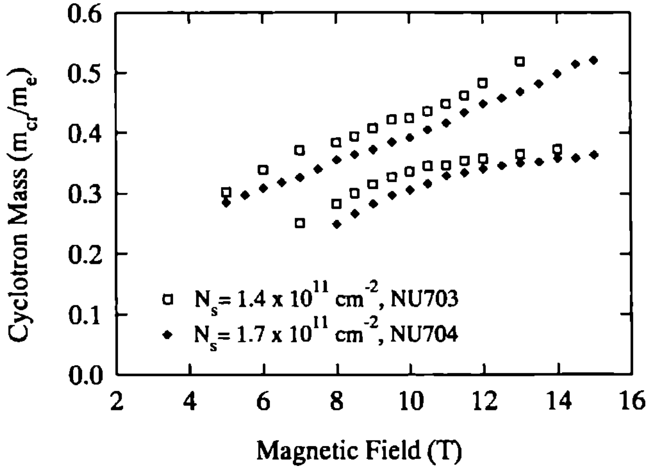

Figure 3.6 Cyclotron resonance effective mass (divided by the free electron mass, m_e) as a function of magnetic field for two different samples NU703 and NU704 with carrier densities 1.4 × 10^{11} and 1.7 × 10^{11} cm^{-2}, respectively.

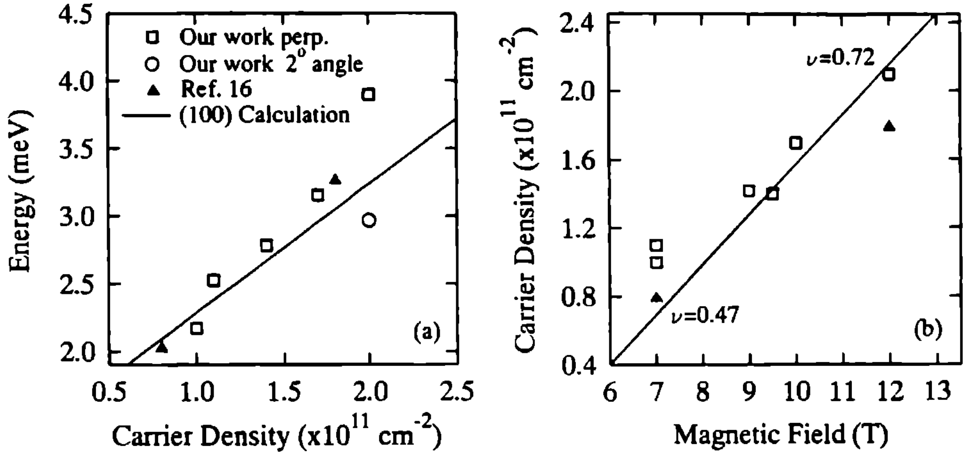

Figure 3.7 (a) The mean energy at the closest approach of the branches in Fig. 3.5 as a function of carrier density for all samples studied. □ : results of the present work, and ▲ : results taken from Schlesinger *et al.* [16], ○ : with the sample deliberately tilted at an angle of 2°. (b) The same as (a) but this time the magnetic field at closest approach of the two branches in Fig. 3.5 is plotted. Two values of filling factor also are indicated. The full lines in both graphs are the results of calculations for the (100) orientation (see text).

filling factor at which the splitting occurs is not constant but instead shows an increase from 0.47 to 0.72, from low to high carrier density samples, respectively. Moreover, the splitting occurs well within the quantum limit.

3.3.1 Calculation of hole Landau levels in magnetic field

In the results we observed a very clear and systematic behaviour of the anticrossing as a function of the 2D carrier density. In order to analyze this behaviour it is of interest to compare this result with theoretical calculations of the hole Landau levels in magnetic field. However, due to the lack of calculations for the (311) symmetry direction, we have to rely on calculations performed for the (100) higher symmetry direction. These calculations were initially performed by Ekenberg and Altarelli [13], and have been extended up to fields of 20 T for a range of 2D hole carrier densities between 0.5×10^{11} cm^{-2} and 3.0×10^{11} cm^{-2}, which cover the range of our experimental parameters. These calculations are rather complex and lengthy, due to the degenerate nature of the valence band. Therefore, we will restrict ourselves to a description of the procedure followed for the calculations, without going into the details. A full discussion of the problem can be found in Ref. [13].

In order to calculate the hole subbands one must take the degeneracy of the valence band in GaAs into account. The top of the valence band at the Γ-point in bulk GaAs behaves as a three-fold degenerate p-like wave function. When the spin-orbit interaction s considered, two different energy levels are expected, corresponding to $J = 3/2$ and $J = 1/2$. The $p_{3/2}$ level is higher than the $p_{1/2}$ level by an amount corresponding to the spin-orbit splitting energy. Furthermore, at $k = 0$ the $p_{3/2}$ level is still fourfold degenerate ($m_j = \pm 3/2$ and $m_j = \pm 1/2$), but for $k \neq 0$ it splits further in a twofold degenerate heavy-hole (HH) band and a twofold degenerate light-hole (LH) band. The split-off band with $p_{1/2}$, which in GaAs is 0.34 eV below the valence band edge, is neglected in the calculations.

As shown by Luttinger [24] the Hamiltonian describing the $p_{3/2}$ levels at the top of the valence band can be represented by a 4×4 matrix with three valence band parameters γ_1, γ_2 and γ_3, which correspond to the inverse effective masses. An important simplification is used by introducing cylindrical symmetry in the Hamiltonian (axial approximation). This approximation implies that the anisotropy in the plane of the 2DHG s neglected. Next, the potential which confines the carriers to a 2D hole gas is added to this Hamiltonian. This potential consists of two parts, the potential due to the mobile carriers in the 2DHG, and the potential due to the ionized impurities in the depletion ayer. The first part is calculated self-consistently in the Hartree approximation by solving Poisson's equation numerically. This calculation yields the electric subband energies and envelope wave functions.

Next, the magnetic field is introduced, which leads to a quantization of the carrier orbits in the plane perpendicular to the magnetic field. To include the magnetic field the following modifications are made to the Hamiltonian: (1) $\boldsymbol{p}$ is replaced by $\boldsymbol{p} + e\boldsymbol{A}$, where $\boldsymbol{A}$ is the vector potential, and (2) a term proportional to the magnetic field weighted by the material constant κ is added. This term represents the interaction of the hole's spin magnetic moment with the magnetic field. The self-consistent potential obtained in the first step without magnetic field is included.

In the axial approximation it is found that the ansatz using a multicomponent wavefunction,

$$\psi_n = (c_1(z)\phi_{n-1}, c_2(z)\phi_n, c_3(z)\phi_{n+1}, c_4(z)\phi_{n+2}) \tag{3.1}$$

becomes an eigenvector of the Hamiltonian and corresponds to a single Landau level ndex n. Here ϕ_n is the harmonic oscillator term corresponding to the quantized motion parallel to the interface, and $c_i(z)$ the wavefunction perpendicular to the interface. n is an integer, $n = -2, -1, 0, 1, ...$ and the $c_i(z)$ coefficients are automatically vanishing for negative oscillator index. For both the HH and LH subband the levels can be ordered in two series, one starting from $n = -2$ and one starting from $n = 1$, corresponding to different "spin" character.

The results of these calculations for the lowest two subbands are shown in Fig. 3.8(a), (b) for two different carrier densities. The calculation assumes that the minority donor density in the GaAs region of the heterostructure is 5×10^{14} cm^{-2}. The notation used to describe the Landau fans in Fig. 3.8(a), (b) is (m, n), where m is the zero field subband index and n is the Landau level index for that subband. At zero field only, the $m = 1$ state corresponds to the HH1 and $m = 2$ to the LH1 subband energies. It is seen that the B-dependence of the Landau levels is far from linear which is directly related to the

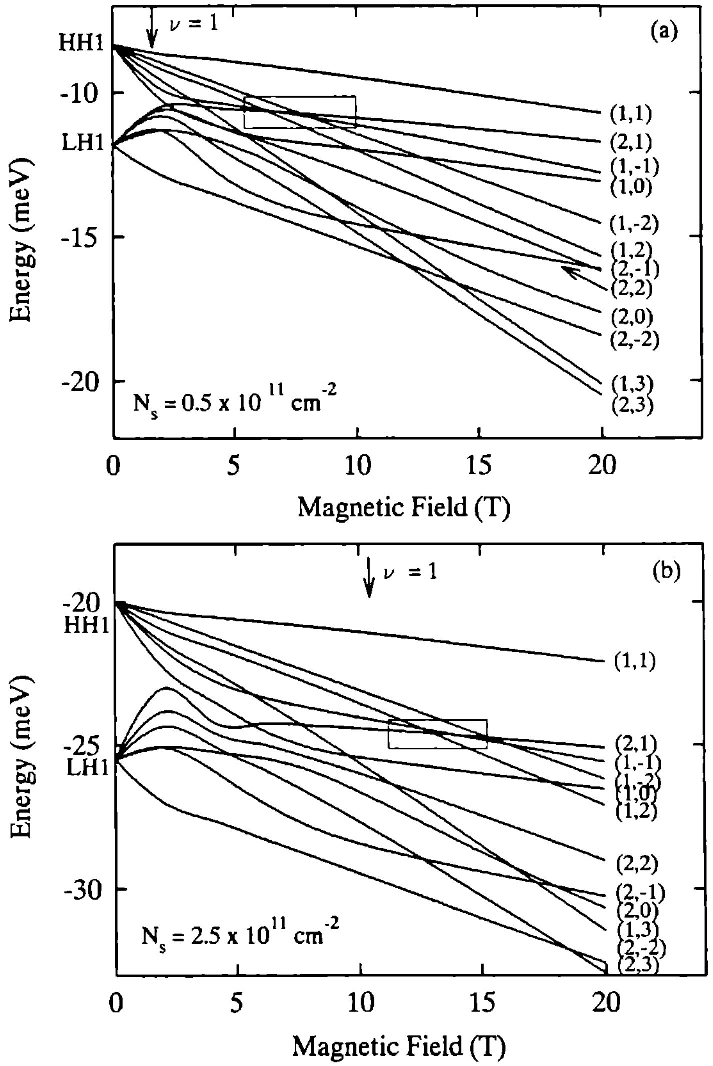

Figure 3.8 Calculated Landau level fan diagrams of the lowest two hole subbands as a function of magnetic field for two different carrier densities as indicated in the graphs. The levels are labeled with the index (m, n), where m corresponds to the zero field subband index and n to the Landau level index. Filling factor $\nu \leq 1$ is indicated with arrows. A particular crossing is highlighted with a box in the graphs (see text).

In the experiment we observe cyclotron resonance transitions between different levels of the Landau fan diagrams in Fig. 3.8(a), (b). Two conditions must be fulfilled for such a transition to take place.

(1) The selection rules for electric-dipole interactions must be fulfilled. These selection rules have been considered by different authors [13,14,25], and it is generally found that within the HH1 subband the strongest transition changes n by plus or minus one. This holds strictly in the axial approximation in which the anisotropy in the 2DHG-plane is ignored. If one goes beyond the axial approximation, Bangert and Landwehr [14] have shown that there is a mixing of Landau levels differing by 4. Thus for $n = 1, 5, 9$ etc. the Landau level index is strictly speaking not a good quantum number. The highest Landau level has a dominant character of $n = 1$ but with some small admixture of $n = 5$ and even smaller admixture of $n = 9$. This means that CR transitions in which $\Delta n = \pm 3$ or 5 etc. become possible, but still less probable than with $\Delta n = \pm 1$.

(2) The transition must also take place from a filled level to an empty level. This implies that in the quantum limit, for $\nu \leq 1$, the transitions can only take place from the (1,1) Landau level in Fig. 3.8.

3.4 Discussion

It is evident from Fig. 3.8 that the zero-field subband separation decreases with reducing areal density; this behaviour is also expected from a simple triangular model for the 2DEG heterostructure potential [26]. It is also evident from these figures that the Landau level fans exhibit strong non-parabolicity and that many level crossings may be observed. At finite values of magnetic field, the crossings observed in the fan diagram occur at progressively higher magnetic fields as the areal density increases; this is illustrated for a particular crossing by a "box" in the two figures. This behaviour follows from the fact that the interaction between the corresponding Landau levels decreases as the areal density increases, and thus an enhancement of their interaction can only be achieved at higher fields. This observation is consistent with the fact that for lower carrier densities an increased effective mass is observed for the whole magnetic field range investigated (see Fig. 3.6).

Additional evidence for the strong interaction between Landau levels is provided by the effective mass curves of Fig. 3.6 for the stronger cyclotron absorption. At low fields the heavy-hole exhibits a relatively low mass but this mass increases with field due to coupling within the Luttinger Hamiltonian [27]. The curves display the discontinuity at the closest approach field, as might be expected, but above this field the mass-curves increase less steeply, which might be construed as evidence for increased subband decoupling effects within the Hamiltonian.

The possible origin of the two resonances will now be discussed qualitatively with the use of the calculated Landau fans for the (100) direction. For the present samples transport measurements [4] indicate that the extreme quantum limit is achieved at magnetic fields of 4-8 T, hence for all our samples the anticrossing occurs for $\nu \leq 1$. CR ate selection rules. Although no calculation of these selection rules for the lower symmetry (311) direction has yet been undertaken, it seems likely that transitions within the same subband manifold will have a greater oscillator strength and that transitions for which the symmetry changes will also be less favoured. The appropriate candidate for the the strongest absorptions noted in Fig. 3.4 will therefore be the hole transitions from the $n = 1$ to the $n = 2$ Landau level within the HH1 subband ($m = 1$). The weaker absorptions (visible between 9 and 12 T) are probably transitions to a Landau level of the LH1 subband ($m = 2$). The (2,1) level from the LH1 subband closely fits the energy observed in the experiment and would be a suitable candidate. However, the (1,2) and (2,1) levels do not anticross for the (100) direction (*c.f.* Fig. 3.8) and because the Landau levels from HH1 and LH1 come from the same Hamiltonian matrix and have the same parity the transition from (1,1) to (2,1) is forbidden ($\Delta n = 0$). Further inspection of Fig. 3.8 shows that the transitions (1,1)→(1,0) and (1,1)→(2,0) do anticross and obey the selection rules. However, at reasonably large magnetic field in the (100) case, the (1,1)→(1,0) transition is expected to have a much smaller oscillator strength than the (1,1)→(1,2) transition [14] and differs considerably in energy from the experiment.

In the (311) direction things should be rather different. Here the lower symmetry should cause a mixing of many Landau levels with different Landau level indices and not just those with indices differing by four, as in the (100) direction [28]. In this case a lot of transitions would in principle be allowed, but from the experimental results one must conclude that many are improbable. In addition, the energies of the Landau levels may also be different for the (100) and (311) direction. Therefore, in order to unambiguously pinpoint the responsible transitions it is essential to have a quantitative knowledge of the Landau levels and the corresponding transition matrix elements in the (311) direction. Such calculations for the (311) direction are presently in preparation [28]. Nevertheless, with respect to expected differences between the (100) and (311) direction, it is reasonable that one of the above mentioned transitions is responsible for the observed anticrossing behaviour.

Additional evidence for the mechanism suggested above is provided by the general agreement between experimental data and curves derived from the (100) calculations shown in Fig. 3.7(a), (b). The theoretical curve is derived from the energy (field) at which the calculated (2,1) and (1,2) levels in Fig. 3.8 cross. If one uses the closest approach field for the (1,0) and (2,0) levels, an identical linear dependence on areal density is found, although the energy of the theoretical curve will be offset from the experimental data. In the case of coupling in a 2DEG induced by a tilted magnetic field [29], a plot of the type shown in Fig. 3.7(a) yields the zero-field subband separation. This is not the case for the complicated valence band structure in 2DHG's, since the Landau levels of the HH1 subband and the LH1 subband exhibit strong non-parabolicity with magnetic field.

Very recently, Hirakawa and coworkers [30] performed an identical study of the CR splitting in (311) 2DHG's. Using both CR spectra and intersubband absorption spectra (measured at zero field), they also identify the observed splitting as an interaction of the Landau levels associated with the HH1 and LH1 subbands. However, the spectra of showing much broader and shallower absorptions, which they interpret as evidence that probably many transitions are involved. In contrast, our well resolved absorptions (*c.f.* Fig. 3.4) suggest rather that only one Landau level of the LH1 subband is involved.

3.5 Summary

We have measured the cyclotron resonance behaviour of several high mobility 2DHG samples grown onto (311)A oriented planes in magnetic fields up to 20 T. Using swept-frequency / fixed field spectroscopy two resonances are generally observable at a given field; the absorption strength shifts from the lower-field to the higher-field resonance as the magnetic field increases. A Landau fan diagram calculation for the (311) direction is extremely difficult, due to the problem of establishing an appropriate *ansatz* for solving the Hamiltonian in this low symmetry direction. The present data have therefore been compared with a self-consistent theory for the higher symmetry (100) direction, assuming that the observed absorption represents transitions within the heavy-hole subband and between the heavy-hole and light-hole subband. In general, these calculations provide strong support for the proposed interpretation. For the lower symmetry (311) direction, additional off-diagonal terms will appear in the Hamiltonian leading to even greater mixing effects and further relaxation of selection rules for cyclotron resonance transitions may also occur.

References

1. W.I. Wang, E.E. Mendez, Y. Iye, B. Lee, M.H. Kim, and G.E. Stillman, J. Appl. Phys. **60**, 1834 (1986).
2. A.G. Davies, J.E.F. Forst, D.A. Ritchie, D.C. Peacock, R. Newbury, E.H. Lindfield, M. Pepper, and G.A.C. Jones, J. Cryst. Growth **111**, 318 (1991).
3. M.B. Santos, Y.W. Suen, M. Shayegan, Y.P Li, L.W. Engel, D.C. Tsui, Phys. Rev. Lett. **68**, 1188 (1992).
4. P.J. Rodgers, C.J.G.M. Langerak, B.L. Gallagher, R.J. Barraclough, M. Henini, G. Hill, S.A.J. Wiegers, and J.A.A.J. Perenboom, J. Phys.: Condens. Matter **5**, L449 (1993).
5. R.K. Hayden, D.K. Maude, L. Eaves, E.C. Valadares, M. Henini, F.W. Sheard, O.H. Hughes, J.C. Portal, and L. Cury, Phys. Rev. Lett. **66**, 1749 (1991).
6. P.A. Harrison, R.K. Hayden, M. Henini, E.C. Valadares, O.H. Hughes, and L. Eaves. J. Vac. Sci. Technol. **B(10)**, 2040 (1992).
7. E.C. Valadares, Phys. Rev. B **46**, 3935 (1992).
8. Z. Ikonic, V. Milan, and D. Tjapkin, Phys. Rev. B **46**, 4285 (1992).
9. A.T. Meney, Superlattices and Microstructures **11**, 31 (1992).
10. H.L. Stormer, Z. Schlesinger, A. Chang, D.C. Tsui, A.C. Gossard, and W. Wiegmann Phys. Rev. Lett. **51**, 126 (1983).
11. T. Ando, J. Phys. Soc. Jpn. **54**, 1528 (1985).

13. U. Ekenberg and M. Altarelli, Phys. Rev. B **32**, 3712 (1985).
14. E. Bangert and G. Landwehr, Surface Science **170**, 593 (1986).
15. Z. Schlesinger, S.J. Allen, Y. Yafet, A.C. Gossard, and W. Wiegmann, Phys. Rev. B **32**, 5231 (1985).
16. Z. Schlesinger and W.I. Wang, Phys. Rev. B **33**, 8867 (1986).
17. Z. Schlesinger, S.J. Allen, J.C.M. Hwang, P.M. Platzman, and R. Tzoar, Phys. Rev. B. **30**, 435 (1984).
18. F. Stern, Appl. Phys. Lett. **43**, 974 (1983).
19. W.I. Wang, E.E. Mendez, T.S. Kuan, and L. Esaki, Appl. Phys. Lett. **47**, 826 (1985).
20. D.C. Tsui, S.J. Allen, R.A. Logan, A. Kamgar, and S.N. Coppersmith, Surface Science **73**, 419 (1978).
21. Th. Englert, J.C. Maan, Ch. Uhilein, D.C. Tsui, and A.C. Gossard, Solid State Commun. **46**, 545 (1983).
22. R.J. Nicholas, M.A. Hopkins, D.J. Barnes. M.A. Brummel, H. Sigg, D. Heitmann, K. Ensslin, J.J. Harris, C.T. Foxon, and G. Weimann, Phys. Rev. B **39**, 10955 (1989).
23. M.B. Stanaway, C.J.G.M. Langerak, R.A.J. Thomeer, J.M. Chamberlain, J. Singleton, M. Henini, O.H. Hughes, A.J. Page, and G. Hill, Semicond. Sci. Technol. **6**, 208 (1991).
24. J.M. Luttinger and W. Kohn, Phys. Rev. **97**, 869 (1955).
25. K. Suzuki and J.C. Hensel, Phys. Rev. B **9**, 4184, (1974).
26. T. Ando, A.B. Fowler, and F. Stern, Rev. Mod. Phys. **54**, 437 (1982).
27. A.S. Plaut, J. Singleton, R.J. Nicholas, R.T. Harley, S.R. Andrews, and C.T. Foxon, Phys. Rev. B **38**, 1323 (1988).
28. U. Ekenberg, private communication.
29. H. Sigg, C.J.G.M. Langerak, J.A.A.J. Perenboom in: *High Magnetic Fields in Semiconductor Physics*, edited by G. Landwehr, Springer Series in Solid State Science **77**, 248 (1987).
30. K. Hirakawa, Y. Zhao, M.B. Santos, M. Shayegan, and D.C. Tsui, Phys. Rev. B **47**, 4076 (1993).

Part II

LOW DIMENSIONAL ORGANIC CONDUCTORS

Introduction

Organic solids are primarily thought of as good electrical insulators. However, the possibility that organic solids might exhibit high electrical conductivity comparable with that of metals was suggested at the beginning of the century [1]. Things took a big step forward when, in 1964, Little [2] calculated that it ought to be possible to make an organic polymer which would be superconducting well above room temperature. Although the superconducting polymers envisioned by Little have not yet been successfully synthesized, his ideas had a great impact on the development of the field of organic conductors. Since this early speculation, the search for organic superconductors has gone along a slightly different route; motivated by the synthesis of the charge-transfer salt TTF-TCNQ, the first organic compound to display truly metallic properties, the focus of attention shifted from organic polymers to organic charge-transfer salts. In 1979, Jérome and Bechgaard [3] discovered the first organic superconductors: charge-transfer salts based on the molecule TMTSF with a transition temperature below about 1.5 K. This discovery stimulated a great deal of activity and through the combined effort of physics and chemistry (or "Crystal Engineering") a large variety of compounds have been synthesized since. Today, the T_c for superconductivity has been raised to 13 K in charge-transfer salts based on the molecule BEDT-TTF [4].

Despite these rather low superconducting transition temperatures (almost an order of magnitude lower than those found in inorganic CuO-superconductors), the organic conductors attracted considerable interest in the past two decades because they exhibit many phenomena that do not occur in ordinary metals. Organic conductors show a remarkable competition between superconducting, magnetic, insulating and metallic states. which depends on the constituents of the compound and on external parameters such as pressure, temperature and magnetic field. Most of these unusual properties arise because the organic crystals are highly anisotropic, so that conductivity is negligible along one or two crystal axes. Depending on the type of molecules and the way in which they are stacked in the crystal, their electronic properties may range from quasi-one-dimensional to quasi-two-dimensional. For example, at low temperatures, when the materials are in their ground state, there may be periodic spatial modulations of the charge-density or spin-density, as predicted for one-dimensional conductors by Peierls [5] and Overhauser [6], respectively. The materials are particularly sensitive to electron-electron correlations and to disorder. In TMTSF-based compounds, application of a magnetic field at low temperatures can induce a transition from a metallic (that is conducting), non-magnetic state to a semimetallic (poorly conducting), magnetic state [7]. In addition, the quantum Hall effect has been observed in these salts (in a bulk material for the first time [8]). Carrier mobilities may range from very low values, characteristic of hopping conduction, to one comparable with the highest values found in conventional semiconductors. In BEDT-

TTF-based compounds, giant magnetoresistance effects, related to the two-dimensional nature of the Fermi surface, can be observed.

The examples mentioned above are just a small collection of phenomena observed in the low dimensional organic conductors. The physics of systems with such "reduced dimensionality" is one of the major themes in condensed matter physics today. A better knowledge of the electronic properties in relation to their specific crystal structure may lead to higher superconducting transition temperatures [9] and useful applications of these materials in the future.

The second part of this thesis is concerned with the far-infrared (FIR) properties of organic charge-transfer salts in the presence of strong magnetic fields. FIR spectroscopy is a simple yet powerful technique which has proven its potential in the study of semiconductors, metals and superconductors. The FIR-range is particularly relevant for organic conductors because many important excitation energies are found in this range. The typical phonon energies, the magnetic energy level separations of the electronic system, as well as the energy gaps related to the low temperature ground states are all in the FIR.

Chapter 4 presents spectroscopic details of the FIR excitation spectrum of the compound $(TMTSF)_2ClO_4$, which is a well known member of the *quasi-one-dimensional* family of charge-transfer salts, also known as Bechgaard salts. This compound is the only ambient pressure superconductor in this family and exhibits a complex phase diagram in the presence of a magnetic field. The specific emphasis in our work will be on the details in the excitation spectrum related to the antiferromagnetic ordering induced by the magnetic field. In a series of three experiments, each concentrating on a different parameter of the phase diagram, the details of the excitation spectrum will be presented (magnetic field up to 30 T, energy between 0.3 and 6.0 meV, and temperature between 0.3 and 7 K). It is shown that there is good general agreement of the optical features with the phase diagram, which has been well established from non-optical studies. However, we will also show that the specific information which can be derived from the excitation spectrum on the energy gap is in disagreement with the accepted theoretical understanding of the magnetic field induced band structure in this material.

Charge-transfer salts of the form $(BEDT\text{-}TTF)_2MHg(SCN)_4$, where M may be K, Tl, Rb, or NH_4 are relatively new members of the *quasi-two-dimensional* family. These salts have been originally synthesized as modifications of the closely related high-T_c salt $(BEDT\text{-}TTF)_2Cu(SCN)_2$, however, they are either not or poorly superconducting. A large number of current investigations concentrate on these salts because of the rather unusual presence of both (antiferro-) magnetic order and strong magneto-oscillatory effects. In chapter 5, we will present a cyclotron resonance study of the charge-transfer salt $(BEDT\text{-}TTF)_2KHg(SCN)_4$. Cyclotron resonance is observed as modulation of the FIR induced reflectance of a mosaic of crystals as a function of magnetic field, enabling a cyclotron mass to be deduced. It will be shown that a comparison between the cyclotron and transport masses provides clear evidence of the importance of electron-electron interactions in this materials.

References

1. H.N. McCoy and W.C. Moore, J. Am. Chem. Soc. **33**, 273 (1911).
2. W.A. Little, Phys. Rev. **134**, 1416 (1964).
3. D. Jérome, A. Mazaud, M. Ribault, and K. Bechgaard, J. Phys. (Paris) Lett. **41**, L95 (1981); K. Bechgaard, C.S. Jacobsen, K. Mortensen, J.H. Pederson, and N. Thorup, Solid State Commun. **39**, 1119 (1980); K. Bechgaard, K. Carneiro, M. Olsen, F.B. Rasmussen, and C.S. Jacobsen, Phys. Rev. Lett. **46**, 852 (1981).
4. J.M. Williams, A.J. Schultz, U. Geiser, K.D. Carlson, A.M. Kini, H.H. Wang, W-K. Kwok M-H. Whangbo, and J.E. Schirber, Science **252**, 1501 (1991).
5. R. Peierls, *Quantum Theory of Solids* (Oxford University Press, Oxford, 1955).
6. A.W. Overhauser, Phys. Rev. Lett. **4**, 462 (1960).
7. J.F. Kwak, J.E. Schirber, R.L. Greene, and E.M. Engler, Phys. Rev. Lett. **46**, 1296 (1981).
8. J.R. Cooper, W. Kang, P. Auban, G. Montambaux, D. Jérome, and K. Bechgaard, Phys. Rev. Lett. **63**, 1984 (1989); S.T. Hannash, J.S. Brooks, W. Kang, L.Y. Chiang, and P.M. Chaikin, Phys. Rev. Lett. **63**, 1988 (1989).
9. D. Jérome, Science **252**, 1509 (1991).

Chapter 4

Magneto-optics of the quasi-1D organic conductor $(TMTSF)_2ClO_4$

Parts of this work have been published in the following papers:

- Phys. Rev. Lett. **67**, 2072 (1991).
- Phys. Rev. B **46**, 8663 (1992).
- Journal de Physique IV (France) **3**, C2-299 (1993).
- Proc. of the tenth Int. Conf. on Electronic Properties of Two-Dimensional Systems, 1993, Newport 1993, and Surface Science to be published.

4.1 Introduction

The charge-transfer salts of the Bechgaard family [1], $(TMTSF)_2X$ (where TMTSF is tetramethyltetraselenafulvalene, and X is ClO_4, PF_6, ReO_4 etc.), have a unique set of properties which depend on temperature, magnetic field and pressure. The discovery of superconductivity [2] in these materials marked the onset of extensive research, devoted to the understanding of the physical properties of these quasi-one-dimensional (quasi-1D) organic conductors [3,4]. The very peculiar properties of these charge-transfer salts are brought about by the fact that the overlap of the electron wave functions in the direction perpendicular to the chains of molecules is only an order of magnitude weaker than in the direction of good conductivity. This anisotropy leads to the characteristic open Fermi surface which consists of two warped sheets. It is well known that the metallic phase described by such a Fermi surface can become unstable due to nesting. At low temperatures charge-density-wave (CDW) or spin-density-wave (SDW) ground states are favoured and may compete with superconductivity. The application of pressure will lead to enhancement of the 2D character, and application of a magnetic field will instead make the material more 1D, and bring it closer to the 1D Fermi surface instability.

A special property of materials like $(TMTSF)_2ClO_4$ and $(TMTSF)_2PF_6$ is that a series of SDW phase transition can be induced by applying a magnetic field [5,6] which lead to nearly quantized steps in the Hall voltage and related features in the magnetoresistance, heat capacity, and magnetization [7,8,9,10]. $(TMTSF)_2PF_6$ is a prototypical member of the family; it exhibits a transition to a SDW insulator at 12 K at ambient pressure. This is suppressed above 6 kbar and superconductivity is observed at these pressures. This superconductivity is in turn suppressed by a small magnetic field, and at much higher fields ($>$ 3 T) the cascade of field-induced spin-density-wave (FI-SDW) transitions is found. $(TMTSF)_2ClO_4$ at ambient pressure has a much more complex phase diagram with FI-SDW's [11,12], reentrance to a metallic state [13], and a controversial "insulating phase" above 27 T [14,15]. These unusual features are thought to be highly dependent on the ordering of the ClO_4-ions [16], and are a subject of ongoing controversy and considerable theoretical attention [17,18,19].

Of great interest in the phase transitions are the changes induced in the electronic excitation spectrum. As in other strongly correlated condensates, like CDW systems and superconductors, the phase transition to the SDW state will result in the creation of a gap in the excitation spectrum. In the last decade a number of theories have been proposed to explain the anomalous behaviour of this special class of charge-transfer salts. The FI-SDW state was first theoretically explained by Gor'kov and Lebed' [20]. Later [21,22] it was shown that the metallic phase was unstable for a quantized set of nesting vectors leading to a hierarchy of subphases. The understanding of the quantized-Hall-like behaviour was less straightforward because the band structure does not indicate any closed orbits on the Fermi surface and therefore conventional Landau level quantization is not possible. The general understanding developed that the single particle excitation spectrum in the FI-SDW phase consists of a series of Landau-like bands separated by more or less equidistant gaps [23,24]. The main SDW gap is predicted to occur at the

Fermi level and, assuming that the carrier density is constant, one expects that this gap roughly follows the variations in the transition line $T_{\mathrm{SDW}}(B)$ [25].

In the past, the optical response has been investigated for a large number of Bechgaard salts [26]. The excitation spectra of the different types of ground state could be approximately explained by theory [27,28]. Up until now, however, there have been no reports of studies of the SDW excitation spectrum in magnetic field. This is probably due to the considerable complexity of combining an optical measurement on these small opaque crystals with both high magnetic fields and low temperatures.

In this chapter we report an extensive optical study of the excitation spectrum of the magnetic-field-induced spin-density-wave phases in the quasi-1D organic conductor (TMTSF)$_2$ClO$_4$. By the use of a large number of experimental techniques we have been able to investigate the complete magnetic field-, energy-, and temperature-dependence of the spectrum, covering the relevant part of the phase diagram at ambient pressure. We find good general agreement of the optical features with the phase diagram, well established from *non-optical* experimental studies. However, the specific information which is derived from the current *optical* study is in serious disagreement with the accepted theoretical understanding of the magnetic field dependent band structure of quasi-1D organic conductors. The results will be presented and discussed in three separate studies each concentrating on a different facet of the phase diagram. In section 4.2 we present the magnetic field dependent reflectivity in fields up to 30 T using monochromatic far-infrared (FIR) energies. We will focus on the observed magnetic field dependent behaviour and reentrant phase transition at extremely high fields. In section 4.3 we present the evolution of the excitation spectrum in the various SDW subphases. The main result of this study is that a gap opens up that is independent of magnetic field and subphase index. Finally in section 4.4, the temperature dependence of the excitation spectrum is investigated. In addition to the energy gap we report the observation of a pinned collective mode resonance, which suggests a coupling between the SDW condensate and the lattice.

Before the optical experiments are presented a short introduction on organic conductors will be given. Some basic properties of quasi-1D conductors will be given together with the current theoretical understanding of the quantized nesting behaviour of the Fermi surface in magnetic field. A comparison is made with experimental results of previous non-optical studies.

4.1.1 Crystal and electronic structure

The organic conductors of the category of the "Bechgaard Salts" are denoted by the generic formula (TMTSF)$_2$X. They consist of large organic TMTSF molecules the cations, see Fig. 4.1) and smaller inorganic X ions (the monovalent anions with X = *e.g.* PF$_6$ or

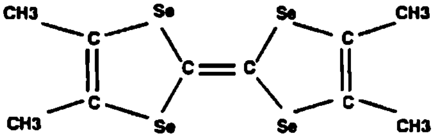

Figure 4.1
Structure of the TMTSF molecule, tetramethyltetraselenafulvalene.

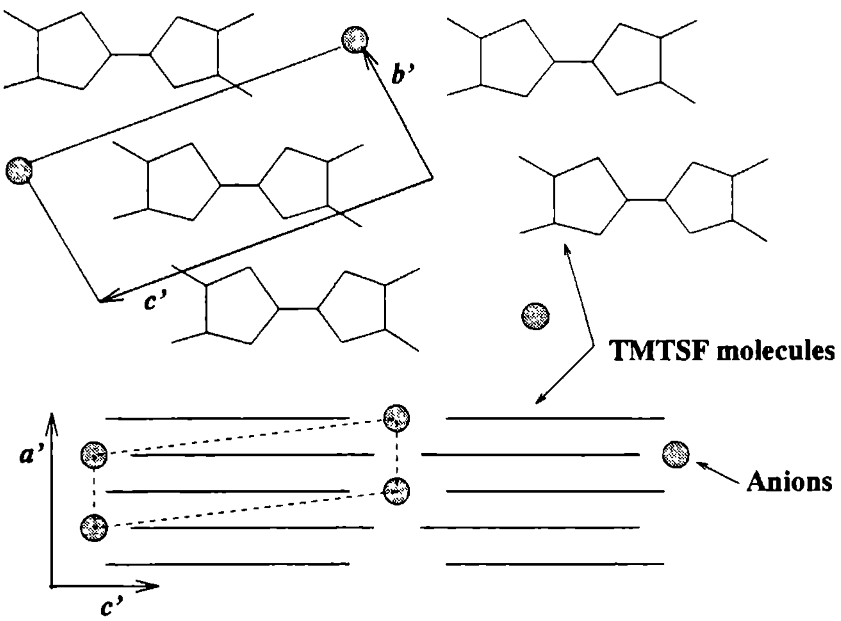

Figure 4.2 Crystal structure of the (TMTSF)$_2$X compounds. *Upper*: View along the *a*-direction, b' and c' are the projections of *b* and *c*. *Lower*: Side view of the stacks (tilted at 10°); a' is the projection of *a*. The dashed lines indicate the unit cell, whose lattice parameters *a*, *b*, and *c* are approximately 7.3, 7.7 and 13.5 Å respectively. The spots represent anions such as ClO_4^-, PF_6^-. The interplanar spacing of the TMTSF molecules along the *a*-direction is about 3.6 Å. After Ref. [29]

ClO$_4$). The bonding occurs via the charge-transfer of one electron from each donor pair of TMTSF molecules to the anion molecule. Figure 4.2 shows a schematic of the crystal structure of (TMTSF)$_2$X (after Ref. [29]). This structure consists of staggered stacks of the large planar TMTSF molecules in the *a*-direction. The anions are ordered in sheets separating the TMTSF-stacks in the *c*-direction. All members of the Bechgaard salt family are isomorphous (triclinic symmetry) with only small differences in the lattice parameters related to differences in anion size.

The typical anisotropy of the crystal structure is reflected in the conductivity, which is largest in the *a*-direction due to the strong molecular wavefunction overlap (predominantly via Selenium) in this direction. The conductivity in the *b*-direction is generally two orders of magnitude smaller, and 5 orders of magnitude smaller in the *c*-direction due to the intervening sheets of ions. Hence these materials are highly one-dimensional in their electronic character. The band structures of the Bechgaard salts have been calculated by Mori *et al.* [30] and Grant [31,32] in the tight binding approximation. From these type of calculations, using the highest occupied molecular orbitals, one obtains the transfer ener-

$t_b \approx 0.1t_a$; the least conducting c-direction is neglected in the calculations ($t_c \approx 0.01t_b$). The 2D electron band energy can be expressed in the tight binding approximation as (assuming orthorhombic symmetry for simplicity)

$$E(k_a, k_b) = 2t_a cos(k_a a_s) + 2t_b cos(k_b b_s) \tag{4.1}$$

where a_s and b_s are intermolecular distances along the a- and b-directions, and k_a and k_b the wave vectors. In $(TMTSF)_2X$ two TMTSF molecules are displaced slightly towards each other, forming a dimerized structure. The dimerized system has a period of $2a_s$ in the stacking a-direction, so that a small gap opens at the Brillouin zone at $k_a = \pi/2a_s$. Assuming that the band is 1D, the Fermi wave vector k_F is found to be $\pi/4a_s$, because for every two TMTSF molecules one electron is transferred from the TMTSF stack to the anion. In this situation the Fermi level is situated at the half-filled level of the upper part of the split band.

Figure 4.3 shows the 2D Fermi surface calculated from the tight binding dispersion in Eq. 4.1 and $t_b/t_a = 0.1$. The main result is that for these band parameters the Fermi surface cannot be closed within the first Brillouin zone. The degree of warping of the Fermi surface is proportional to the transfer energy (= interaction between the stacks) in the b-direction. Therefore this value determines the "degree" of two-dimensionality. In this approximation the Fermi surfaces have an exactly sinusoidal shape, and are still completely nested for the vector $\mathbf{Q_0}$. However, when higher harmonic corrections are included (dotted lines in Fig. 4.3) the surfaces are more corrugated and become less prone to nesting instabilities. This correction is proportional to $(t_b/t_a)^2 = t_b'$ [33] and hence increases when the system becomes more 2D-like.

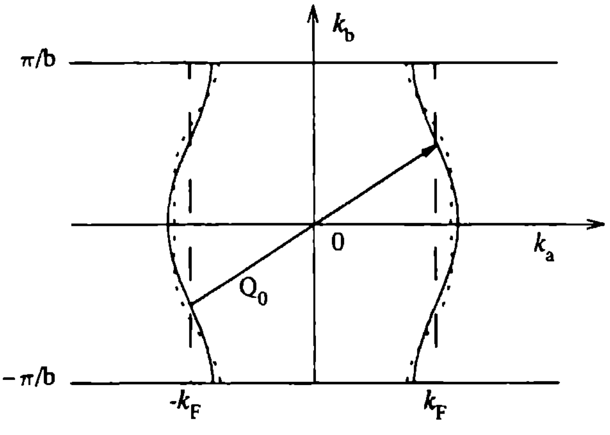

Figure 4.3 Fermi surface for a quasi-1D conductor $(TMTSF)_2X$ (solid line) calculated from Eq. 4.1 in first order approximation, and a truly 1D conductor (long dashed line) in the k_a-k_b plane. The dotted lines show the deviation of the Fermi surface from this simple form as a result of higher harmonic components.

Although the anions do not have a direct effect on the band structure, they play an important role in the low temperature ground state of the Bechgaard salts. ClO_4 is tetrahedral (a little pyramid) and can thus be accommodated in two possible orientations in the lattice. At room temperature the anions have a random orientation, whereas below 24 K they may undergo a structural phase transition to an ordered superlattice when cooled sufficiently slowly (0.1 K/min through the transition temperature) [34]. From X-ray measurements [35] it was verified that the phase below 24 K consists of alternating orientations of the ClO_4 anions in the b-direction with superstructure $(a, 2b, c)$. The consequence is a doubling of the unit cell and a halving of the Brillouin zone in the b-direction. The slow-cooled (i.e. anion-ordered) ClO_4 compound is superconducting below 1 K [36] and also the FI-SDW phases are only observed under this condition. When rapidly cooled ($>$ 50 K/min) the random orientation is frozen in and the resulting low temperature state (below 6 K) was identified as an insulating SDW phase [37]. The PF_6 anion is octahedral (centro-symmetric) and thus no structural disorder is present and the low temperature state always yields a SDW phase. Under pressure however $(TMTSF)_2$-PF_6 is superconducting and like the ordered $(TMTSF)_2ClO_4$ compound it has a cascade of FI-SDW transitions, although at somewhat higher fields.

4.1.2 Theory on quasi-one-dimensional conductors

Zero magnetic field

Before introducing the effect of magnetic field on the Bechgaard salts it is instructive to discuss briefly their zero field properties which are a specific result of the open Fermi surface of quasi-1D conductors. Consider the Fermi surface in a nearly 1D conductor (small transfer energy t_b; solid curve in Fig. 4.3). In this case any perturbation of amplitude Δ and wave vector $\mathbf{Q_0} = (2k_F, \pi/b)$ will couple (or "nest") a large number of degenerate states and so open a gap $2|\Delta|$ across the entire Fermi surface. The opening of the gap will change the energy bands most strongly near the Fermi surface; the occupied states below the gap will have their energy lowered, while the unoccupied states will have their energy raised, and the system becomes insulating. Peierls [38] first demonstrated that below a critical temperature the energy gain of opening this gap will always exceed the energy cost of creating a modulated distortion with wave vector $\mathbf{Q_0}$. Hence, all 1D conductors have this Peierls instability towards an insulating state at low temperatures. The fact that the distortion results in a state where the Fermi energy is located in the gap in all directions is what stabilizes the distorted state.

If the conductivity along the b-axis increases (increase in t_b; dotted line in Fig. 4.3), and becomes more quasi-2D, complete nesting of the warped Fermi surface will not be possible. In this case a gap may open only in a restricted range of the Fermi surface.

In most quasi-1D conductors the low temperature state is a charge-density-wave (CDW) state; a periodic density modulation with wave vector $\mathbf{Q_0}$ of the electronic density which is usually accompanied by a lattice modulation. However, in the Bechgaard salts the low temperature insulating state is not a CDW since the relevant lattice modulations of a characteristic anisotropy of the magnetic susceptibility [39]. This is known as a spin-density-wave (SDW) state; a periodic modulation with wave vector $\mathbf{Q_0}$ of the electronic spin density. The driving mechanism for this state is the on-site Coulomb interaction which in the anisotropic Bechgaard salts is relatively large and of comparable magnitude to the electronic bandwidth. This is a result of the limited screening of the Coulombic charge due to restraints on the electronic movements [40]. In addition, the electron-phonon coupling leading to an excess or deficiency of charge density at a site is opposed by this large on-site Coulombic repulsion [41].

The different ground states among the various members of the Bechgaard family can be qualitatively understood from their degree of one-dimensionality and hence the nesting properties of the Fermi surface (this has been shown more exactly by Yamaji [42] using a mean field approach). ClO$_4$ is the smallest anion in the Bechgaard family and as a result the transfer energy t_b is largest. The Fermi surface is most warped and will not nest. Hence, at low temperatures the Peierls instability does not occur, instead it becomes superconducting when cooled slowly. For the PF$_6$ ion, which is larger, t_b is slightly smaller and the Fermi surface does nest, giving the transition to the SDW state below 12 K. When pressure is applied the transfer energy t_b is increased, making the band structure more quasi-2D, which results in a suppression of SDW state and a transition to a superconductive state at $P \approx 7$ kbar [2].

Finite magnetic fields

When a magnetic field is applied parallel to the least conducting c'-axis of (TMTSF)$_2$ClO$_4$ crystals (or (TMTSF)$_2$PF$_6$ under pressure) a cascade of SDW phase transitions is observed [5,43,44]. The transitions start appearing after a certain threshold field ($H_{\rm th} \approx 3$ T) and depend only on the component of the magnetic field perpendicular to the ab-plane.

Gor'kov and Lebed' [20] first analyzed this problem using a Green's function representation of the nesting vector dependent spin susceptibility $\chi(\mathbf{Q})$. Essentially, a divergence of this function for a certain nesting vector determines the instability and the phase transition. They showed that in magnetic field $\chi(\mathbf{Q_0})$ (with $\mathbf{Q_0}$ the optimum nesting vector defined above) becomes periodically divergent in $1/B$ even if it remains finite in zero field.

A more intuitive picture has been given by Chaikin [45,46], starting from a semi-classical point of view. It starts from the Fermi surface of a quasi-1D conductor such as depicted in Fig. 4.3. When a magnetic field is applied along the c-axis, perpendicular to the ab-plane, the carriers will traverse an open orbit on the Fermi surface in the k_b-direction into the adjacent Brillouin zone. The frequency of traversing successive boundaries is given by $\omega_c' \sim (eB/m_a^*)k_a b$ (m_a^* is the effective mass on the Fermi surface in the a-direction) [46], which replaces the usual closed orbit cyclotron resonance frequency. A two-dimensional dispersion relation is postulated as

$$E(k_x, k_y) = \left(\hbar^2 k_x^2/2m_a^*\right) - 2t_b cos(k_y b), \tag{4.2}$$

with a free-electron dispersion in the a-direction and the c-direction neglected which is allowed when $\hbar\omega_c' > 4t_c$. The quasi-classical quantization in magnetic field corresponds

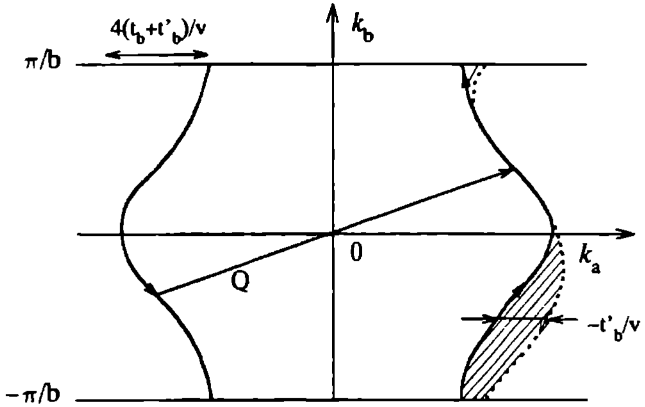

Figure 4.4 SDW wave vector **Q** for which the left hand side of the Fermi surface is translated so that it is tangent to the right hand side. In a magnetic field, $\chi(\mathbf{Q})$ has a maximum when the area of the hatched part is quantized in terms of $2\pi eB/\hbar$. For clarity, the width of the pocket $\sim t_b'/v$ (v is the Fermi velocity) has been exaggerated and in reality it only spans $\approx 1\%$ of the Brillouin zone. The arrows indicate semi-classical trajectories of electrons at the Fermi surface in momentum space. After Ref. [22].

to solving the Schrödinger-type equation

$$\left(\hbar^2/2m_a^*\right)\left(d^2/dx^2\right)\phi - 2t_b cos(k_y b - eBbx/\hbar)\phi = E\phi \tag{4.3}$$

where the Landau gauge is chosen. A linear coordinate transformation $x_1 = x - x_0$ (where $x_0 = k_y\hbar/eBb$) eliminates k_y from Eq. 4.3. The energy eigenvalues are independent of k_y and do only depend on x and k_x. The fundamental effect of the magnetic field is to transform the periodicity in the transverse b-direction into a new periodicity along the a-direction. This new periodicity has the wavelength

$$\lambda = 2\pi x_0 = \frac{2\pi\hbar}{eBb} = \frac{2\pi}{G}. \tag{4.4}$$

Thus Eq. 4.3 describes an one-dimensional problem of a particle in a periodic potential with wave vector G. As a result Chaikin [45] showed that for magnetic fields above a threshold value the dispersion will be 1D and hence an instability must occur. In real space this transition from 2D to 1D behaviour can readily be seen. An electron makes a zig-zag motion in the b-direction and moves with constant velocity in the a-direction. As the magnetic field increases the real-space excursion along b is reduced until eventually the electron is localized on a single chain. This occurs when $\hbar\omega_c' = 4t_b$ and the system is literally 1D and a SDW-state is induced by a magnetic field.

The Orsay-group combined the two above mentioned viewpoints and calculated the divergences of the spin susceptibility $\chi(\mathbf{Q})$ under the condition of the periodic potential with wave vector G [21,22,24]. They found that even in the case of imperfect nesting a series of divergences in $\chi(\mathbf{Q})$ is obtained for a set of nesting vectors $\mathbf{Q}$ when the longitudinal component satisfies $\mathbf{Q}_x = 2k_F + 2\pi N/G$, where N is an integer. In Fig. 4.4 an imperfectly nested Fermi surface is shown, the hatched area corresponds to the unnested region and is proportional to the harmonic correction mentioned above (denoted by t'_b). When $\chi(\mathbf{Q})$ is at a maximum this area was found to be given by $A(B) = N(2\pi eB/\hbar)$ and corresponds to an integer number times the unnested area in zero magnetic field.

The mechanism of successive field-induced SDW (FI-SDW) transitions can now be described naively in the following way [21]. With the imperfect nesting such as shown in Fig. 4.4 the wave vector $\mathbf{Q}$ creates closed orbits on the Fermi surface which are quantized into Landau levels by the magnetic field. The SDW state is not insulating and has still a number $\mathcal{N}$ of carriers near the Fermi level. The total energy is minimized when the number of carriers completely fills an integer number of Landau levels. This implies that the number of carriers has to vary with field so that $\mathcal{N}(B) = NeB/h$. This is possible thanks to a variation of the nesting vector with the field $\mathbf{Q}(B)$. When the field increases, the nesting vector varies with the field so that the number of carriers in the SDW state increases linearly with field. There is then a critical field above which the nesting becomes too bad so that the quantum number N decreases by one unit to get back to the better nesting condition. This mechanism describes a cascade of subphases each of them is characterized by an integer number N of completely filled Landau levels. The Hall voltage is then quantized in each subphase [21,23], and due to the discontinuity of the number of carriers, there is a first order transition between the subphases.

These phenomena, which result from the competition between the nesting geometry of the Fermi surface and the quantization of electronic orbits, has been christened the quantized nesting mechanism [21] and was later called the standard model [23,24,47].

Comparison between theory and experiments

Given the standard model, it has been possible to explain many of the features observed in the Bechgaard salts. This appears to work best for the compound $(TMTSF)_2PF_6$ which under pressure exhibits a clear cascade of first order FI-SDW transitions [5] when the zero-field SDW is suppressed. It nicely demonstrates the opposite effects of pressure and magnetic field on the dimensionality of the Fermi surface. The observation of a well developed quantum Hall effect (QHE) with a transition to the insulating $N = 0$ state at high fields strongly supports the assumption of completely filled Landau bands around the Fermi level. However, deviations from the usual QHE observed in 2D-semiconductors occur in that the ratios between quantized plateaux depend strongly on pressure [48] and that the longitudinal resistance does not tend to zero as expected.

The $(TMTSF)_2ClO_4$ compound shows strong deviations from the standard model. At ambient pressure a well developed cascade of FI-SDW transition is again observed [6]: however, at ~ 27 T it shows a reentrance into the metallic state [13]. In Fig. 4.5 a schematic phase diagram is presented, composed of data taken from several different groups [9,10,13,14]; the standard model follows the long-dashed line at high fields. At low temperatures and high magnetic field above the reentrant phase boundary a new insulating phase has been observed which might be another SDW state [14]. The large and extremely stable state between 8 and 27 T was first thought to be the final $N = 0$ SDW phase, however, this phase is not an insulator and a lot of the discussions in the literature centered on the correct assignment of it ($N = 0$ [47], $N = 1$ [19], and even $N = 1/3$ [11]). Up to now no conclusive assignment has been possible. The reentrant behaviour is generally thought to be intimately related with the anion ordering in this compound. This could give rise to an additional periodic potential in the crystal which might suppress the $N = 0$ phase [18,19]. An alternative explanation has been given by Yakovenko [17], entirely independent of the nesting model. In a complex treatment he shows that the competition between Cooper and Peierls channels leads to a destabilization of the SDW in high fields [49]. However, the crucial parameter in his model appears to be unphysical [15]. It must be noted that neither of the two models mentioned above is yet capable of predicting the correct shape of the phase diagram of $(TMTSF)_2ClO_4$. In addition, the QHE is poorly developed in this compound and at certain magnetic field values the Hall-voltage even changes sign [50].

A separate issue are the rapid oscillations (RO) which have been observed in all transport and thermodynamic measurements of $(TMTSF)_2ClO_4$. These oscillations mimic many of the features of normal closed-orbit Shubnikov-de Haas oscillations. The RO appear both below and above the FI-SDW phase boundary and can thus not be related with the SDW state. Because the amplitude of the oscillations depends strongly on cooling rate, models have been proposed which relate them to the above mentioned anion ordering. However, identical oscillations have also been observed in $(TMTSF)_2PF_6$ (which does not have anion disorder) and so seems to rule out such a mechanism [51], leaving this feature essentially unexplained.

The fact that the band parameters of the ClO_4 and PF_6 compounds only differ by a few percent [31] and that yet their phase diagrams do not universally converge to that predicted by the standard model, is an indication that there are some essential parts missing in the theory. Certainly the ClO_4 compound seems to require additional ingredients, or maybe a completely different approach [17]. In a recent report [16] on the complete phase diagrams of the PF_6 and ClO_4 compounds versus magnetic field, temperature and pressure, it was surprisingly found that above a critical pressure of 5 kbar the anion ordering is suppressed, and it was suggested that above this pressure $(TMTSF)_2ClO_4$ does show normal standard model behaviour like $(TMTSF)_2PF_6$. However, the magnetic fields available currently are too low to justify such a conclusive assignment.

A final point is the proportionality relation between T_{SDW} and the magnetic field dependent ground-state properties formulated by Montambaux *et al.* [25]. This relation is based on a very general model-independent thermodynamic description of a system with many gaps, and assumes a BCS-like form for the second order metal to SDW transition. If one uses $T_{SDW}(B)$ (the contour of the phase diagram in Fig. 4.5) as an input parameter then one finds that the SDW-gap at the Fermi level should be directly proportional to it. Therefore, measuring this energy gap and establishing its magnetic field and temperature dependence could give a conclusive verification of the standard model.

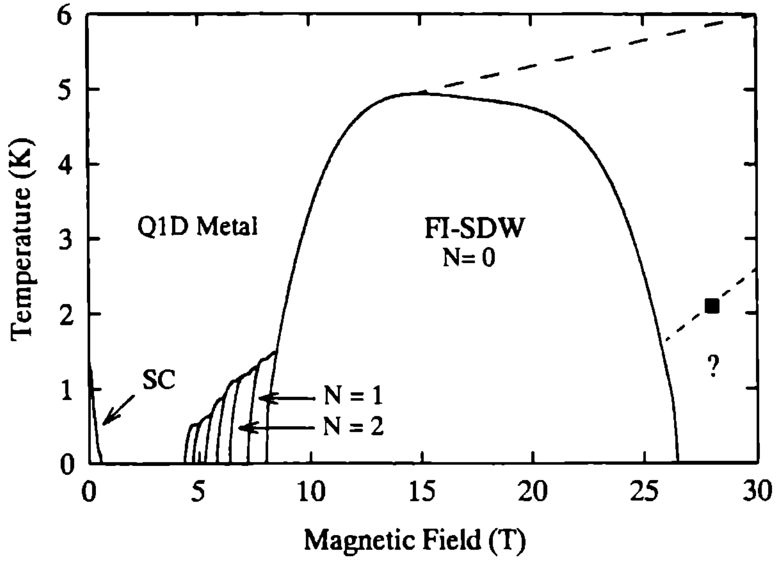

Figure 4.5 A schematic phase diagram of $(TMTSF)_2ClO_4$ (solid line), based on a compilation of calometric [10] and magnetization [9,13] measurements. The final FI-SDW state is referred to as the $N = 0$ state, the one before $N = 1$ state, etc.. The question mark indicates another possible state observed by Yu *et al.* [14]. SC stands for the superconducting phase. "The Standard Model" is shown as a long dashed line and does not cover the experimental data at very high fields.

4.2 Magnetic field dependent behaviour in $(TMTSF)_2ClO_4$

The observation of the QHE [51,52] in quasi-1D organic conductors with an open Fermi surface implies that, within the framework of quantized nesting [21], completely filled and empty Landau bands should straddle the Fermi level with changing magnetic field. The corresponding theoretical magnetic field dependent energy spectrum has been calculated by Montambaux and Poilblanc [24]. From a naive point of view this spectrum shows some superficial similarities to the Landau level spectrum known from the two-dimensional electron gas (2DEG) in semiconductor systems. However, for the quasi-1D conductor the energy spectrum only exists above a threshold field applied along the least conducting c'-axis. Furthermore, the bands and gaps reorganize at each successive FI-SDW phase transition, always keeping the largest gap at the Fermi level. Specific heat measurements on $(TMTSF)_2ClO_4$ have given thermodynamic evidence for the main SDW gap at the Fermi level, but there are deviations from a simple weak coupling picture [10].

Magneto-optical techniques have proven to be a powerful tool in the investigation of band structures in general. In the organic conductors the typical energies involved are in the meV-range and the energy spectrum should therefore be probed with wavelengths in the far-infrared (FIR). In this section, monochromatic FIR reflectivity measurements are presented on the organic conductor $(TMTSF)_2ClO_4$ undertaken to directly determine the magnetic field dependent energy spectrum and to optically investigate the very high magnetic field anomalies. In contrast to $(TMTSF)_2PF_6$, $(TMTSF)_2ClO_4$ exhibits FI-SDW states at ambient pressure and is thus more suited for this optical investigation. In the spectra we observe both energy dependent and independent features as a function of magnetic field. The latter coincide with the threshold fields of the cascade of FI-SDW transitions, and we will interpret this as evidence for the opening of an energy gap n the density of states. The energy dependent features point towards the existence of Landau quantization. We will argue that these features are related to the rapid oscillation phenomena which are also observed in the reflectivity spectra. We also observe in the optical data details associated with anomalies in this material in high magnetic fields.

4.2.1 Experimental details

A dozen single crystals of $(TMTSF)_2ClO_4$ were arranged in a parquet with their *c*-axes parallel to the applied magnetic field in order to increase the optical signal from these small crystals. This parquet of crystals was placed at the magnetic field centre, with its upper surface 1 mm below a conical light guide from which the FIR radiation emerged; the diameter of the exit orifice of the cone was 1.5 mm. The FIR radiation between 8 and 160 cm^{-1} was provided by an optically pumped laser [53]. The FIR radiation was unpolarized in this work. A carbon bolometer was placed above the parquet just to one side of the cone, in order to detect the reflected radiation. A similar bolometer was placed n the light guide above the cone, in order to monitor the incident FIR radiation, so that normalized reflectivity spectra could be recorded [54]. Transport leads were attached to one crystal placed outside the path of the light, and this sample was used for monitoring the formation of FI-SDW states and rapid oscillations. The samples were slow-cooled through the anion ordering transition at 24 K to ensure the completion of the structural phase transition needed for the formation of FI-SDW states and rapid oscillations. The high magnetic fields necessary for the observation of FI-SDW states and the reentrant phase transition were provided by a 30 T hybrid magnet and 20 T Bitter coils.

Finally we mention that in this chapter we use wavenumbers (number of wave-engths per cm vacuum) as a frequency measure, a common practice for spectroscopists; 100 $cm^{-1} \simeq 12.42$ meV.

4.2.2 Results

The main results of this work are summarized in Figs. 4.6 and 4.7. The normalized reflectivity change $\Delta R/R$ versus magnetic field and laser energy for five field sweeps at a temperature of 1.2 K is shown in Fig. 4.6 and in Fig. 4.7 the energy and magnetic field dependent structure in $\Delta R/R$ has been plotted. The measurements address three different ranges in the phase diagram (see Fig. 4.5).

(a) The vicinity of the threshold field and multiple subphase region is shown in Fig. 4.6. Here several features are immediately evident. First, there is a pronounced

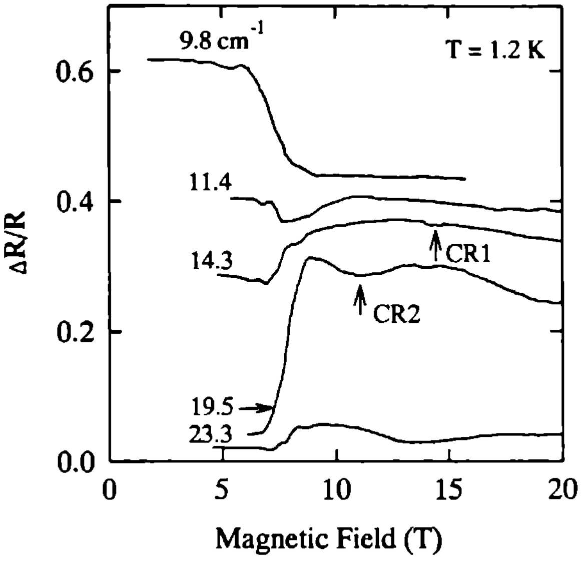

Figure 4.6 Relative change in the reflectivity $\Delta R/R$ versus magnetic field at 1.2 K for different frequencies. The traces are offset for clarity, and one unit corresponds to 10 % change in $\Delta R/R$.

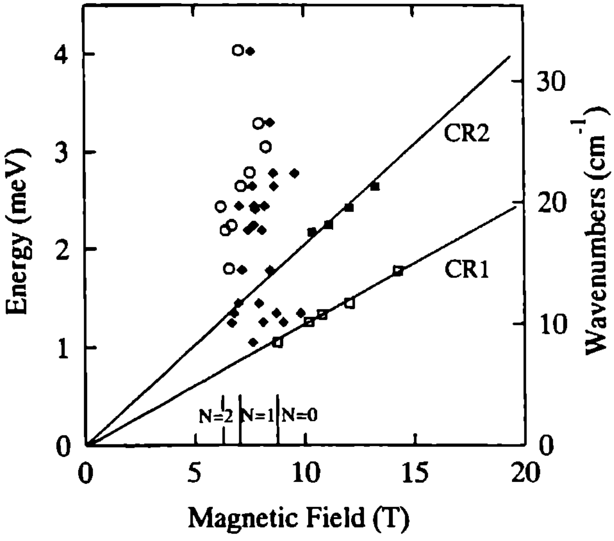

Figure 4.7 Energy and magnetic field dependent features of the reflectivity signal at 1.2 K. □ : CR1; ■ : CR2; ○ : position of onset of change in $\Delta R/R$; ◆ : position of additional features.

which is energy dependent. Secondly, there are magnetic field dependent features (dips) characteristic of cyclotron resonance (CR) behaviour. And thirdly, significant additional structure appears just above H_{th}.

(b) At intermediate fields in the $N = 0$ SDW phase, Fig. 4.8(a) shows the appearance of structure with the periodicity of the SdH-like rapid oscillations in the magnetoresistance signal. In Fig. 4.8(b) both CR2 and the rapid oscillations above CR2 are observed. The two particular energies plotted in this figure are representative for the results obtained for many different energies.

(c) At the highest magnetic fields the high field reentrant phase boundary has been explored, as shown in Figs. 4.9(a) and 4.9(b). The magnetoresistance of the transport sample indicates the position of the reentrant phase boundary. At the lowest temperature (0.7 K), $\Delta R/R$ shows a weak (but reproducible) dip at the reentrance, which is slightly changed in shape at the highest photon energy. At intermediate temperatures, only one energy was possible (due to practical circumstances), and a very broad feature was identified with a change of slope in the reentrant region (not shown). At the highest temperature (3 K), a sharp drop was observed for all three energies investigated at the reentrance.

4.2.3 Discussion

An important feature of the present work is that a SDW state can be induced by a magnetic field. Hence the energy dependent differences in the optical signals between the metallic and SDW state are easily observed, as indicated in Fig. 4.6. Magnetic field induced changes in $\Delta R/R$ are in some way related to changes in the conductivity of the system. Thus the sign reversal of $\Delta R/R$ as function of energy indicates a prominent change in conductivity around 13 cm^{-1} at a field of 8 T. This result can be compared with previous work on quenched (SDW) samples by Ng *et al.* [55] where a clear onset of conductivity was found at an energy of 20 cm^{-1} (with the polarization parallel to the *a*-axis). There is some similarity in character, but it is difficult to make a quantitative comparison between the two types of measurement. The SDW state in quenched samples may be highly sample dependent [56], uncertainties due to diffraction effects [26] and mode switching may come into play, and polarization may play a role. Nevertheless, the energy dependent nature of the background signal reverses sign near 13 cm^{-1} (=1.5 meV =17 K). In the usual BCS mean field treatment, $2\Delta/k_BT = 3.5$, the $N = 0$ SDW gap $2\Delta_{\text{SDW}}$ is 16 K (*c.f.* Fig. 4.5). In the light of previous work on quench-induced SDW $(\text{TMTSF})_2\text{ClO}_4$ and the close correspondence of mean field prediction and optical energies of the features, this effect seems to be highly correlated with the opening of the SDW gapped state above H_{th}. From a few energies alone one cannot determine the possible energy dependence of this SDW gap as predicted by theory [25]. In the next section we have elaborated on this issue in more detail by employing broad-band interferometer techniques and by using lower sample temperatures to enhance the sharpness of the features.

Unlike the broad variations in background signal discussed above, the energy- and

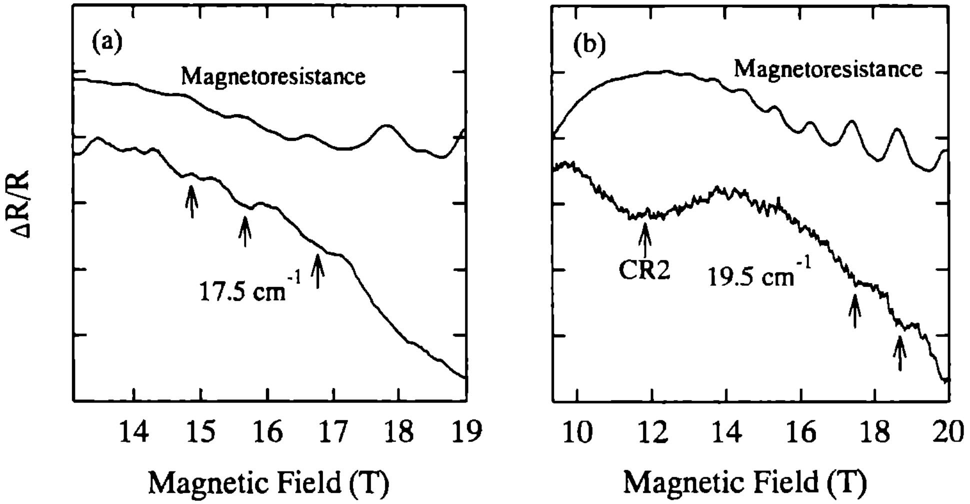

Figure 4.8 Rapid oscillation signals (magnetoresistance and reflectivity) in a highly ordered sample. Arrows indicate oscillations. (a) Over a range of fields at 17.5 cm^{-1}. (b) Over a range of fields at 19.5 cm^{-1}, here both CR and oscillations are evident.

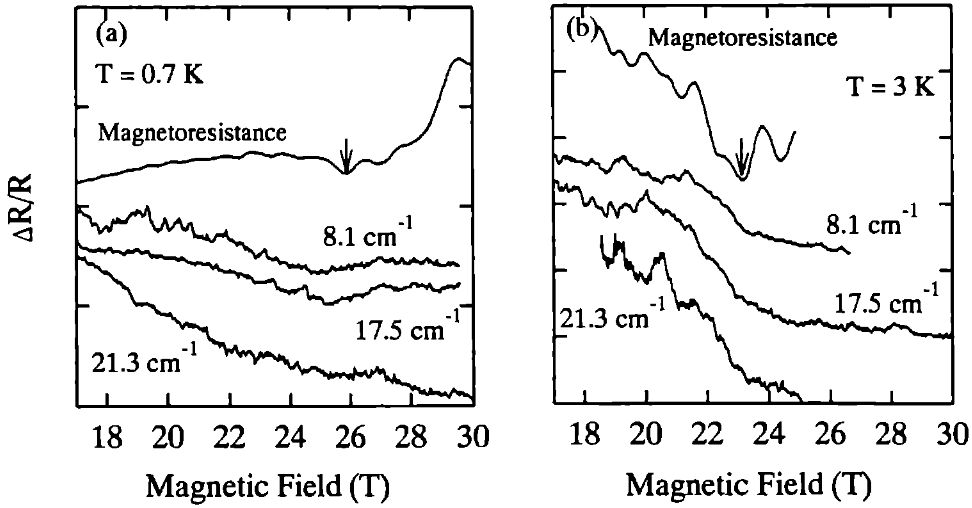

Figure 4.9 Energy and temperature dependent investigation of the reentrant regime. (a) For a temperature of 0.7 K, and (b) for a temperature of 3 K.

possible underlying gap spectrum. The density of states changes in the field-induced SDW states at each subphase, hence the changes in reflectivity observed arise from passage from one SDW phase to another, and should correspond to the positions of the SDW phase boundaries and be independent of energy. In the region between $H_{\rm th}$ and the $N = 0$ phase transition a large number of features have been indicated in Fig. 4.7. From the phase diagram in Fig. 4.5 it is clear that at a temperature of 1.2 K the phase transitions are close together and will result in multiple features between $H_{\rm th}$ and the $N = 0$ phase boundary line. Between the $N = 1$ and $N = 0$ phases, the most dramatic change in the phase diagram takes place, an effect which is also apparent from the reduction of data points in Fig. 4.7. However, between $H_{\rm th}$ and $N = 0$ no magnetic field dependent features can be assigned with confidence.

The shallow features above 8 T in Fig. 4.6 do reflect magnetic field dependent behaviour as can be observed from Fig. 4.7. Here we have arbitrarily labeled the two prominent cyclotron resonant features as CR1 and CR2, which by simple analysis yield effective masses of $m^*/m \approx 1.0$ (CR1) and $m^*/m \approx 0.6$ (CR2), where m is the free electron mass. CR2 has by far the strongest oscillator strength and exhibits an increasing inewidth with increasing magnetic field. CR1 is only a very shallow absorption, and is very close to the gap edge expected from the mean field SDW gap value. It would be tempting to assign these features to transitions between the Landau bands as predicted by theory [24]: however, at lower temperatures CR1 is not visible and the oscillator strength of CR2 is decreased, whereas the energy-independent features increase with decreasing temperature (see next section). This is opposite to what one would expect for resonant transitions within an energy spectrum when the thermal smearing decreases with decreasing temperature. An alternative explanation could be that these resonances are related to the phenomena causing the anomalous rapid oscillations observed in these materials [12], which show a similar activated behaviour.

In Fig. 4.8 we show the rapid oscillations both in the transport and in the reflectivity, where in one case the field range is sufficient to see CR2 at a field below the oscillations. We note that for a 2DEG, Ando [57], first showed that SdH oscillations should be superimposed on the cyclotron resonance signal, an effect which has indeed been seen experimentally [54]. Except for qualitative similarities between Fig. 4.8(b) and the Ando picture, we cannot with certainty make the association between CR2 and the rapid oscillations. Possible evidence also lies in the consideration of the rapid oscillation frequency of 225 T [12] under the simplifying but unrealistic assumption of a circular k-space orbit. The period $\Delta(1/B)$ of SdH oscillations is related to the effective mass and Fermi velocity $v_{\rm F}$ by the relation $\Delta(1/H) = 2e\hbar/m^{*2}v_{\rm F}^2$. The Fermi velocity, deduced from the transfer energy in the a-direction, is $\approx 2 \times 10^5$ m/s [58] which gives a rapid oscillation effective mass of $m^*/m = 0.5$, in rough agreement with the mass found for CR2. With respect to CR1 the comparison with the rapid oscillations is less clear. In a detailed magnetoresistance experiment Ulmet *et al.* [59] observed a second much weaker oscillation-period. This period has nearly an equal frequency to the stronger oscillations, but a different temperature dependence; it is only observed in a restricted temperature tions were attributed to a nearly equal sized pocket of different carrier type as the strong oscillations. It may be that the weak CR1 and the weak oscillation-period have the same origin. However, in Ref. [59] it is noted that the quality of the sample may be crucial for the observation of such a double series of oscillations and their result is the only report of this effect thus far. In order to unambiguously assign the CR lines to the rapid oscillation phenomena, a cyclotron resonance measurement is needed below H_{th} where the SDW phases cease to exist but the rapid oscillations are observed. Although the metallic state, the low energy, and the anisotropy complicate the measurement, it should be possible.

Finally the results close to the reentrant transition above the $N = 0$ state should be discussed. Here, at least at temperatures above 2 K, the material returns to a metallic state. At low temperatures, there is mounting evidence that the state is gapped [14]. Our high temperature data show a sharp drop in $\Delta R/R$ at the transition, which may represent the return of metallic behaviour observed below H_{th}; our low temperature data show a dip followed by a much less dramatic change. This may represent a transition from the $N = 0$ state to another gapped state at higher fields, with an intervening metallic phase at the transition. This interpretation is consistent with both specific heat [15] and thermopower [14] measurements above the reentrant phase line.

4.2.4 Summary

FIR reflectivity measurements were used to determine the energy spectrum of the organic conductor $(TMTSF)_2ClO_4$ in high magnetic fields. This is the first such determination of the magnetic field induced energy spectrum in an organic conductor. The results fit well with the phase diagram found by other experimental methods and demonstrates that the cascade of FI-SDW phase transitions can be optically detected. We argue that the two main resonant lines CR1 and CR2 could be associated with the rapid oscillation phenomena. In addition we find evidence for the opening of an energy gap in the density of states at the threshold field of the FI-SDW phase transitions. Finally, we have explored the reentrant phase line and found consistency between optical and thermodynamic measurements.

4.3 FIR spectroscopy of the FI-SDW gap in $(TMTSF)_2ClO_4$

In the past decade a large number of extensive spectroscopic studies have been performed on the Bechgaard salts [26], however, none were performed in magnetic fields strong enough to induce the FI-SDW states. Instead these investigations concentrated on the low temperature conductivity in the metallic, density-wave (SDW or CDW), and superconductive states. The conductivity in the metallic state is in general very different from the Drude-type conductivity observed in ordinary metals and is strongly anisotropic in the *ab*-plane. In contrast to the high dc-conductivity there is no evidence of strong metallic reflectivity. Instead the Bechgaard salts show a region of depressed optical conductivity in the FIR regime. This discrepancy has been generally explained in terms of a narrow nism implies that the current at low temperatures is carried by this collective mode [60]. A second explanation that is widely accepted is in terms of a single particle picture of carriers with a very long mean free path [61]. The reduction in low frequency conductivity is then attributed to some experimental artefact such as a damaged surface which is then not representative for the bulk properties of the material [62].

In the group of materials with octahedral anions (AsF_6, Sb_6, PF_6) a SDW transition takes place at ~ 12 K. In the spectra clear changes are observed when passing the transition temperature, corresponding to a developing gap in the density of states [60,61,63]. However, the conductivity below the gap energy does not vanish completely as expected, suggesting that the gap is anisotropic with parts of the Fermi surface being gapless [26,63]. In recent experiments Quinlivan *et al.* [64] investigated the microwave and submillimeter properties of the SDW state in $(TMTSF)_2PF_6$. They observed a conductivity edge in the spectra which was interpreted as evidence for the opening of a SDW gap, accompanied by the appearance of a collective mode resonance of the SDW condensate.

In addition, Eldridge *et al.* [65] measured the absorption spectra of a large number of powdered Bechgaard salts. From these spectra a large number of low energy phonon modes could be identified. Most interesting are the low frequency phonon modes which only appear after the structural ordering in the salts with tetrahedral anions and can therefore only be observed in the slow-cooled state of $(TMTSF)ClO_4$.

In the previous section we concluded that the reversal of the background reflection signal in the optical data indicated the opening of a FI-SDW gap. However, from a few monochromatic energies alone it is impossible to derive the theoretically predicted [25] behaviour of the gap in the various subphases. In this section we present a detailed FIR and microwave study in the range between 1.5 and 45 cm^{-1} in fields up to 20 T, covering both the metallic and FI-SDW states in $(TMTSF)_2ClO_4$ at a temperature of 400 mK. The broad-band interferometer technique allows a detailed investigation of the threshold fields of the FI-SDW subphases which are well separated at this low temperature (*c.f.* Fig. 4.5). We report the spectroscopic observation of the evolution of the excitation spectrum in the various FI-SDW subphases. The main result of this work is that a gap opens up the energy of which is independent of magnetic field or subphase index. We interpret this as evidence that the gap is nonuniform in *k*-space and that the gapped area on the Fermi surface appears to increase discontinuously upon each phase transition to a lower index spin-density-wave state. We will discuss additional observations related to a collective mode excitation in the microwave region and a coupling of low energy phonons to the spin-density modulation.

4.3.1 Experimental details

The samples used in this work were prepared in a standard electrochemical way, yielding very pure crystals with a typical size of 0.5 × 1 × 7 mm^3. In order to enhance the optical signal from these small crystals, we arranged a dozen crystals in a grid like structure, so that the plane of the grid coincides with the *ab* plane of the crystals. The samples were then placed in a ^3He cooled sample holder, mounted in the bore of either a 10 T superconducting magnet or of a 20 T Bitter magnet. The magnetic field direction was chosen along the c'-axis, perpendicular to the grid. We used different FIR set-ups; an optically-pumped molecular FIR-laser, providing approximately 20 lines in the submillimeter range (10-30 cm^{-1}), several microwave klystrons in the frequency range between 30 and 70 GHz (1-2.5 cm^{-1}), a set of microwave pumped diode frequency multipliers, yielding a nearly continuous output between 2 and 15 cm^{-1} and a Bruker IFS 113v Fourier transform IR spectrometer. All sources could be connected to the insert using lightguides and could be interchanged without affecting the sample conditions. The combination of these different sources allows a quasi-continuous spectroscopy from the infrared range down to approximately 1.0 cm^{-1}.

The FIR light intensity was measured with Si bolometers cooled to 1.2 K. The sample was cooled at a rate of 30 mK/min through the anion ordering transition at 24 K and was kept at 400 mK during the experiment. Both reflection and transmission of the sample grid could be measured simultaneously, a technique first exploited by Ng *et al.* [66] on these materials. Because of the large conductivity along the a-axis, the reflectivity is close to unity and field dependent changes in the extreme FIR are difficult to detect. The basic reason for using a grid arrangement is that transmission is restricted to a polarization along the less conducting b-axis and multiple reflections will enhance the effect of changes in conductivity. Therefore the signal measured by the transmission bolometer basically corresponds to the sample *reflectivity*. A disadvantage of this configuration is that it is difficult to calibrate the absolute value of the sample absorption and perform Kramers Kronig analysis. The linear polarization of the transmitted light in the spectral region of interest (below 30 cm^{-1}) was confirmed in a separate experiment for temperatures down to 4 K. A second sample was placed outside the optical path but in good thermal contact with the holder. The magnetoresistance of this reference sample was used to monitor the formation of FI-SDW states.

4.3.2 Results

Figure 4.10(a) shows the normalized transmission through the sample grid versus magnetic field for several monochromatic FIR energies. Here the transmission (T) taken in an applied field B is divided by the transmission in zero field. Large changes are found in $T(B)/T(0)$ at the various phase transitions. At this low temperature the transmission changes in a steplike fashion with nearly field independent plateaux in between. With the help of the magnetoresistance data (Fig. 4.10(b)) taken on the reference sample these steps can be identified to correspond with transitions between different FI-SDW subphases. Above 7 T the spectra exhibited a large hysteresis depending on the magnetic field history. Because of this effect only traces recorded with increasing field are shown. Some of the microwave-energy $T(B)/T(0)$ traces are shown Fig. 4.12.

The most interesting aspect of these traces at constant radiation energy is that the changes near the phase transitions are quasi-steplike, reminiscent of the steps in the Hall voltage. At low frequencies the sample reflectivity, proportional to $T(B)/T(0)$, generally decreases with field. It would indicate a smaller conductivity, in agreement with the

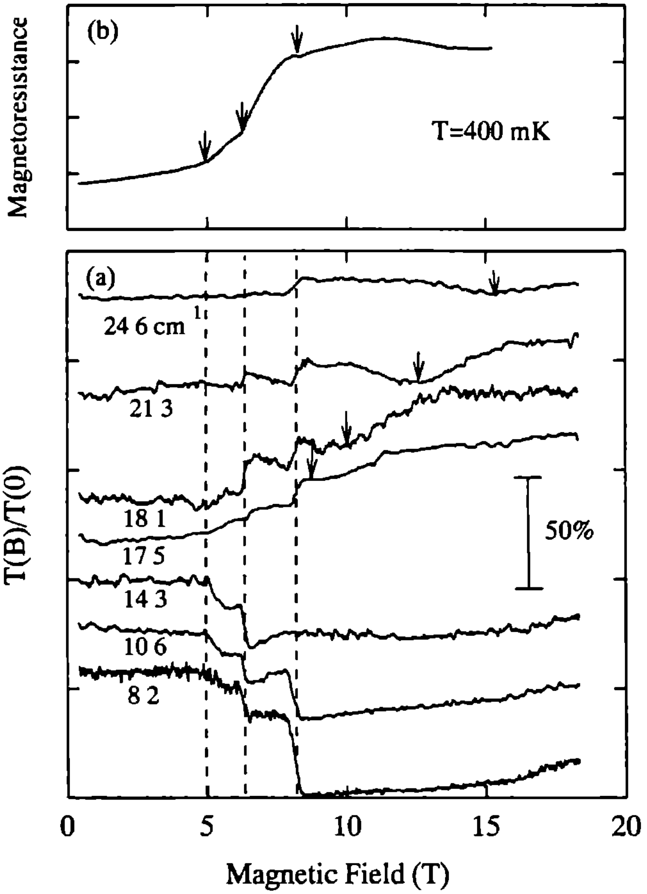

Figure 4.10 (a) Transmission (normalized to transmission at $B = 0$) versus magnetic field for different frequencies both below and above the SDW gap The arrows indicate the cyclotron resonance Dashed lines correspond to the fields where magnetoresistance steps were observed, as shown in (b) (b) Magnetoresistance of the reference sample, where arrows indicate the phase transitions between the FI-SDW subphases.

opening of a (partial) gap in the excitation spectrum A remarkable exception is the behaviour in a narrow range around 2 4 cm^{-1}, where $T(B)/T(0)$ sharply increases At frequencies above 14 cm^{-1} $T(B)/T(0)$ increases at the phase transitions, as one would expect when the single particle density of states piles up above the gap edge Normalized FIR spectra are shown in Fig 4 11, showing the complete energy dependence. The spectra in magnetic field are normalized to the zero field transmission spectrum The data taken

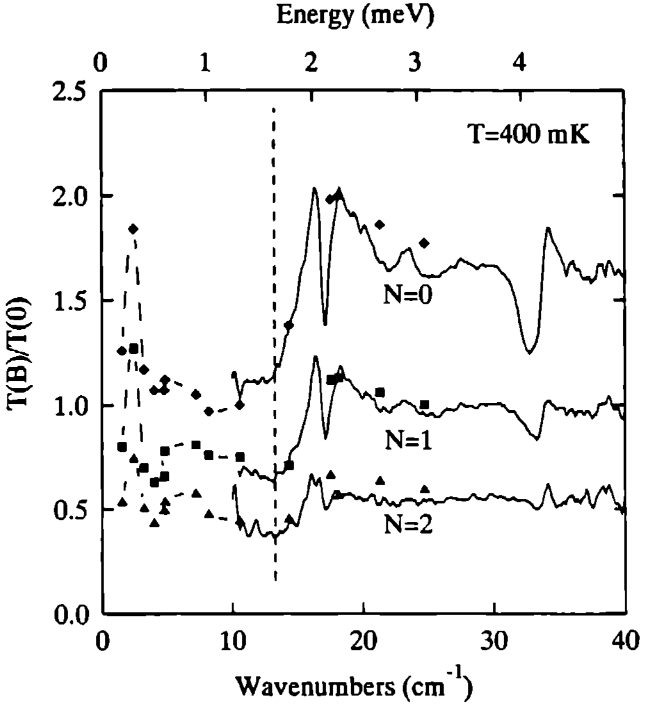

Figure 4.11 FIR spectra (normalized to the $B = 0$ spectrum) for three different magnetic fields corresponding to the $N = 0, 1$, and 2 FI-SDW subphases. The microwave and FIR laser data are indicated by the different symbols. The upper and lower spectrum have been offset by ±0.5 for clarity.

symbols. For fields between the thresholds for different phase transitions the spectra were virtually identical, so we have limited the data to the three generic spectra that are shown in this figure. For historical reasons we labeled the FI-SDW phases with index N=2,1,0 corresponding to fields of 6, 7.5, and 8 T. More spectra at fields up to 15 T have been taken but these did not substantially differ from the 8 T spectrum. In Fig. 4.11 several features can be identified:(a) a large decrease is found for $T(B)/T(0)$, below approximately 14 cm^{-1} in all FI-SDW phases, indicating the opening of a (partial) gap. Note that the energy of the gap is the same in all subphases. (b) Sharp spectral features at 17 and 32 cm^{-1} appear suddenly with the formation of each SDW subphase. A smaller structure appears near 23 cm^{-1}. (c) Finally, a resonance peak at 2.4 cm^{-1} is found. All features become more pronounced at higher fields or equivalently for lower FI-SDW index. However, none of them tend to shift in energy with increasing magnetic fields.

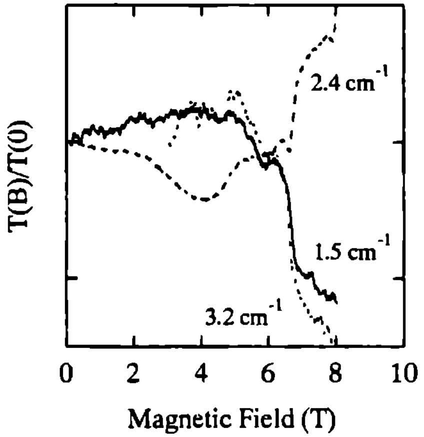

Figure 4.12 Field dependence of the normalized transmission through the grid of samples for three frequencies in the microwave regime.

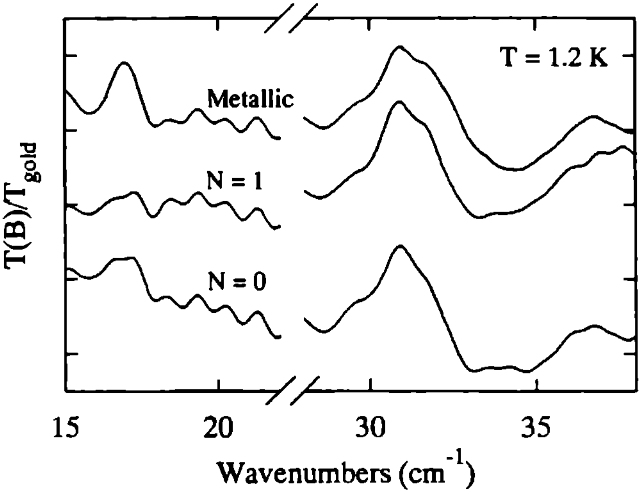

Figure 4.13 Normalized transmission spectra (using a reference spectrum taken on a gold coated sample) in two FI-SDW states and the low field metallic state.

4.3.3 Discussion

The main feature in the spectra is the opening of a gap below 14 cm^{-1}. This value is slightly higher than that estimated from the 1.2 K reflectivity in the previous section, however still within the accuracy which can be expected from the monochromatic experiment.

In a theoretical treatment to explain the quasi-quantized Hall behaviour, Montambaux *et al.* [22] assumed a constant carrier density and concluded that a multiplet of gaps would form, separating Landau-like bands. As a consequence the magnitude of the gaps would be strongly field dependent and change discontinuously between the various SDW subphases.

Our spectroscopic results do not confirm this picture. We find no evidence for multiple gaps, and more specifically, our data show that the fundamental gap is independent of the magnetic field or subphase index. However, the signal strength in the gap is not zero but does depend on the subphase index. We must conclude that the gap is not uniform in k-space.

To explain the data we propose the following simple qualitative model: When the field increases, the system will become more sensitive to a nesting instability, part of the charge carriers condense into a collective SDW ground state and it will take a finite amount of energy (the gap) to create a free electron excitation. In the original treatment of Gor'kov and Lebed' [20] the free energy of the system is lowest if the area of the normal carrier pockets on the Fermi surface is quantized. The total gapped area, or equivalently the density of electrons in the collective state will increase discontinuously upon each phase transition. (This agrees with the general observation of an increase of the magnetoresistance and a stepwise increase of the Hall voltage.)

The enhancement of the reflectivity above the gap is qualitatively in accordance with a sum rule conservation of the total oscillator strength for the electronic excitations, with only part of the total strength transferred to a collective mode. We associate the low frequency resonance at 2.4 cm^{-1} in Fig. 4.11 with this collective mode. Both the extreme low frequency (well inside the SDW gap) and the magnetic field dependent behaviour of the resonance support this assignment. A somewhat surprising result is the fact that the collective mode appears at a rather high frequency (still much lower than the phonon modes) in comparison with the collective mode observed in $(TMTSF)_2PF_6$ [64]. This could indicate a strong pinning of the electronic modulation to the lattice defects. In contrast to CDW systems, such a pinning is not expected for SDW's.

The interaction of the SDW formation with the lattice is also obvious from the change in the phonon response, especially near 32 cm^{-1}. This phonon is expected to be basically an acoustic mode, which becomes FIR active because of the zone folding caused by the ClO_4 anion ordering transition [65]. This mode is depicted in more detail in Fig. 4.13, where the transmission signal is normalized to the transmission of the same sample after it had been coating with gold. The 31 cm^{-1} phonon mode is distorted from a simple Lorentzian, partly due to the varying dielectric constant in this frequency region. However, it is clear that, especially in the $N = 0$ SDW state the phonon lineshape changes and becomes more asymmetric. This indicates an enhanced coupling of this phonon to the electronic system in the SDW state. Part of this coupling could result from the opening of the gap, which shifts electronic spectral weight to higher frequencies closer to the phonon frequency.

The origin of the feature around 17 cm^{-1} is not understood. One could speculate

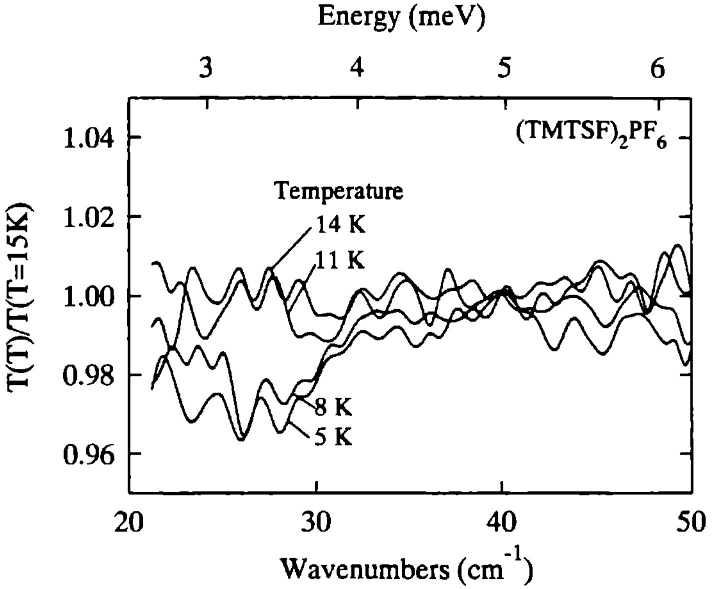

Figure 4.14 Normalized transmission spectra (using 15 K spectra) through a grid of (TMTSF)$_2$PF$_6$ crystals at 4 different temperatures around the SDW phase transition.

the phonon dispersion and induces new FIR active modes that correspond to the original acoustic mode. For a quarter filled band and a $2k_F$ modulation this would lead to additional modes at about half of the zone folding 32 cm^{-1} mode induced by the anion ordering. Contradicting this supposition is the observation of this phonon mode in the zero field (metallic state) spectra in Fig. 4.13. It slightly shifts in frequency with magnetic field and becomes very asymmetric in the SDW phases. This fact makes a mechanism via double folding due SDW formation unlikely. This phonon is therefore more likely to be another zone folded acoustic phonon not previously observed by other workers [65,67,68]. It probably appears distorted at higher fields due to large changes in the dielectric response very close to the gap.

Tanaka *et al.* [69] performed a temperature dependent transmission experiment on a related material, MEM(TCNQ)$_2$ which exhibits a spin-Peierls transition below 19 K. Below this spin-Peierls transition temperature dependent and independent phonon modes were observed as a result of crystal changes and zone folding associated with the spin-Peierls transition. One could speculate that the 14 cm^{-1} feature observed in our spectra is not the SDW gap but instead a phonon mode of the kind observed by Tanaka and coworkers. In order to check the assignment of the 14 cm^{-1} edge to the SDW gap we performed FIR measurements on a similar grid of (TMTSF)$_2$PF$_6$ crystals, which exhibit a SDW state at low temperatures in zero field. From absorption experiments [64,70] the of measuring transmission through a grid. In Fig. 4.14 several spectra are shown, measured both above and below the SDW ordering temperature which is 12 K at ambient pressure for this material. The spectra are of considerable lower quality then those obtained on $(TMTSF)_2ClO_4$ crystals due to the poor crystal quality of the $(TMTSF)_2PF_6$ batch available. Below the SDW ordering temperature a decrease of the transmission signal below 32 cm^{-1} is observed. Near this edge we find no visible phonon structure in the spectra, and indeed there is no corresponding feature to be expected due to zone folding because there is no anion disorder in the centro-symmetric PF_6 compound. Assigning this edge to the opening of the SDW gap, we indeed find that the size of this gap is about twice as large as the sharp edge in the $(TMTSF)_2ClO_4$ spectra, in accordance with the twice as large value of T_{SDW} in $(TMTSF)_2PF_6$.

A final remark concerns the appearance of broad shallow dips in the field dependent data, marked in Fig. 4.10(a) by arrows. When compared with the work in the previous section at higher temperature, the number and sharpness of these features, which are interpreted as the cyclotron resonance of free carriers, is considerably reduced. This result is consistent with the general observation [12] that Landau level type behaviour is thermally activated below $T_{SDW}(B)$ in this material. We calculate the effective mass to be m^*=0.7 m_e which is in the range of values found in the previous section.

4.3.4 Summary

Spectroscopic evidence has been presented that the gap in the field induced spin-density-wave state is independent of the value of the magnetic field. The data are consistent with a stepwise increase of the carrier density in the condensed SDW ground state upon each phase transition into a lower index subphase. In addition, the first indication of a collective mode excitation in the microwave region is reported, and of an enhanced coupling of the 31 cm^{-1} zone folding phonon mode with the electronic system as a result of SDW formation.

4.4 Temperature dependence of the excitation spectrum in $(TMTSF)_2ClO_4$

In the previous section we established the low temperature magnetic field induced excitation spectrum of $(TMTSF)_2ClO_4$. In principle the spectrum was found to consist of two parts; a contribution from single particle excitations across the SDW gap, and a collective mode resonance originating from the excitation of the density-wave itself at a pinning frequency inside the SDW gap. This spectrum is in many respects similar to that known from CDW compounds [71]. However, such a spectrum is not theoretically expected for SDW systems [27].

In a CDW the dynamical mass m^* of the density-wave is strongly enhanced over the band mass m_b, because it is associated with a large lattice distortion. The CDW collective mode resonance appears with m_b/m^* oscillator weight at zero frequency or at a finite frequency if pinned to lattice imperfections. The single particle excitations occur with oscillator weight $(1 - m_b/m^*)$ commencing at the gap [27]. In the ideal SDW case m^* equals m_b, because the SDW does not interact with the lattice. Hence, the single particle contribution to the excitation spectrum would be zero with all oscillator strength concentrated at the zero frequency collective mode [28]. As shown in the previous section this is far from being the case since we do observe both collective and single particle contributions. Other experiments also indicate that the SDW is strongly pinned to the lattice [72] with a SDW dynamical mass enhanced over the band mass [64]. To explain this behaviour one generally assumes that the SDW is pinned via impurities in the lattice [73]. Alternatively, it has been predicted that Coulomb repulsion could raise the collective contribution to finite frequencies [74]. However, the understanding of these mechanisms is still far from complete.

In this section we present a magneto-optical study of the excitation spectrum of $(TMTSF)_2ClO_4$ covering the phase diagram around the FI-SDW threshold fields. The observed transition temperatures of the various FI-SDW subphases follow closely the phase diagram derived from transport data. From the excitation spectra we derive the magnitude of the SDW gap as a function of temperature. In addition we find evidence of a developing collective mode excitation in the gap with decreasing temperature, confirming the relatively strong pinning of the SDW to the lattice. Finally we present novel hysteresis and memory effects near the FI-SDW phase transitions which might point to the direction of a possible new mechanism for coupling between the condensed SDW electrons and the lattice.

4.4.1 Experimental details

Basically the experimental setup was identical to the one described in section 4.3.1 except that a heater, capacitance sensor and calibrated Allen-Bradley temperature sensor were incorporated, which allowed precise control of the sample temperature in a range from 0.4 to 7 K without essentially affecting the bolometer sensitivity. In addition we used a slow-scan Grubb-Parsons interferometer with either a 50 μm beamsplitter, or a 250 μm beamsplitter which enabled us to measure down to 2 cm^{-1}.

4.4.2 Results

In Fig. 4.15 normalized transmission spectra taken at monochromatic energies are shown for a set of temperatures covering the phase diagram of $(TMTSF)_2ClO_4$. The laser was tuned to 8.3 cm^{-1} which corresponds to an energy well within the SDW gap. With increasing temperature the number of FI-SDW phase transitions decreases and those still present move to higher magnetic fields. The transition field at each temperature is taken as the midpoint of the steps in the transmission signal. The points thus acquired in the phase diagram have been plotted in Fig. 4.16, together with the specific heat data of Fortune *et al.* [15].

In Fig. 4.17 we show the complete energy spectrum as a function of temperature for a magnetic field of 10 T measured with a slow-scan Fourier interferometer optimized in the long wavelength region. At this field we probe only the $N = 0$ FI-SDW phase. The

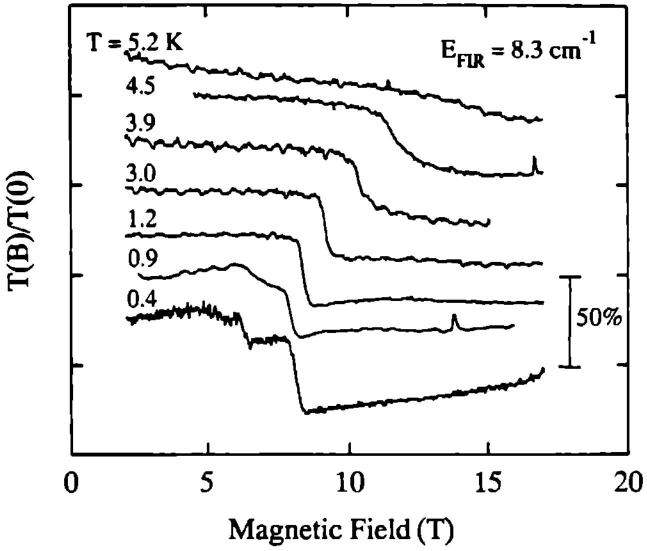

Figure 4.15 Normalized transmission spectra $T(B)/T(0)$ versus magnetic field at different sample temperatures at 8.3 cm^{-1}. The traces are offset for clarity.

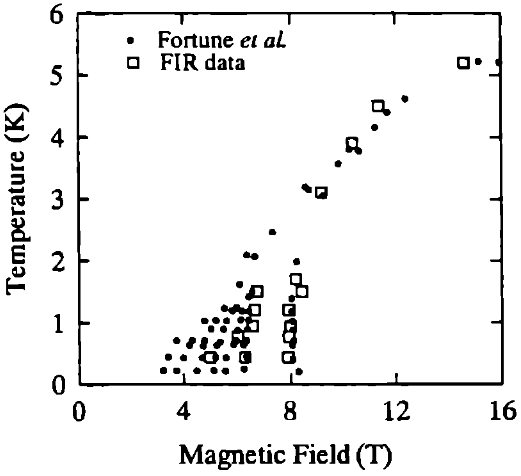

Figure 4.16 Phase diagram composed of the FIR transmission data. Here the midpoints of the transitions such as in Fig. 4.15 have been used. The specific heat data reproduced from Fortune *et al.* [15] are shown for comparison.

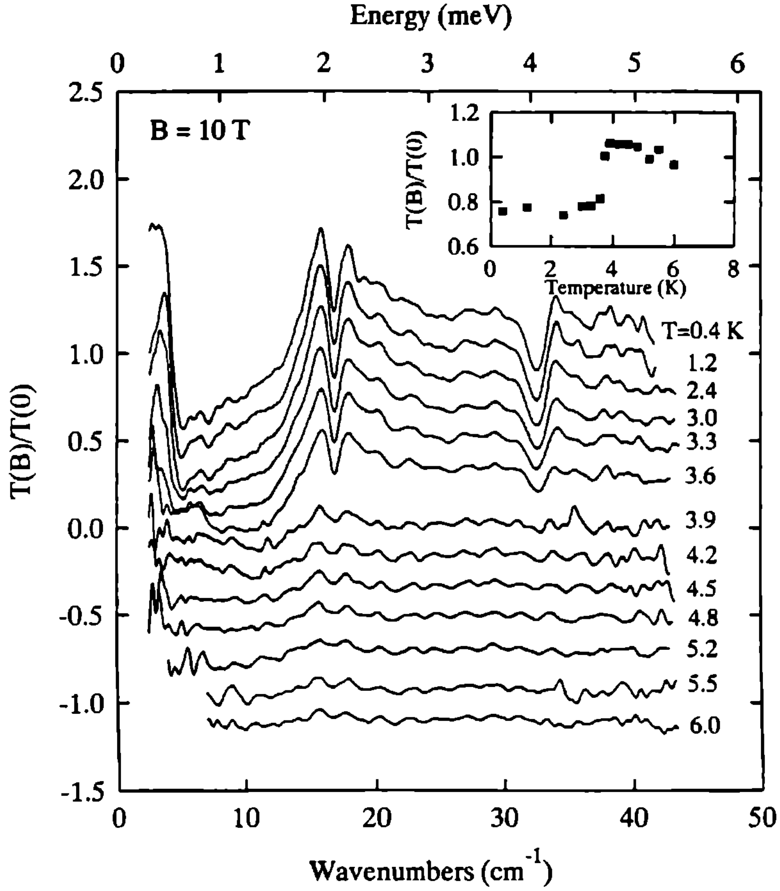

Figure 4.17 Normalized spectra (using zero field spectra at the same temperature) as a function of frequency at various temperatures and a magnetic field of 10 T. The spectra taken with 50 and 250 μm beamsplitter are merged together. The traces are offset for clarity. Inset: Plot of the signal intensities at (9.5 cm^{-1}) within the SDW gap as a function of temperature.

spectra were normalized using zero field spectra taken at the same temperature, hence dividing out any temperature dependence of the bolometer. The signal strength inside the gap remains nearly constant with increasing temperature until the transition temperature is reached. A remarkable feature in the spectra is the remnants of shallow structure above T_{SDW}. For a magnetic field of 10 T, T_{SDW} would be $\approx$ 4 K. This effect is more evident from the inset in Fig. 4.17 where the normalized signal intensities at 9.5 cm^{-1} well within the gap are plotted versus temperature.

After all measurements were performed a layer of gold was evaporated onto the

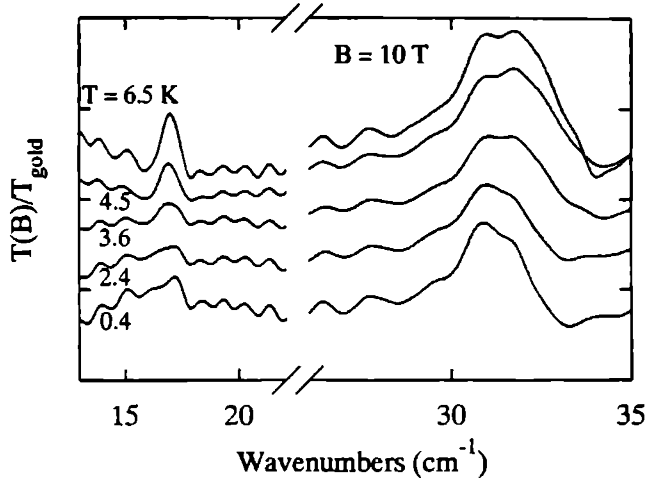

Figure 4.18 Normalized spectra (using reference spectra on a gold coated sample at the same temperature) at 10 T for several different temperatures both above and below the SDW phase transition temperature. The spectra are offset for clarity.

sample. This was done from different angles to obtain complete coverage also in between the crystals. All measurements were then repeated in order to obtain reference spectra. Unfortunately, due to small alignment and source intensity changes in the time elapsed between the sample and reference spectra, the quality of the normalized spectra was poor. In spectroscopic studies of organic materials it is common practice to perform a Kramers-Kronig analysis on the normalized spectra obtained with a reference spectrum of a gold coated sample. However, the conductivities thus obtained are not very accurate and show a large difference in magnitude due to irregular crystal surfaces and openings in between the separate crystals [26]. For a transmission-type experiment on a grid of crystals as used by us these effects would be even more severe. Therefore we omitted such an analysis and only base our analysis on the changes directly observable in the spectra. Nevertheless, the normalized spectra do reveal a clear change in phonon lineshape when the temperature changes through the phase transition. This is demonstrated in Fig. 4.18 where the details of the 17 and 31 cm^{-1} phonon modes are shown for a few temperatures above and below T_{SDW} at 10 T.

4.4.3 Discussion

The monochromatic data summarized in Fig. 4.15 for different temperatures show an identical behaviour to the data presented in Fig. 4.10(a) in section 4.3.2. With increasing temperature we find the resolved FI-SDW phase transitions to decrease in number and to shift to higher fields. At low temperatures the transitions occur almost discontinuously within a very narrow field range, indicative of a first order nature of these phase transitions. At higher temperatures the transitions are broadened and the change in the FIR transmission becomes smaller, probably related to the thermally excited carriers above the SDW gap. The overall agreement with the specific heat data (see Fig. 4.16) is quite good, giving confidence that we are indeed optically probing the SDW formation. The conclusion of the previous section was that the gap is not uniform in k-space, and that in all subphases there is a remaining free carrier density, related to the ungapped area of the Fermi surface. The present data are consistent with this conclusion.

In the energy spectra in Fig. 4.17 we observe a gap-like structure below 14 cm^{-1} similar to the low temperature data in Fig. 4.11 for the $N = 0$ FI-SDW phase. With increasing temperature the gap edge does not shift to lower energies, as one would expect in a mean field picture, but remains at a fixed position. The signal strength inside the gap depicted in the inset of Fig. 4.17 remains nearly constant with increasing temperature up to the phase transition. Again, this behaviour is quite different from BCS-like mean field predictions. The fact that, above T_{SDW}, shallow remnants of the gap remain visible is unexpected in a mean field model and indicates a possible presence of SDW fluctuations with no long range magnetic order. Fluctuations are an issue which have lead to a lot of debate in the past [75,76]. Evidence is conclusive that the phase boundary of $(\text{TMTSF})_2\text{ClO}_4$ is second order up to a temperature of 3 K where the subphases disappear; the subphase transitions themselves are thought to be first order [9,10]. Above 3 K the magnetization data indicate a first order phase transition [9], contradicting the specific heat measurements which point to a second order transition [15]. Furthermore, in our data hysteresis is observed at the phase transition also above 3 K like for the subphase transitions, which points rather to a first order transition. Fluctuations are predicted to be present in anisotropic conductors but would be strongly suppressed for a second order phase transition. Perhaps the origin of the shallow structure is less subtle than proposed above, and caused by the inability of the heater to maintain the proper sample temperature at the highest temperatures during the measurement. However, the fact that in the experiments with monochromatic energies the exact phase diagram can be reproduced, indicates that the sample temperature is correct.

At low frequencies we find in Fig. 4.17 a strong excitation mode which slightly hardens when going to lower temperatures. This confirms the earlier observation of this mode with monochromatic microwave sources shown in Fig. 4.12 of section 4.3.2. Although the relative accuracy decreases near the extreme low frequency end of the spectrum, it is clear that the intensity of this mode is weakly temperature dependent until it vanishes near the critical temperature. This is in agreement to its interpretation as a collective mode excitation of the SDW state, where the hardening at low temperatures is due to a more effective pinning of the condensate. To unequivocally observe this hardening, additional measurements down to lower frequencies will be necessary.

The phonon features observed in the spectra in Fig. 4.17 also change when changing from the metallic state to the SDW state below T_{SDW}. As mentioned before these are probably both related to zone folding due to the anion ordering superlattice. We find a strong change in the phonon lineshape when lowering the temperature into the SDW coated sample (Fig. 4.18) it is indeed clear that the 17 cm^{-1} phonon peak decreases in intensity and becomes strongly asymmetric, again similar to the case where the magnetic field changes the SDW subphases (Fig. 4.13). This could be due to an increased coupling to the electronic excitations just above the SDW gap. A similar effect appears at the high energy side of the 32 cm^{-1} phonon structure. These changes, although unexpected for SDW systems, are in themselves not very surprising given the additional incommensurate modulation which breaks the translation symmetry and changes the selection rules for optically active ($k = 0$) phonon modes. However, it must be noted that both phonons are also present in the metallic state and the major effect of the SDW formation is a change in lineshape.

4.4.4 Hysteresis and memory effects

In this last section we want to discuss some interesting hysteresis and memory effects observed in the experiments taken with microwave sources at energies well within the SDW gap. Normally the hysteresis observed in magnetotransport measurements at the last SDW phase transition depends on how far the magnetic field has been swept beyond the threshold field. In Fig. 4.19(a), a field sweep at 7.2 cm^{-1} is shown. When the field was swept up, we found the signal to show the usual steps at the FI-SDW transition fields. Just after the $N = 0$ SDW state was entered, the magnetic field sweep was stopped, and the field was held constant at 8.0 T. During the pause the transmission signal very slowly (on the time scale of minutes) relaxed back to the level corresponding to the previous $N = 1$ subphase. When after about 20 minutes the field was swept down, the signal was found to drop again to the level of the $N = 0$ state. At even lower fields the transmission rose again and after this the usual steps of the phase transition were observed. Fig. 4.19(b) shows the signal intensity at a the magnetic field of 8.0 T versus time for an initial sweep rate of 0.04 T/min. At this slow sweep rate induction effects in the magnetic field or temperature changes due to sweeping of the magnetic field can be estimated to be insignificantly small.

The time scale for the relaxation is very long, in the order of minutes; this suggests either the presence of domain formation or possibly some sort of coupling to the nuclear spins of the organic molecules. The fact that the system relaxes back to the $N = 1$ state after it already made the transition to the $N = 0$ state rules out hysteresis effects. The nucleation of domain structures also seems unlikely because the system already made the full phase transition. Furthermore, on the down sweep the transition occurs on a much shorter timescale. The appearance of a memory effect while sweeping down in field suggests the build up of an internal magnetic field. A similar sort of effect was first predicted by Overhauser [77] for metallic systems. He suggested that microwave energies are capable of saturating the electronic system via electron-spin-resonance (ESR). The electron system will then effectively polarize the nuclei via paramagnetic relaxation processes that can occur by means of the hyperfine interaction between electrons and nuclei. Such a strong nuclear polarization has been observed by Dobers *et al.* [78] in an ESR experiment on GaAs-(Ga,Al)As heterostructures. In the present system one could envision a similar effect where the electronic system carries a stationary magnetic moment which varies in

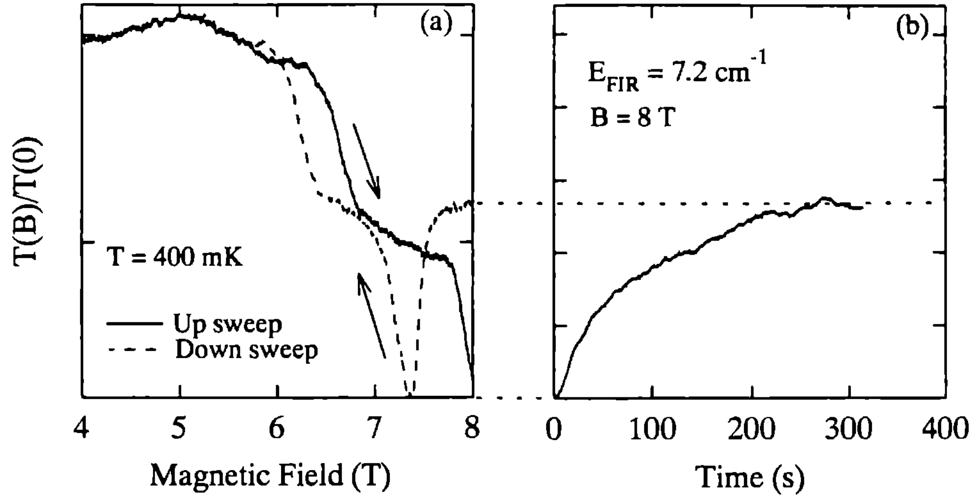

Figure 4.19 (a) Up and down sweep for the transmission signal at microwave energy of 7.2 cm^{-1}, showing a anomalous hysteresis. (b) Transmission signal versus time after an up-sweep to 8 T.

space. The hyperfine interaction could effectively induce a coupled magnetization of the nuclei (presumably Se or H) with the same periodicity as the electronic SDW. This mechanism implies that memory effects could also appear in non-optical experiments. With NMR experiments, Azevedo *et al.* [44] estimated the local field in $(TMTSF)_2ClO_4$ to be at least of the order of 0.1 T on the Selenium sites. A very slow proton relaxation rate (minutes) was observed in the FI-SDW states indicating a change in relaxation mechanism at the phase transition. Because the FI-SDW formation is the result of a delicate energy balance it is possible that the lowest energy state for a given external field in the presence of the polarized nuclei is different from the state without polarization. This kind of coupling could also be the origin of the frequently observed hysteresis effects near the SDW transitions. It could also explain the unusual pinning of the SDW electronic ground state to the lattice. A possible check for the mechanism will be to quench the relaxation effect via saturation of the nuclear spins with RF radiation [78]. In that case no spin-flip process can take place due to absence of empty levels in the nuclei, as a result the up and down sweep in the experiment should appear unshifted, without the memory effect.

4.4.5 Summary

We have presented spectroscopic data on the temperature dependence of the FI-SDW formation in $(TMTSF)_2ClO_4$. The value of the SDW gap is relatively insensitive to temperature. The phase transitions as a function of temperature at high magnetic fields, as well as the phase transitions as a function of magnetic field at low temperatures are established from thermodynamic measurements. Above T_{SDW} some shallow gap structure in the spectra remains. This indicates possible fluctuations of the FI-SDW state. We confirm the presence of a collective mode near 2.4 cm^{-1} which is weakly temperature dependent, indicating possible depinning at higher temperatures. In addition we report the measurement of peculiar memory effects near the SDW subphase transitions, which suggest magnetic coupling to the lattice.

Acknowledgement: We are grateful to Paul Chaikin for providing the samples used.

References

1. K. Bechgaard, C.S. Jacobsen, K. Mortensen, J.H. Pederson, and N. Thorup, Solid State Commun. **33**, 1119 (1980).
2. D. Jérome, A. Mazaud, M. Ribault, and K. Bechgaard, J. Phys. (Paris) Lett. **41**, L95 (1980).
3. *Low Dimensional Conductors and Superconductors*, edited by D. Jérome and L. Caron, Nato Advanced Study Institute, Series B. Physics. **155** (Plenum, New York, 1987).
4. *Organic Superconductors*, by T. Ishiguro and K. Yamaji, Springer Series in Solid-State Sciences **88**, (Springer-Verlag, Berlin, 1990).
5. J.F. Kwak, J.E. Schirber, R.L. Greene, and E.M. Engler, Phys. Rev. Lett. **46**, 1296 (1981).
6. H. Bando, K. Oshima, M. Suzuki, H. Kobayashi, and G. Saito, J. Phys. Soc. Jpn. **51**, 2711 (1982).
7. P.M. Chaikin, M.Y. Choi, J.F. Kwak, J.S. Brooks, K.P. Martin, M.J. Naughton, E.M. Engler, and R.L. Greene, Phys. Rev. Lett. **51**, 2333 (1983).
8. K. Kajimura, H. Tokumoto, M. Tokumoto, K. Murata, T. Ukachi, H. Anzai, T. Ishiguro, and G. Saito, J. Phys. (Paris) Colloq. **44**, C3-1059 (1983).
9. M.J. Naughton, J.S. Brooks, L.Y. Chiang, R.V. Chamberlin, and P.M. Chaikin, Phys. Rev. Lett. **55**, 969 (1985).
10. F. Pesty, P. Garoche, and K. Bechgaard, Phys. Rev. Lett. **55**, 2495 (1985).
11. R.V. Chamberlin, M.J. Naughton, X. Yan, L.Y. Chiang, S.Y. Hsu, and P.M. Chaikin, Phys. Rev. Lett. **60**, 1189 (1988).
12. X. Yan, M.J. Naughton, R.V. Chamberlin, S.Y. Hsu, L.Y. Chiang, J.S. Brooks, and P.M. Chaikin, Phys. Rev. B **36**, 1799 (1987).
13. M.J. Naughton, R.V. Chamberlin, X. Yan, S.Y. Hsu, L.Y. Chiang, M.Y. Azbel, and P.M. Chaikin, Phys. Rev. Lett. **61**, 621 (1988).
14. R.C. Yu, L.Y. Chiang, R. Upasani, and P.M. Chaikin, Phys. Rev. Lett. **65**, 2458 (1990).
15. N.A. Fortune, J.S. Brooks, M.J. Graf, G. Montambaux, L.Y. Chiang, J.A.A.J. Perenboom, and D. Althof, Phys. Rev. Lett. **64**, 621 (1988).
16. W. Kang, S.T. Hannash, and P.M. Chaikin, Phys. Rev. Lett. **70**, 3091 (1993).
17. V.M. Yakovenko, Sov. Phys. JETP **66**, 355 (1987).

18. A.G. Lebed' and Per Bak, Phys. Rev. B **40**, 11433 (1989).
19. T. Osada, S. Kagoshima, and M. Miura, Phys. Rev. Lett. **69**, 1117 (1992).
20. L.P. Gor'kov and A.G. Lebed', J. Phys. (Paris) Lett. **45**, L4333 (1984).
21. M. Héritier, G. Montambaux, and P. Lederer, J. Phys. (Paris) Lett. **45**, L943 (1984).
22. G. Montambaux, M. Heritier, and P. Lederer, Phys. Rev. Lett. **55**, 2078 (1985).
23. K. Yamaji, J. Phys. Soc. Jpn. **54**, 1034 (1985).
24. G. Montambaux and D. Poilblanc, Phys. Rev. B **37**, 1913 (1988).
25. G. Montambaux, M.J. Naughton, R.V. Chamberlin, X. Yan, P.M. Chaikin, and M.Y. Azbel, Phys. Rev. B **39**, 885 (1989).
26. T. Timusk and C.S. Jacobsen in: *Low Dimensional Conductors and Superconductors*, edited by D. Jérome and L.G. Caron (Plenum, New York, 1987) p. 253 and p. 275.
27. P.A. Lee, T.M. Rice, and P.W. Anderson, Solid State Commun. **14**, 703 (1984).
28. E.W. Fenton and G.C. Psaltakis, Solid State Commun. **47**, 767 (1983).
29. K. Bechgaard, Mol. Cryst. Liq. Cryst. **79**, 1 (1982).
30. T. Mori, A. Kobayashi, Y. Sasaki, and H. Kobayashi, Chem. Lett. **1982**, 1923 (1982).
31. P.M. Grant, Phys. Rev. B **26**, 6888 (1982).
32. P.M. Grant, Phys. Rev. Lett. **50**, 1005 (1983).
33. K. Yamaji, J. Phys. Soc. Jpn. **55**, 860 (1986).
34. H. Schwenk, K. Andres, and F. Wudl, Phys. Rev. B **29**, 500 (1984).
35. J.P. Pouget, G. Shirane, K. Bechgaard, and J.M. Fabre, Phys. Rev. B **27**, 5203 (1983).
36. K. Bechgaard, K. Carneiro, M. Olsen, F.B. Rasmussen, and C.S. Jacobsen, Phys. Rev. Lett. **46**, 852 (1981).
37. K. Mortensen, C.S. Jacobsen, A. Lindergaard-Andersen, and K. Bechgaard, J. Physique C **44**, 963 (1983).
38. R.E. Peierls: *Quantum Theory of Solids*, (Oxford Univ. Press, London 1955).
39. K. Mortensen, Y. Tomkiewicz, T.D. Schultz, and E.M. Engler, Phys. Rev. Lett. **46**, 1234 (1981).
40. G. Soda, D. Jérome, M. Weger, J. Alizon, J. Gallice, H. Robert, J.M. Fabre, and L. Giral, J. Phys. (Paris) **38**, 931 (1977).
41. J.E. Hirsch, Phys. Rev. Lett. **51**, 296 (1983).
42. K. Yamaji, J. Phys. Soc. Jpn. **52**, 1361 (1983).
43. P.M. Chaikin, M.Y. Choi, and R.L. Green, J. Phys. (Paris) Colloq. **44**, C3-783 (1983)
44. L.J. Azevedo, J.M. Williams, and S.J. Compton, Phys. Rev. B **28**, 6600 (1983).
45. P.M. Chaikin, Phys. Rev. B **31**, 4770 (1985).
46. P.M. Chaikin, T. Holstein, and M. Ya. Azbel, Philos. Mag. B **48**, 457 (1983).
47. A. Virosztek, L. Chen, and K. Maki, Phys. Rev. B **34**, 3371 (1986).
48. J.F. Kwak, J.E. Schirber, P.M. Chaikin, J.M. Williams, H.H. Wang, and L.Y. Chiang Phys. Rev. Lett. **63**, 972 (1986).
49. V.M. Yakovenko, Phys. Rev. Lett. **61**, 2276 (1988).
50. M. Ribault, D. Jérome, J. Yuchendler, C. Weyl, and K. Bechgaard, J. Phys. (Paris Lett. **44**, L953 (1983).
51. S.T. Hannahs, J.S. Brooks, W. Kang, L.Y. Chiang, and P.M. Chaikin, Phys. Rev

52. J.R. Cooper, W. Kang, P. Auban, G. Montambaux, D. Jérome, and K. Bechgaard, Phys. Rev. Lett. **63**, 1984 (1989).
53. H. Sigg, H.J.A. Bluyssen, and P. Wyder, IEEE J. Quantum Electron, **QE-20**, 616 (1984).
54. C.J.G.M. Langerak, Ph.D. thesis, University of Nijmegen (1990), unpublished. Many of the techniques used in this work are given here.
55. H.K. Ng, T. Timusk, and K. Bechgaard, Mol. Cryst. Liq. Cryst. **119**, 191 (1985).
56. M. Takigawa and G. Saito, Physica B **143**, 442 (1986).
57. T. Ando, J. Phys. Soc. Jpn. **38**, 989 (1975).
58. R.V. Chamberlin, M.J. Naughton, X. Yan, and P.M. Chaikin, Phys. Rev. Lett. **61**, 2277 (1988).
59. J.P. Ulmet, A. Khmou, P. Auban, and L. Bachere, Solid State Commun. **58**, 753 (1986).
60. H.K. Ng, T. Timusk, D. Jérome, and K. Bechgaard, Phys. Rev. B **32**, 8041 (1985).
61. K. Kornelsen, J.E. Eldridge, and G.S. Bates, Phys. Rev. B **35**, 9162 (1987).
62. S. Marianer, M. Kaveh, and M. Weger, Phys. Rev. B **25**, 519 (1982).
63. H.K. Ng, T. Timusk, and K. Bechgaard, Phys. Rev. B **30**, 5842 (1984).
64. D. Quinlivan, Y. Kim, K. Holczer, G. Grüner, and F. Wudl, Phys. Rev. Lett. **65**, 1816 (1990).
65. J.E. Eldridge, C.C. Holmes, F.E. Bates, and G.S. Bates, Phys. Rev. B **32**, 5156 (1985).
66. H.K. Ng, T. Timusk, J.M. Delrieu, D. Jérome, K. Bechgaard, and J.M. Fabre, J. Phys. (Paris) Lett. **43**, L513 (1982).
67. H.K. Ng, T. Timusk, and K. Bechgaard, J. Phys. (Paris) Colloq. **44**, C3-867 (1983).
68. C.S. Jacobsen, D.B. Tanner, K. Bechgaard, Phys. Rev. B **28**, 7019 (1983).
69. Y. Tanaka, N. Satoh, and K. Nagasaka, J. Phys. Soc. Jpn. **59**, 319 (1990).
70. J.E. Eldridge and G.S. Bates, Mol. Cryst. Liq. Cryst. **119**, 181 (1985).
71. G. Grüner, Rev. Mod. Phys. **60**, 1129 (1988).
72. G. Kriza, G. Quiron, O. Traetteberg, and D. Jérome, Phys. Rev. Lett. **66**, 1264 (1991).
73. W. Kang, S. Tomić, and D. Jérome, Phys. Rev. B **43**, 1264 (1991).
74. K. Maki and G. Grüner, Phys. Rev. Lett. **66**, 782 (1991).
75. D. Jérome and H.J. Schulz, Adv. Phys. **31**, 299 (1982).
76. H. Bando, K. Kajimura, H. Anzai, T. Ishiguro, and G. Saito, Mol. Cryst. Liq. Cryst **119**, 41 (1985).
77. A.W. Overhauser, Phys. Rev. Lett. **2**, 411 (1953).
78. M. Dobers, K. von Klitzing, J. Schneider, G. Weimann, and K. Ploog in: *High Magnetic Fields in Semiconductor Physics II*, edited by G. Landwehr, Springer Series in Solid State Sciences **87**, 396 (1989).

Chapter 5

Cyclotron resonance of the quasi-2D organic conductor $(\mathrm{BEDT\text{-}TTF})_2\mathrm{KHg(SCN)}_4$

Parts of this work have been published in the following papers:

- Physica B **177**, 348 (1992).
- Phys. Rev. Lett **68**, 2500 (1992).
- Phys. Rev. B **45**, 13904 (1992).

5.1 Introduction

The charge-transfer salts of the molecule BEDT-TTF (bis-ethylenedithia-tetrathiafulvalene, or ET as we call it hereafter) exhibiting metallic behaviour down to low temperatures are mostly quasi-two-dimensional (quasi-2D): the family does however include several quasi-one-dimensional (quasi-1D) conductors, but most of these are nonmetallic at room temperature. The quasi-2D ET salts exhibit a myriad of different properties. By varying the anion X incorporated into the salt $(ET)_nX$, the stoichiometry and band filling may be adjusted, and compounds may be produced which are metallic, semimetallic, or semiconducting [1,2]. One member of this family provided us with the highest-temperature organic superconductor [3]; yet another combines antiferromagnetism with metallic conductivity [4,5,6]. The compounds are also of interest in the study of electron-electron interactions (EEI) in narrow-bandwidth metallic systems; a large enhancement of the transport effective mass over the predicted band mass in metallic $(BEDT\text{-}TTF)_2Cu(SCN)_2$ has been noted and associated with EEI [7,8].

Typical ET salts contrast with the TMTSF salts discussed in the previous chapter, in that they have generally quasi-2D electronic states. Circular motion of the electrons is than possible if a magnetic field is applied perpendicular to the two-dimensional plane. Through the properties of the electrons under the influence of the magnetic field, the size of the Fermi surface and the dynamical parameters of the electrons can be investigated, and such studies are contributing greatly to the understanding of these materials. Many studies on the organic ET salts have involved measurement of the Shubnikov-de Haas (SdH) oscillations in the magnetoresistance (MR) [9]; there have also been a few de Haas-van Alphen studies [10]. In contrast, no cyclotron resonance (CR) studies have been reported. CR measurements have an important role to play since, according to Kohn's theorem [11], the effective mass measured by CR is independent of EEI, giving the band mass renormalized only by electron-phonon interactions, whereas the transport mass, measured *e.g.* by SdH experiments, will be influenced additionally by EEI.

The compound studied in this work, $(ET)_2KHg(SCN)_4$, was originally synthesized as a likely superconducting modification of $(ET)_2Cu(SCN)_2$, but was found to be simply metallic down to 0.1 K [12]; the closely related salts $(ET)_2NH_4Hg(SCN)_4$ is, however, superconducting, with a critical temperature of 0.8 K [13]. $(ET)_2KHg(SCN)_4$ exhibits a number of features that distinguish it from other ET charge-transfer salts; for example, the material orders antiferromagnetically at $\sim$ 8 K [14]. In marked contrast to magnetically ordered charge-transfer salts of other molecules (*e.g.* TMTSF), $(ET)_2KHg(SCN)_4$ remains metallic below 8 K. At this point the temperature dependence of the electrical resistivity also changes slope and the magnetoresistance is dramatically enhanced [15]. At low temperatures and in high magnetic fields, the SdH oscillations are anomalous in form and sample dependent [9,14,15,16]. In addition, at around 22 T, there is a region of strong negative magnetoresistance known as the "kink" transition [16].

In this chapter we will report the far-infrared (FIR) optical measurements of the cyclotron mass of the closed orbit sections of the Fermi surface in metallic $(ET)_2KHg(SCN)_4$.

performed by us in order to elucidate features such as the anomalous SdH oscillations and the "kink" transition in this material. The magnetoresistance below the kink transition consists of two SdH oscillations which are thought to result from a band structure that is a modification of that calculated using the room-temperature crystal structure. The magnetoresistance above the kink shows a more simple behaviour as a consequence of a possible field-induced modification of the band structure. The cyclotron effective mass is compared with the renormalized transport mass calculated from the magneto-transport results. The transport effective mass is found to be several times higher than the cyclotron mass, providing clear evidence of the importance of electron-electron interactions in this material.

This chapter is organized as follows. In the next section (5.2), the crystal and band structure of (ET)$_2$KHg(SCN)$_4$ will be introduced. The magnetotransport results are discussed in section 5.3. Finally, in section 5.4 the cyclotron resonance measurements are presented and discussed.

5.2 Crystal and electronic structure

The crystal structure of (ET)$_2$KHg(SCN)$_4$ at room temperature is shown in Fig. 5.1 [12] and illustrates many of the typical structural properties of ET salts [1,2]. ET molecules (Fig. 5.1(a)) stack in the two-dimensional *ac*-plane (Fig. 5.1(b)) separated by layers of polymeric anions sheets of KHg(SCN)$_4$ in the *b*-direction (Fig. 5.1(c)). Transfer of electrons between ET molecules therefore occurs readily within the 2D planes, but much less readily in the perpendicular direction through the anion layers. Accordingly, an anisotropy in the conductivity (σ_c/σ_b) as large as 2000 at 1.2 K was reported, where σ_c and σ_b are the conductivity along and across the conducting plane, respectively [17]. As a result, the band structures and electrical properties of ET salts are rather 2D. This is different from the Bechgaard salts discussed in the previous chapter which are quasi-1D because of the weak side-by-side interaction between the 1D columns of TMTSF molecules. The ET molecules supply more π-electrons in the plane of the molecule so that the side-by-side overlap integrals between adjacent molecules are increased [18]. In addition, ET molecules are not planar and as a consequence the intracolumn S..S distance can be comparable with the intercolumn S..S distance, leading to the increased dimensionality.

Figure 5.2 shows the Brillouin zone and Fermi surface for (ET)$_2$KHg(SCN)$_4$ calculated by Mori *et al.* [19] with an extended Hückel Model using the room-temperature crystal structure. As in many ET salts, the Fermi surface consists of a quasi-1D open sheets (electrons) and a closed 2D hole pocket. The weak inter-plane coupling leads to a slight warping of the Fermi surface in the direction perpendicular to the 2D plane; i.e. the hole pocket in Fig. 5.2 is a warped cylinder, rather than a true 2D Fermi tube. ET salts with smaller anions (i.e. thinner anion layers) are less 2D, and hence have more strongly warped Fermi surfaces; in the case of (ET)$_2$I$_3$, both neck and belly orbits around the hole Fermi cylinder have been observed as beating of the SdH oscillations in [20].

In contrast to the TMTSF salts which from isomorphous crystal structures with different anions, the ET molecules form different types of compounds of varying composition

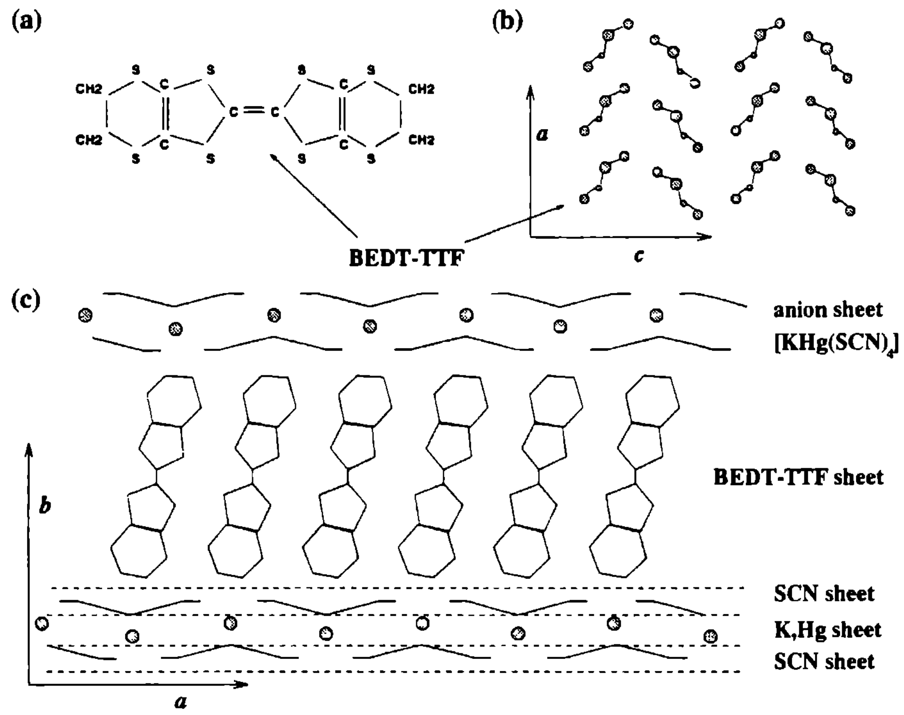

Figure 5.1 (a) Bis(ethylenedithio)tetrathiafulvalene molecule (BEDT-TTF or ET). Schematic crystal structure [12] of (BEDT-TTF)$_2$KHg(SCN)$_4$ at room temperature: (b) molecular stacking of BEDT-TTF, viewed along the molecular long axis, and (c) along the c-axis.

ratio and crystal structure. Even for the same anion molecule, different types of crystal structures are possible. Altering the anion causes changes in packing of the ET ions, enabling the molecular overlap and band-filling to be adjusted with sometimes dramatic results; *e.g.* the superconducting transition temperature T_c may be raised by a factor ~3 in the β-phase ET salts by changing the anion [1,2].

5.3 Magneto-transport results

Quasi-1D Fermi surfaces are prone to SDW (or CDW) formation (see *e.g.* the case of the quasi-1D TMTSF salts in the previous chapter), due to their almost perfect nesting characteristics [1,2]. The SDW leads to a band gap at the Fermi energy which results in a metal-insulator transition at low temperatures. In (ET)$_2$KHg(SCN)$_4$ (and other related ET compounds [1]) both quasi-1D and quasi-2D bands are present (see Fig. 5.2). As will be discussed below, the presence of this 1D band gives rise to SDW's [4,5,6,21], however

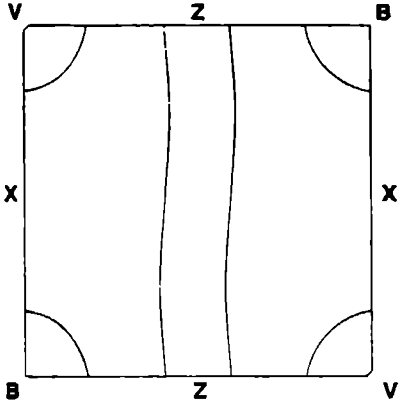

Figure 5.2 2D Brillouin zone and Fermi surface of (ET)$_2$KHg(SCN)$_4$ (after Ref. [19]). There are a pair of electron-like open Fermi surfaces running along the c-direction, and closed hole-like 2D pocket around the corner.

the effects are more subtle in ET salts than in the TMTSF salts, due to the presence of the 2D carriers.

(ET)$_2$KHg(SCN)$_4$, which has attracted much interest recently due to a spin-split structure of the SdH oscillations and an anomalous high field kink in the magnetoresistance (MR) at about 22 T, is also known to order antiferromagnetically below about 8 K. Figure 5.3(a) shows typical MR traces up to 20 T obtained at low temperatures, and in Fig. 5.3(b) one curve is plotted with the slowly varying background subtracted. Two SdH frequencies are present causing beating. One of the SdH frequencies, B_{F1} = 670 T, is always present, but the other frequency B_{F2} was found to be sample- or cooling-method-dependent, and can be as large as $\sim$ 860 T [4]. As the Fermi surface (see Fig. 5.2) only contains one closed hole pocket, only one frequency would be expected; the transport behaviour in this field range is therefore "anomalous".

Figure 5.3(c) shows the high-field MR with the large drop or "kink" [4,5,6] in resistance occurring around 22 T; at higher fields one single series of SdH oscillations is observed, with frequency B_F = 656 T. The angle dependence of the high-field (> 23 T) SdH oscillations follow the $1/\cos\theta$ dependence expected of a 2D metal, and there are also the amplitude and harmonic content oscillations expected from the varying spin to cyclotron splitting ratio as θ is varied [4]. The results above the 22 T kink transition are found to be in fair agreement with predictions made from the extended Hückel model [4,19], whereas the situation is rather more complicated at lower fields.

The antiferromagnetic ordering below 8 K could be explained in terms of an incommensurate SDW associated with the quasi-1D band [4]. A SDW would open up an energy gap along the quasi-1D band, via the mechanism of Fermi surface nesting as described in section 4.1.2, preventing the electrons taking part in the electrical conductivity; this is supported by the very isotropic MR below 22 T [4]. The remaining carriers (in the 2D

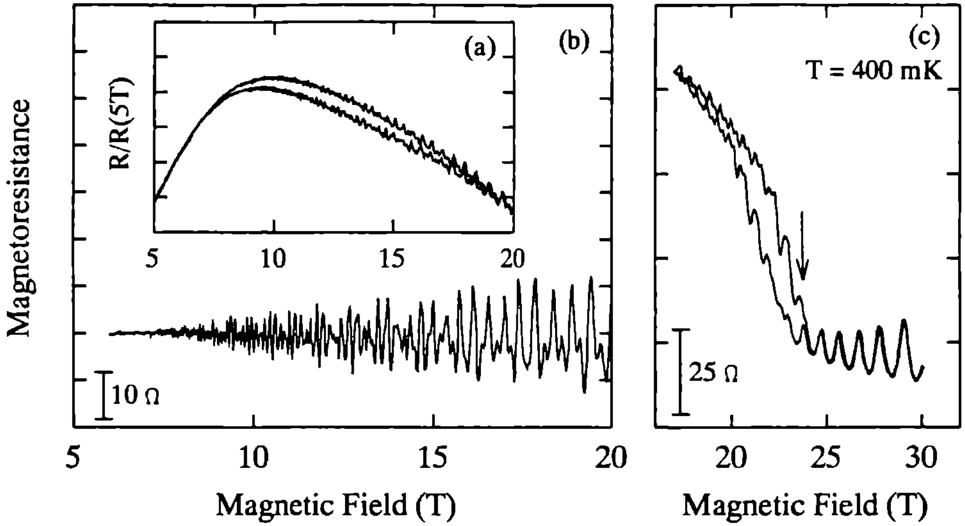

Figure 5.3 Magnetoresistance of $(ET)_2KHg(SCN)_4$; (a) Raw data for upsweeps and downsweeps of the field. (b) SdH oscillations with the background magnetoresistance removed (only one field sweep). (c) High field magnetoresistance showing a drop ("kink") in the resistance around 22 T.

pockets) and the SDW would form an interacting system, as suggested by the changes in MR occurring at the same temperature as the onset of antiferromagnetism [4,15]. In order to explain the presence of the "kink" transition it was suggested [4] that, at low fields, the system is not only antiferromagnetically ordered within the plane, but that there is also a magnetic superlattice in the b^*-direction (perpendicular to the 2D plane), causing a doubling of the unit cell along this axis. A possible mechanism for this is canted antiferromagnetic order within each plane, with the canting direction alternating from one layer to another (Fig. 5.4(a)). The result of this, is that the band structure becomes divided into two magnetic subbands separated by a band gap [4]. The formation of a magnetic band gap will double the number of SdH oscillation frequencies; a schematic representation of the possible Fermi surface is shown in Fig. 5.4(b). Above the 22 T transition, high external fields may change the magnetization so that all planes become equivalent (Fig. 5.4(c)), hence removing the magnetic band gap. (for an extensive discussion of the magneto-transport the reader is referred to Ref. [4] and for other recent models of the ground state, see Kartsovnik *et al.* [22]).

At fields below the kink feature, we are thus dealing with two closed 2D pockets of carriers. In order to obtain the transport masses, the amplitudes of the SdH oscillations have been measured as a function of temperature between 0.5 K and 5 K and fitted using the Lifshitz-Kosevich formula [23]. These masses can then be compared with the cyclotron

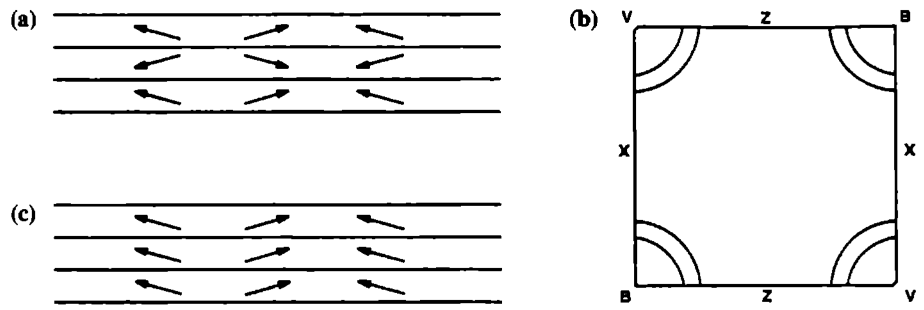

Figure 5.4 Schematic of effect of magnetic superlattice. (a) Represents the magnetic moments in an incommensurate spin-density-wave antiferromagnetic state, including a 2*b* magnetic superlattice due to a canted arrangement of dipoles. A possible from of the 2D section of the Fermi surface is shown in (b); there are now two concentric holes at the zone corner (*c.f.* Fig. 5.2). (c) Represents the suggested arrangement of dipoles at fields above the kink transition.

B_{F1}. The SdH oscillations of the secondary, higher frequency series are rather weaker, and it is not possible to make a meaningful estimate of the effective mass using the same method. Instead, the results of a separate harmonic ratio experiment are used [24], in which the ratio of the fundamental frequency of the SdH oscillations to its second harmonic is measured as a function of sample orientation (see [25] for a review of the technique). These indicate that the ratio of masses is $m^*_{\mathrm{tr1}}/m^*_{\mathrm{tr2}} \simeq 1.22$, so that $m^*_{\mathrm{tr2}} \simeq 2.4\ m_e$.

5.4 Cyclotron resonance measurements

5.4.1 Experimental details and results

The measurements were performed on crystals of (ET)$_2$KHg(SCN)$_4$ grown electrochemically using BEDT-TTF prepared by the method of Larsen and Lenoir [26] with KSCN, HgSCN, and 18Crown6 in a mixture of 90% 1,1,2-TCE and 10% ethanol. Crystals formed as small black distorted-diamond-shape platelets, with the platelet plane defined by the highly conducting 2D directions. The crystals were arranged in the form of a mosaic with the highly conducting planes perpendicular to the magnetic field, in order to increase the reflected signal from these small crystals. The FIR laser system used has been described in detail elsewhere [27]. The incident and reflected radiation were detected using two carbon bolometers, and the reflected radiation was normalized to the incident signal. Great care was taken to stabilize the intensity of the FIR laser system. The magnetic fields were provided by a 20 T Bitter magnet.

The measured FIR reflectivity at 1.2 K is shown in Fig. 5.5 for several different laser energies. Two rather sharp features are observed, occurring at fields which are proportional to the FIR energy, the characteristic behaviour of CR: The electron-spin-resonance

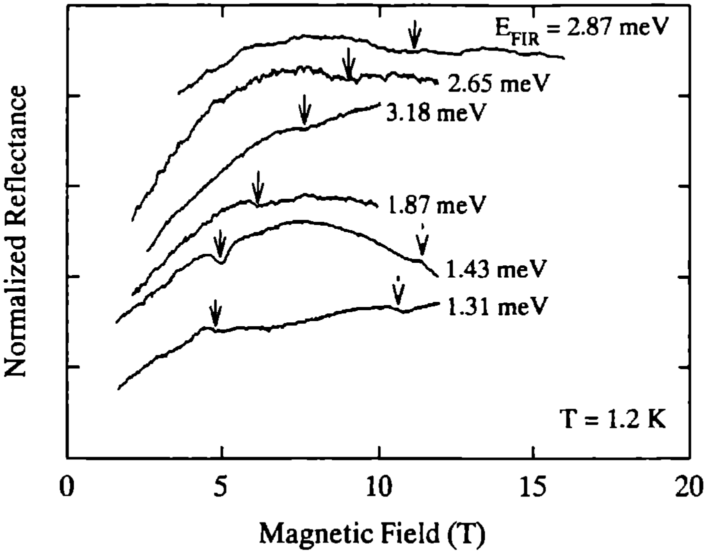

Figure 5.5 Normalized reflectivity of $(ET)_2KHg(SCN)_4$ at 1.2 K for different radiation energies. The CR features are marked with arrows.

of the observed resonances is narrow enough, nor at a high enough field, to be due to ESR. The resonances are superimposed on a gently varying background magnetoreflectance and nstrumental response. The strongest of the two features appears as a dip in reflectivity at 5 T with a FIR energy of 1.43 meV, and is very similar in form to CR reflectivity signals seen from 2D electron gases in semiconductor heterostructures when the underlyng reflectivity of the structure is high [27]. In contrast to the ~ 10% modulation of the reflectivity seen in the latter systems, however, the small skin depth of $(ET)_2KHg(SCN)_4$ means that the CR leads to only a ~ 0.6% change in reflectivity. At higher energies the dip becomes wider and shallower, whereas for lower energies the CR is observed as a peak. The latter behaviour is also seen in heterostructures under conditions of changing background reflectance [27]; the sharp changes in behaviour between 1.43 and 1.31 meV may be due to a low energy lattice phonon. The cause of the broadening of the resonance at higher energies is not yet known; it may represent the onset of resonant coupling to a phonon mode (cf. Ref. [27]). The weaker CR at higher fields (Fig. 5.5) also exhibits changes in shape as a function of energy. However, in the regime were the wavelength of the FIR radiation equals the dimensions of the crystal and the spacings between them n the mosaic, diffraction effects may be important and could also contribute or distort the lineshape in some way [29]. The field positions of the CR features are plotted against energy in Fig. 5.6. Effective masses of $m^*_{cr1} = (0.40 \pm 0.02)m_e$ and $m^*_{cr2} = (0.94 \pm 0.02)m_e$ are estimated from the linear slopes of the plots of radiation energy against CR field position

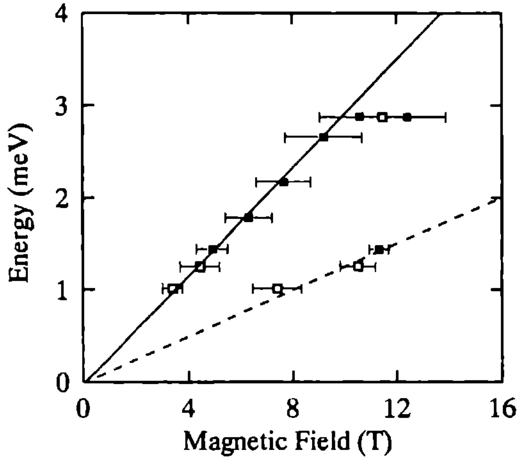

Figure 5.6 CR positions et each energy with ■ : reflectance minima, and □ : reflectance maxima. The horizontal bars correspond to the estimated widths of the CR features. The dashed and solid line correspond respectively to the effective masses of 0.40 m_e and 0.94 m_e.

5.4.2 Discussion

We now consider the relation between the two effective masses m^*_{cr1} and m^*_{cr2} observed in CR and the effective masses m^*_{tr1} and m^*_{tr2} measured from the SdH oscillations. A closed Fermi surface is necessary for the observation of both CR and SdH oscillations. In addition, in a system such as $(ET)_2KHg(SCN)_4$ one would expect the CR and SdH oscillations to be similarly affected by the various scattering mechanisms present, i.e. there will be a correlation between the strength of the CR and the SdH oscillations. The stronger CR can therefore be assigned to the 2D hole pocket associated with the dominant 670 T SdH oscillations and the weaker CR to the extra carrier pocket responsible for the secondary, higher frequency SdH oscillations series; however, note that, even if this assignment is inverted, the conclusions drawn below will remain unaffected.

Comparing data taken over comparable temperature ranges, the CR (1.2 K) yields effective masses of 0.4 and 0.94 m_e while the SdH oscillations (0.5-4.0 K) give values close to 2.0 m_e and 2.4 m_e, respectively. This difference is thought to be a consequence of Kohn's theorem [11,23], which states that at long wavelengths an external perturbation only couples to center-of-mass motion, which is independent of EEI. Thus CR, representing the excitation of a $q = 0$ magnetoplasmon, measures the "bare" band structure mass, renormalized only by electron-phonon interactions [27], whereas the transport mass, representing the $q = \infty$ magnetoplasmon case of a magnetoplasmon [30], is also renormalized by EEI. Some violations of Kohn's theorem due to nonparabolicity have been observed in CR in high mobility semiconductor heterojunctions [30,31], but these tend to lead to between the measured $m^*_{\rm cr}$ and $m^*_{\rm tr}$ for $(\mathrm{ET})_2\mathrm{KHg(SCN)}_4$ represents a direct gauge of the strength of the EEI in a 2D system as measured by the renormalization of the effective mass.

Effective masses may also by derived from the band structure calculated by Mori *et al.* [19]. On the basis of this band structure, a cyclotron mass of 1.2 m_e is obtained for the hole pocket. The plasma frequencies calculated are 0.77 eV for **E** polarized along a, and 0.35 eV for **E** along c. Experimental plasma frequencies in this material have been measured by Tamura *et al.* [32] and are 1.1 eV with **E** polarized along a, and 0.63 eV with **E** along c, suggesting that the true bandwidth is greater (and hence the effective mass is smaller) than predicted by Mori's band structure. Since the effective mass is inversely proportional to the square of the plasma frequency, we would expect a cyclotron mass of 0.47 m_e on the basis of the measured plasma frequencies. This value is close to the measured effective mass of the stronger CR.

The optical mass measurements (from CR and plasma frequency) are both insensitive to EEI and indicate a larger bandwidth in $(\mathrm{ET})_2\mathrm{KHg(SCN)}_4$ than that predicted from band structure calculations, which is in turn bigger than that deduced from transport measurements. A similar effect may take place in the 11 K superconductor $(\mathrm{ET})_2\mathrm{Cu(SCN)}_2$, where the transport mass is ~ 4 times larger than that expected from band structure calculations [7], a fact which has lead Toyota *et al.* [8] to point out that band structure calculations in BEDT-TTF salts almost always reproduce the experimentally observed Fermi surface shapes fairly reliably, but overestimate the bandwidth (*i.e.* underestimate the effective mass). Toyota *et al.* showed that the observed narrow bandwidth must be due to many-body renormalization, but in the absence of further data were unable to state whether this was due to electron-phonon interactions or EEI, or both. As electron-phonon interactions are expected to renormalize *both* $m^*_{\rm cr}$ and $m^*_{\rm tr}$ equivalently [33], the experiments reported in this work indicate that the major part of the observed difference between calculated and observed bandwidths is due to EEI, and that EEI lead to an enhancement of ~ 5 in the effective mass of the holes.

The EEI responsible for the effective mass renormalization can be described by a Hubbard model with an effective on-site Coulomb correlation energy $U_{\rm eff}$. Mass renormalization in the Hubbard model has been considered by Brinkman and Rice [34] using the Gutzwiller approximation. For a half-filled band the renormalization factor is $[1-(U_{\rm eff}/8\epsilon)^2]^{-1}$, where ϵ is the average energy of the electrons. For the present purposes a simplified view of the band structure of $(\mathrm{ET})_2\mathrm{KHg(SCN)}_4$ [19] will be taken. A dimer is regarded as the basic unit, which produces two dimer bands, the upper band being half filled. The experimentally observed mass enhancements of the order 2-5 imply values for $U_{\rm eff}/8\epsilon$ in the range 0.7-0.9. The average energy of the electrons in the upper subband is estimated to be ~ 60 meV from the band structure [19]. This leads to a value for $U_{\rm eff}$ for the dimer in the range 0.4-0.5 eV; in this model $U_{\rm eff}$ is associated with the intradimer correlation energy and the values obtained here are entirely consistent with typical values derived from optical spectra of a wide range of charge-transfer salts [35]. Recently, the cyclotron resonance effective masses have also been measured in other drawn above for the $(ET)_2KHg(SCN)_4$ salt.

5.5 Summary

We have measured cyclotron resonances in the quasi-2D organic charge-transfer salt $(ET)_2KHg(SCN)_4$ for the first time; these results indicate low carrier effective masses of 0.40 m_e and 0.94 m_e. In contrast, transport measurements reveal much higher effective masses $\sim 2.0\ m_e$ and $\sim 2.4\ m_e$. The difference between between transport and cyclotron masses is probably an indication of the strength of electron-electron interactions in the material.

References

1. *Organic Superconductors*, by T. Ishiguro and K. Yamaji, Springer Series in Solid-State Sciences **88**, (Springer-Verlag, Berlin, 1990).
2. *Organic Superconductivity*, edited by V.Z. Kresin and W.A. Little, (Plenum Press, New York, 1990).
3. J.M. Williams, A.M. Kini, H.H. Wang, K.D. Carlson, H. Geiser, L.K. Montgome, G.J. Pyrka, D.M. Watkins, J.M. Kommers, and S.J. Boryschu, Inorg. Chem. **29**, 3272 (1990).
4. F.L. Pratt, J. Singleton, M. Doporto, A.J. Fisher, T.J.B.M. Janssen, J.A.A.J. Perenboom, M. Kurmoo, W. Hayes, and P. Day, Phys. Rev. B **45**, 13904 (1992).
5. J.S. Brooks, C.C. Agosta, S.J. Klepper, M. Tokumoto, N. Kinoshita, H. Anzai, S. Uji, H. Aoki, A.S. Perel, G.J. Althas, and D.A. Howe, Phys. Rev. Lett. **69**, 156 (1992).
6. T. Sasaki and N. Toyota, Solid State Commun. **82**, 447 (1992).
7. F.L. Pratt, J. Singleton, M. Kurmoo, S.J.R.M. Spermon, W. Hayes, and P. Day in: *The Physics and Chemistry of Organic Superconductors*, edited by G. Saito and S. Kagoshima, Springer Proceedings in Physics **51** (Springer-Verlag, Berlin, 1990), p. 200.
8. N. Toyota, E.W. Fenton, T. Sasaki, and M. Tachiki, Solid State Commun. **72**, 859 (1989).
9. M. Tokumoto, A.G. Swanson, J.S. Brooks, C.C. Agosta, S.T. Hannahs, N. Kinoshita, H. Anzai, and J.R. Anderson, J. Phys. Soc. Jpn. **59**, 2324 (1990).
10. I.D. Parker, D.D. Pidram, R.H. Friend, M. Kurmoo, and P. Day, Synth. Metals **27**, A387 (1988); A.G. Swanson, J.S. Brooks, H. Ansai, N. Konoshita, M. Tokumoto, and K. Murata, Solid State Commun. **73**, 353 (1990). Phys. Rev. Lett. **67**, 2072 (1991).
11. W. Kohn, Phys. Rev. **123**, 1242 (1961).
12. M. Oshima, H. Mori, G. Saito, and K. Oshima, Chem. Lett. **1989**, 1159 (1989).
13. H.H. Wang, K.D. Carlson, H. Geiser, W.K. Kwok, M.D. Vashon, J.E. Thompson N.F. Larsen, G.D. McCabe, R.S. Hulsher, and J.M. Williams, Physica C **166**, 57 (1990).
14. T. Sasaki, H. Saito, and N. Toyota, Synth. Metals **42**, 2211 (1991).

15. T. Sasaki, N. Toyota, M. Tokumoto, N. Kinoshita, and H. Anzai, Solid State Commun. **75**, 93 (1990); **75**, 97 (1990).
16. T. Osada, R. Yagi, A. Kawasumi, S. Kagoshima, N. Miura, M. Oshima, H. Mori, T. Takamura, and G. Saito, Synthetic Metals **42**, 2171 (1991).
17. T. Osada, R. Yagi, S. Kagoshima, N. Miura, M. Oshima, H. Mori, and G. Saito, Phys. Rev. B **41**, 5428 (1990).
18. G. Saito, T. Enoki, K. Toriumi, and H. Inokuchi, Solid State Commun. **42**, 557 (1982).
19. H. Mori, S. Tanaka, M. Oshima, G. Saito, T. Mori, Y. Maruyama, and H. Inokuchi, Bull. Chem. Soc. Jpn. **63**, 2183 (1990).
20. W. Kang, G. Montambaux, J.R. Cooper, D. Jérome, P. Batail, and C. Lenoir, Phys. Rev. Lett. **62**, 2559 (1989).
21. F.L. Pratt, M. Doporto, J. Singleton, T.J.B.M. Janssen, J.A.A.J. Perenboom, M. Kurmoo, W. Hayes, and P. Day, Physica B **177**, 333 (1992).
22. M.V. Kartsovnik, A.E. Kovalev, and N.D. Kushch, J. Phys. I France **3**, 1187 (1993).
23. M. Doporto, J. Singleton, F.L. Pratt, T.J.B.M. Janssen, J.A.A.J. Perenboom, M. Kurmoo, W. Hayes, and P. Day, Physica B **177**, 348 (1992).
24. J. Singleton (unpublished).
25. J. Wosnitza, G.W. Crabtree, H.H. Wang, K.D. Carlson, M.D. Vashon, and J.M. Williams, Phys. Rev. Lett. **67**, 263 (1991).
26. J. Larsen and C. Lenoir, Synthesis **1988**, 134 (1988).
27. C.J.G.M. Langerak, J. Singleton, J.A.A.J. Perenboom, F.M. Peters, J.T. Devreese, D.J. Barnes, R.J. Nicholas, S. Huant, J.J. Harris, C.T. Foxon, and B. Etienne, Phys. Scr. **T39**, 308 (1991).
28. M. Newton, M. Kurmoo, F.L. Pratt, and J. Singleton (unpublished).
29. T. Timusk in: *Low Dimensional Conductors and Superconductors*, edited by D. Jérome and L.G. Caron (Plenum, New York, 1987), p. 275.
30. R.J. Nicholas, D.J. Barnes, R.G. Clark, S.R. Haynes, J.R. Mallett, A.M. Suckling, A. Usher, J.J. Harris, C.T. Foxon, and R. Willet in: *High Magnetic Fields in Semiconductor Physics II*, edited by G. Landwehr, Springer Series in Solid-State Sciences **87** (Springer-Verlag, Berlin, 1989), p. 115.
31. M. Watts, I. Auer, R.J. Nicholas, J.J. Harris, and C.T. Foxon in: *High Magnetic Fields in Semiconductor Physics III*, edited by G. Landwehr, Springer Series in Solid-State Sciences **101** (Springer-Verlag, Berlin, 1989), p. 581.
32. M. Tamura, R. Masuda, T. Naito, H. Tajima, H. Kuroda, A. Kobayashi, M. Tokumoto, N. Kinoshita, and A. Anzai, Synthetic Metals **42**, 2499 (1991).
33. J.W. Wilkins in: *Electrons at the Fermi Surface*, edited by M. Springford (Cambridge Univ. Press, Cambridge, 1980), p. 46.
34. W.F. Brinkman and T.M. Rice, Phys. Rev. B **2**, 4302 (1970).
35. S. Mazumdar and S.N. Dixit, Phys. Rev. B **34**, 3683 (1986).
36. J. Singleton, F.L. Pratt, M. Doporto, J.M. Caulfield, S.O. Hill, T.J.B.M. Janssen, I. Dekkers, G. Pitsi, F. Herlach, W. Hayes, J.A.A.J. Perenboom, M. Kurmoo, and P. Day, Physica B **184**, 470 (1993).

Summary

In this thesis we have reported a study of the electronic properties of a number of low dimensional systems which were realized either artificially in semiconductor systems or which occur naturally in organic charge-transfer salts. In these investigations we have made use primarily of far-infrared (FIR) spectroscopy, which in combination with a magnetic field, is a very versatile tool to study the excitation spectrum in solids.

The first part of this thesis is devoted to the study of charge confinement in semiconductor systems. The starting point for making these systems is the high mobility two-dimensional electron gas (2DEG) in a GaAs-(Ga,Al)As heterostructure in which the electron motion is already quantized in one direction. Imposing additional ultrafine lateral confinement on the original 2DEG will quantize the electron motion in the lateral direction as well. In this way one can obtain zero-, and one-dimensional electronic systems (chapters 1 and 2). Chapter 3 is devoted to the confinement of the holes in a two-dimensional sheet.

In chapter 1, we discussed the FIR response of a number of quasi-0D quantum dot devices with different lithographically defined radii. In our devices the dots were defined via the depleting action of a metal gate. The use of a transparent back-gate allowed the simultaneous measurement of capacitance and FIR transmission on the same quantum dot sample. At small negative gate voltages, when the system corresponds to a density modulated 2DEG, we observed 2D magnetoplasmons, where the 2D array of dots acted as a grating coupler. The energies of the plasmons were found to be in good agreement with the theoretical magnetic field- and carrier density-dependence. At more negative gate voltages, when isolated dots are formed, an absorption peak was seen to arise which, for the larger-dot sample, could be described by a (collective) edge magnetoplasmon model. Using this model and the carrier densities derived from the capacitance data, we calculated that the dot radius of our devices can be reduced up to 50% by strengthening the gate voltage. Furthermore, the number of electrons in the dot could be determined independently from the calculated lineshape, and was found to be in reasonable agreement with the values obtained from the plasmon model. For the smaller-dot samples it was found that (single particle) quantum confinement is becoming more important.

One speaks of point contacts when a current is passing ballistically through a narrow constriction. For constrictions larger than the Fermi wavelength they are called "classical" as opposed to "quantum point contacts" where the opposite is true. A quantum point contact was made using a split gate geometry on top of a high mobility GaAs-(Ga,Al)As heterostructure. In chapter 2, we presented a transport and optical study of such quantum point contact devices in the nonlinear transport regime. In the differential conductivity of these devices, we observed new quantized half integer plateaux in the high bias regime. These plateaux are explained in terms of a model incorporating the effect of the bias voltage on the chemical potentials on the two sides of the 1D channel in the adiabatic regime. Under a constant transverse magnetic field this mechanism was used to determine the 1D subband spacings, and was found to agree with theoretical values. In the optical experiment, a strong *dc* voltage response, which depends strongly on the number of occupied 1D subbands, was observed when a quantum point contact was subjected to FIR radiation. This signal was explained by the rectification of the applied high frequency electric field. The nonlinearity causing the rectification is the result of the fact that an unequal number of 1D subbands is populated for the two opposite directions of current in the channel. We estimated that quantum detection should be feasible, and this in principle implies that there are many interesting applications for studying the fundamental properties of ballistic charge transport at ultra-high frequencies in quantum confined electron devices.

In chapter 3, we investigated the cyclotron resonance behaviour of several high mobility 2D hole gas samples grown onto (311)A oriented planes in magnetic fields up to 20 T. Using swept-frequency / fixed-field FIR spectroscopy two resonances were generally observable, with the absorption strength exhibiting a clear anti-crossing behaviour as the magnetic field increased. A Landau fan diagram calculation for the (311) direction is extremely difficult in this low symmetry direction. The present data have therefore been compared with a self-consistent theory for the higher symmetry (100) direction, assuming that the observed absorption represents transitions within the heavy-hole subband and between the heavy-hole and light-hole subband. In general, these calculations provide a strong support for the proposed interpretation, keeping in mind the anticipated changes with respect to the lower symmetry (311) direction. In that case additional off-diagonal terms will appear in the Hamiltonian leading to greater mixing effects and further relaxation of selection rules.

The second part of this thesis is devoted to magneto-optical aspects of low dimensional organic charge-transfer salts. Organic conductors attract considerable interest because they exhibit many phenomena that do not occur in ordinary metals. They show a remarkable competition between superconducting, magnetic, insulating and metallic states, which depends on the constituents of the compound and on external parameters such as pressure, temperature and magnetic field. Most of these unusual properties arise because the organic crystals are highly anisotropic, so that conductivity is negligible along one or two crystal axes. Depending on the type of molecules and the way in which they are stacked in the crystal, their electronic properties may range from quasi-one-dimensional to quasi-two-dimensional.

In chapter 4, we presented spectroscopic details of the FIR excitation spectrum of the compound $(TMTSF)_2ClO_4$, which is a well known member of the quasi-1D family of charge-transfer salts, also known as Bechgaard salts. This compound exhibits a complex phase diagram in the presence of a magnetic field. The specific emphasis in our work has been on the details in the excitation spectrum related to the antiferromagnetic ordering induced by the magnetic field. In a series of three experiments, each concentrating on a different parameter of the phase diagram, the details of the excitation spectrum have been presented (magnetic field up to 30 T, energy between 0.3 and 6.0 meV, and temperature function of magnetic field and temperature follow closely the phase diagram established from thermodynamic measurements. The experiments demonstrate that the cascade of field-induced spin-density-wave (FI-SDW) phase transitions and the high field reentrant phase line can be optically detected. We argued that the observed cyclotron resonance features may be associated with the rapid oscillation phenomena. The spectroscopic data indicated that the gap in the FI-SDW state is independent of the value of the magnetic field and temperature as opposed to the predictions of the standard model. However, this result is consistent with a stepwise increase of the carrier density in the condensed SDW ground state upon each phase transition into a lower index subphase. In addition, the first indication of a pinned collective mode excitation in the microwave region has been reported, and of an enhanced coupling of the 31 cm^{-1} zone folding phonon mode with the electronic system as a result of SDW formation.

Finally, in chapter 5, we presented the first cyclotron resonance measurements in the quasi-2D organic charge-transfer salt $(\mathrm{BEDT\text{-}TTF})_2\mathrm{KHg(SCN)}_4$. This salt is closely related to the high-T_c salt $(\mathrm{BEDT\text{-}TTF})_2\mathrm{Cu(SCN)}_2$ and particularly interesting because of the rather unusual presence of both magnetic order and strong magneto-oscillatory effects. Our cyclotron resonance measurements indicated low carrier effective masses of 0.40 m_e and 0.94 m_e. In contrast, transport measurements revealed much higher effective masses $\sim 2.0\ m_e$ and $\sim 2.4\ m_e$. The difference between between transport and cyclotron masses is probably an indication of the strength of electron-electron interactions in this material.

Samenvatting

Dit proefschrift behandelt de elektronische eigenschappen van een aantal laag-dimensionale systemen, die kunstmatig zijn gerealiseerd in halfgeleider structuren of op natuurlijke wijze voorkomen in organische "charge-transfer" zouten. Hierbij is voornamelijk gebruik gemaakt van ver-infrarood spectroscopie. In combinatie met een magneetveld is ver-infrarood spectroscopie een uitermate geschikte techniek om het excitatiespectrum van vaste stoffen te bestuderen.

Het eerste deel van dit proefschrift is gewijd aan de studie van de opsluiting van ladingsdragers in laag-dimensionale halfgeleider systemen. Om een laag-dimensionaal systeem te verkrijgen, wordt uitgegaan van het twee-dimensionaal (2D) elektronen gas in een GaAs-(Ga,Al)As heterostructuur. Hierin is de bewegingsvrijheid van de elektronen reeds begrensd en gequantiseerd in één richting. Door het aanbrengen van ultrafijne begrenzingen in het vlak van het originele 2D elektronen gas zal ook de bewegingsvrijheid van de elektronen in het vlak gequantiseerd worden. Op deze manier is het mogelijk om nul- (0D) en één-dimensionale (1D) elektronische systemen te creëren (hoofdstuk 1 en 2). Hoofdstuk 3 is gewijd aan de opsluiting van gaten in een twee-dimensionaal vlak.

In hoofdstuk 1 zijn ver-infrarood metingen gepresenteerd aan quasi-0D "quantum dot devices". De diameter van deze quantum dots wordt bepaald door de lithografische structuur van de "gate", en kon nog worden gereduceerd d.m.v. ladingsdepletie. Door het gebruik van een transparant grondcontact is het mogelijk om zowel ver-infrarood-transmissie- als capaciteitsmetingen aan het zelfde device te verrichten. Bij kleine negative spanningen op de gate komt het systeem overeen met een dichtheids-gemoduleerd 2D elektronen gas. In deze situatie zijn 2D magnetoplasmonen waargenomen als gevolg van de 2D contactstructuur op het sample die als inkoppel-rooster functioneert. De energieën van de plasmonen komen goed overeen met de theoretische magneetveld- en ladingsdichtheid-afhankelijkheid. Bij sterke negative spanningen bestaat het systeem uit van elkaar geïsoleerde dots. In deze situatie werd, in de grootste-dot devices, een absorptiepiek waargenomen, welke beschreven kon worden met een (veel-deeltjes) "edge-magnetoplasmon" model. Door het gebruik van de ladingsdichtheden, verkregen uit de capaciteitsmetingen, kon worden berekend, dat de straal van de dots kon worden gereduceerd met 50% door de gate-spanning. Verder kon het aantal elektronen in de dot ook worden berekend uit de lijnvorm. Dit aantal is in goede overeenstemming met het plasmonmodel. In de kleinste-dot devices werd gevonden dat (één-deeltjes) quantum effecten belangrijker worden.

Men spreekt van puntcontacten als een stroom ballistisch door een kleine constrictie wordt gestuurd. Als deze constrictie groter is dan de Fermi-golflengte noemt men dit een "klassiek" contact, voor een "quantum puntcontact" is het tegenovergestelde het geval. Een quantum puntcontact wordt verkregen door een "split-gate" aan te brengen op een hoge mobiliteits GaAs-(Ga,Al)As heterostructuur. In hoofdstuk 2 zijn transport en optische metingen gepresenteerd aan dergelijke quantum puntcontacten in het bereik met niet-lineair transport. In de differentiële geleiding, onder hoge spanningen, zijn nieuwe gequantiseerde plateau's waargenomen bij half-hele waarden. Deze plateau's konden worden verklaard in termen van een adiabatisch model dat het effect van de spanning op de chemische potentiaal aan weerszijden van het 1D kanaal in beschouwing neemt. In een vast en loodrecht magneetveld werd dit mechanisme gebruikt om de energie afstand tussen de subbanden te bepalen, welke in goede overeenstemming is met de theoretische waarde. In het optische experiment werd een sterke dc spanningsresponse waargenomen, die afhangt van het aantal 1D subbanden in het quantum puntcontact, als dit bestraald wordt met ver-infrarood licht. Dit signaal werd verklaard als rectificatie van het aangelegde hoogfrequente elektrische veld. De niet-lineariteit die hiervoor verantwoordelijk is, is het gevolg van de ongelijke bezetting van 1D subband niveau's voor de tegengestelde stroomrichtingen in het puntcontact. Een schatting laat zien dat het mogelijk is om quantum detectie te verkrijgen, en dit impliceert een aantal interessante toepassingen voor het bestuderen van ballistisch ladingstransport bij ultrahoge frequenties in quantum devices.

In hoofdstuk 3 zijn cyclotron resonantie metingen gepresenteerd in magneetvelden tot 20 T aan een aantal hoge mobiliteits 2D gaten-gas samples, gegroeid op het (311)A georiënteerde kristalvlak. In energie-afhankelijke en vast-magneetveld ver-infrarood metingen werd een absorptie gevonden, welke een sterke splitsing vertoonde als het magneetveld werd verhoogd. Omdat een berekening van de Landau-niveau's voor de lage-symmetrie (311) richting erg lastig is, zijn de resultaten vergeleken met reeds voorhanden berekeningen voor de hogere symmetrie (100) richting. Aangenomen werd dat de waargenomen absorpties overgangen zijn binnen de zware-gaten subband, en tussen de zware-gaten en lichte-gaten subband. In het algemeen zijn de berekeningen in redelijke overeenstemming met onze interpretatie, mits men de verschillen tussen de (100) en (311) richting in het oog houdt. Voor de (311) richting zullen extra niet-diagonaal elementen in de Hamiltoniaan zorgen voor een grotere vermenging van de Landau-niveau's en een verzwakking van de selectie regels.

Het tweede gedeelte van dit proefschrift is gewijd aan de magneto-optische aspecten van laag-dimensionale organische "charge-transfer" zouten. Het interessante aan deze organische geleiders is, dat ze eigenschappen bezitten die niet voorkomen in gewone geleidende metalen. Ze vertonen een grote verscheidenheid in supergeleidende, magnetische, niet-geleidende en metallische toestanden. Deze toestanden hangen af van de moleculaire samenstelling en uitwendige parameters zoals druk, temperatuur en magneetveld. Veel van de ongewone eigenschappen zijn het gevolg van het feit dat organische kristallen sterk anisotroop zijn, zodat de geleiding verwaarloosbaar is in één of twee kristalrichtingen. Afhankelijk van het type moleculen en de manier waarop deze in het kristal gestapeld zijn, kunnen de elektrische eigenschappen variëren van quasi-één-dimensionaal tot quasi-twee-dimensionaal.

In hoofdstuk 4 zijn ver-infrarood spectroscopische metingen gepresenteerd aan het charge-transfer zout $(TMTSF)_2ClO_4$. Dit materiaal is een bekend lid van de quasi-1D een zeer complex fasediagram. De aandacht was in ons werk speciaal gericht op de details in het excitatiespectrum die samenhangen met de zogenaamde "veld-geïnduceerde-spindichtheids-golven". De resultaten zijn gepresenteerd in een serie van drie experimenten die zich elk concentreerde op een andere parameter van het fasediagram (magneetvelden tot 30 T, energieën tussen 0.3 en 6.0 meV en temperaturen tussen 0.3 en 7.0 K). Gevonden werd dat, als functie van magneetveld en temperatuur, de optisch waargenomen fase-overgangen in goede overeenstemming zijn met het fasediagram zoals dat is bepaald uit thermodynamische metingen (b.v. specifieke warmte en magnetisatie). De experimenten lieten zien dat de reeks van fase-overgangen en de hoog-veld "reentrant" fase-overgang optisch gedetecteerd kunnen worden. Er werd beargumenteerd dat de waargenomen cyclotron resonanties samen kunnen hangen met de eveneens optisch waargenomen snelle oscillaties. De spectroscopische resultaten vertoonden in de veld-geïnduceerde-spindichtheids-golf toestand een magneetveld- en temperatuur-onafhankelijke energie-"gap" in het excitatiespectrum, en dit is strijdig met de voorspellingen van het "standaard model". Onze resultaten laten echter duidelijk zien dat de ladingsdichtheid in de gecondenseerde spin-dichtheids-golf toestand stapsgewijs hoger wordt bij elke fase-overgang naar een subfase met lagere index. Bovendien hebben we voor het eerst aanwijzingen gevonden voor een "gepinde" collectieve excitatie in het microgolf gebied en voor een versterkte koppeling, als gevolg van spin-dichtheids-golf vorming, tussen het 31 cm^{-1} fonon met het elektronische systeem. Dit fonon wordt optisch actief t.g.v. de door ordening gereduceerde Brillouin zone.

In hoofdstuk 5 tenslotte zijn cyclotron resonantie metingen gepresenteerd aan het quasi-2D organische charge-transfer zout (BEDT-TTF)$_2$KHg(SCN)$_4$. Dit zout is nauw verwant aan het hoge-T_c zout (BEDT-TTF)$_2$Cu(SCN)$_2$, en interessant omdat zowel magnetische ordening als sterke magneto-oscillatie effecten kunnen worden waargenomen. Uit de cyclotron resonantie metingen volgden relatief lage waarden voor de effectieve massa's van 0.4 m_e en 0.9 m_e. Dit in tegenstelling tot de massa's bepaald uit transportmetingen die veel hogere waarden van 2.0 m_e en 2.4 m_e geven. Het verschil tussen transport- en cyclotronmassa's is waarschijnlijk een indicatie voor de sterkte van de elektron-elektron wisselwerking in dit zout.

List of publications

- N_s-dependent polaron effects in GaAs-(Ga,Al)As heterojunctions.
  C.J.G.M. Langerak, J. Singleton, D.J. Barnes, P.J. van der Wel, R.J. Nicholas, M.A. Hopkins, T.J.B.M. Janssen, J.A.A.J. Perenboom, and C.T. Foxon in: *High Magnetic Fields in Semiconductor Physics II*, edited by G. Landwehr, Springer Series in Solid State Sciences **87**, 449 (1989).
- 2D magnetopolaron coupling to both homopolar and longitudinal optic phonons in the layer compound InSe.
  D.F. Howell, R.J. Nicholas, C.J.G.M. Langerak, J. Singleton, T.J.B.M. Janssen, and A. Chevy, J. Phys.: Condens. Matter **1**, 7493 (1989).
- 2D cyclotron resonance and magneto-polaron coupling to homopolar and LO phonons in the layered semiconductor InSe.
  D.F. Howell, T.J.B.M. Janssen, R.J. Nicholas, C.J.G.M. Langerak, J. Singleton, and A. Chevy, Surface Science **229**, 496 (1990).
- One-dimensional subband effects in the conductance of multiple quantum wires in Si metal-oxide-semiconductor field-effect transistors.
  J.R. Gao, C. de Graaf, J. Caro, S. Radelaar, M. Offenberg, V. Lauer, J. Singleton, T.J.B.M. Janssen, and J.A.A.J. Perenboom, Phys. Rev. B **41**, 12315 (1990).
- Ballistic transport in one dimension: additional quantisation produced by an electric field.
  N.K. Patel, L. Martin-Moreno, M. Pepper, R. Newbury, J.E.F. Frost, D.A. Ritchie, G.A.C. Jones, T.J.B.M. Janssen, J. Singleton, and J.A.A.J. Perenboom, J. Phys.: Condens. Matter **2**, 7247 (1990).
- Far-infrared photoconductive response of a one dimensional GaAs/AlGaAs ballistic channel.
  N.K. Patel, T.J.B.M. Janssen, J. Singleton, M. Pepper, G.A.C. Jones, J.E.F. Frost, D.A. Ritchie, D.C. Peacock, R. Brown, H. Ahmed, D.G. Hasko, and J.A.A.J. Perenboom in: *Proc. 20th Int. Conf. on the Physics of Semiconductors*, edited by E.M. Anastassakis and J.D. Joannopoulos, (Thessaloniki 1990), p. 2371 (1991).
- One-dimensional subbands in multiple quantum wires in Si-MOSFET's.
  J.R. Gao, C. de Graaf, J. Caro, S. Radelaar, M. Offenberg, V. Lauer, J. Singleton, T.J.B.M. Janssen, and J.A.A.J. Perenboom in: *Proc. 20th Int. Conf. on the Physics of Semiconductors*, edited by E.M. Anastassakis and J.D. Joannopoulos, (Thessaloniki 1990), p. 2339 (1991).

- Thermal transport in free-standing semiconductor fine wires.
  A. Potts, M.J Kelly, D.G. Hasko, C.G. Smith, J.R.A. Cleaver, H. Ahmed, D.C. Peacock, J.E.F. Frost, D.A. Ritchie, G.A.C. Jones, J. Singleton, and T.J.B.M. Janssen, Superlattices and Microstructures **9**, 315 (1991).
- Photoconductive response of a quasi-one dimensional channel.
  T.J.B.M. Janssen, N.K. Patel, J. Singleton, M. Pepper, H. Ahmed, D.G. Hasko, R.J. Brown, J.A.A.J. Perenboom, G.A.C. Jones, J.E.F. Frost, D.C. Peacock, and D.A. Ritchie in: *Granular Nanoelectronics*, edited by D.K. Ferry, NATO ASI series B: Physics **251**, 551 (1991).
- Magnetoresistance studies of β''-ET$_2$ AuBr$_2$.
  M. Doporto, F.L. Pratt, W. Hayes, J. Singleton, T.J.B.M. Janssen, M. Kurmoo, and P. Day, Synthetic Metals **41-43**, 1903 (1991).
- Magnetotransport studies of (BEDT-TTF)$_2$Cu(SCN)$_2$.
  F.L. Pratt, M. Doporto, W. Hayes, J. Singleton, T.J.B.M. Janssen, M. Kurmoo, and P. Day, Synthetic Metals **41-43**, 2195 (1991).
- Recent high-field investigations of semiconductor nanostructures and other systems at Nijmegen.
  J. Singleton, J.A.A.J. Perenboom, and T.J.B.M. Janssen in: *High Magnetic Fields in Semiconductor Physics III*, edited by G. Landwehr, Springer Series in Solid State Science **101**, 686 (1992).
- Thermal transport in free-standing GaAs wires in a High Magnetic field.
  A. Potts, J. Singleton, T.J.B.M. Janssen, M.J. Kelly, C.G. Smith, D.G. Hasko, D.C. Peacock, J.E.F. Frost, D.A. Ritchie, G.A.C. Jones, J.R. Cleaver, and H. Ahmed in: *High Magnetic Fields in Semiconductor Physics III*, edited by G. Landwehr, Springer Series in Solid State Science **101**, 325 (1992).
- Far-infrared transmission of voltage-tunable GaAs-(Ga,Al)As quantum dots in high magnetic fields.
  N.K. Patel, T.J.B.M. Janssen, J. Singleton, M. Pepper, H. Ahmed, D.G. Hasko, J.A.A.J. Perenboom, G.A.C. Jones, J.E.F. Frost, D.C. Peacock, and D.A. Jones in: *High Magnetic Fields in Semiconductor Physics III*, edited by G. Landwehr, Springer Series in Solid State Science **101**, 339 (1992).
- Magnetoconductance of Si MOSFET quantum wires: weak localization and magnetic depopulation of 1D subbands.
  J.R. Gao, C. de Graaf, J. Caro, S. Radelaar, M. Offenberg, V. Lauer, J. Singleton, and T.J.B.M. Janssen in: *High Magnetic Fields in Semiconductor Physics III*, edited by G. Landwehr, Springer Series in Solid State Science **101**, 313 (1992).
- Magnetic field dependent energy levels in a highly anisotropic electronic material.
  A.S. Perel, J.S. Brooks, C.J.G.M. Langerak, T.J.B.M. Janssen, J. Singleton, J.A.A.J. Perenbooom, G. Montambaux, and L.Y. Chiang, Phys. Rev. Lett. **61**, 2072 (1992).

- The two dimensional electron gas at the CdTe/InSb interface: cyclotron resonance and Shubnikov-de Haas investigations.
  R.T. Grimes, T.J.B.M. Janssen, M.B. Stanaway, C.J.G.M. Langerak, J. Singleton, D.E. Ashenford, B. Lunn, G. Hill, and J.M. Chamberlain, Surface Science **267**, 133 (1992).
- Cyclotron resonance and electron-electron interactions in the organic metal (BEDT-TTF)$_2$KHg(SCN)$_4$.
  M. Doporto, J. Singleton, F.L. Pratt, T.J.B.M. Janssen, J.A.A.J. Perenboom, M. Kurmoo, W. Hayes, and P. Day, *Research on High Magnetic Fields*, edited by F.R. de Boer, Physica B **177**, 333 (1992).
- Magnetotransport studies of the organic metals (BEDT-TTF)$_2$AuBr$_2$ and (BEDT-TTF)$_2$KHg(SCN)$_4$.
  F.L. Pratt, M. Doporto, J. Singleton, T.J.B.M. Janssen, J.A.A.J. Perenboom, M. Kurmoo, W. Hayes, and P. Day in: *Research on High Magnetic Fields*, edited by F.R. de Boer, Physica B **177**, 348 (1992).
- A far-infrared cyclotron resonance study of electron dynamics in (BEDT-TTF)$_2$-KHg(SCN)$_4$.
  J. Singleton, F.L. Pratt, M. Doporto, T.J.B.M. Janssen, J.A.A.J. Perenboom, M. Kurmoo, W. Hayes, and P. Day, Phys. Rev. Lett. **68**, 2500 (1992).
- Magnetotransport and Fermiology of (BEDT-TTF)$_2$KHg(SCN)$_4$.
  F.L. Pratt, J. Singleton, M. Doporto, A.L. Fisher, T.J.B.M. Janssen, J.A.A.J. Perenboom, M. Kurmoo, and P. Day, Phys. Rev. B **45**, 13904 (1992).
- FIR-spectroscopy of the field induced spin density wave gap in (TMTSF)$_2$ClO$_4$.
  T.J.B.M. Janssen, A.S. Perel, A.M. Gerrits, W. Kang, J.S. Brooks, A. Wittlin, J.A.A.J. Perenboom, and P.J.M. van Bentum, Phys. Rev. B **46**, 8663 (1992).
- A novel mechanism for parallel conduction in GaAs-(Ga,Al)As heterojunctions.
  R.M. Kusters, T.J.B.M. Janssen, C.J.G.M. Langerak, J. Singleton, and J.A.A.J. Perenboom, Semicond. Sci. Technol. **7**, 961 (1992).
- Observation of plasmons and edge magnetoplasmon in voltage-tunable dots in GaAs/AlGaAs heterostructures.
  N.K. Patel, T.J.B.M. Janssen, J. Singleton, M. Pepper, J.A.A.J. Pereboom, D.A Ritchie, J.E.F. Frost, and G.A.C. Jones, J. Phys.: Condens. Matter **5**, 1517 (1993)
- Magneto-optics and magneto-capacitance studies of voltage-tunable GaAs/AlGaAs quantum dots.
  D.D. Arnone, T.J.B.M. Janssen, M. Pepper, J.A.A.J. Pereboom, D.A. Ritchie J.E.F. Frost, and G.A.C. Jones, J. Phys.: Condens. Matter **5**, L1 (1993).
- Cyclotron resonance studies of electron dynamics in BEDT-TTF salts.
  S.O. Hill, J. Singleton, F.L. Pratt, M. Doporto, W. Hayes, T.J.B.M. Janssen J.A.A.J. Perenboom, M. Kurmoo, and P. Day, Synthetic Metals **56**, 2566 (1993).

- Magneto-optical and magneto-transport studies of electron-electron interactions in organic superconductors using fields up to 50 T.
  J. Singleton, F.L. Pratt, M. Doporto, J.M. Caulfield, S.O. Hill, T.J.B.M. Janssen, I. Dekkers, G. Pitsi, F. Herlach, W. Hayes, J.A.A.J. Perenboom, M. Kurmoo, and P. Day, Physica B **184**, 470 (1993).
- Cyclotron resonance of high mobility GaAs-(Ga,Al)As (311) 2DHG's.
  S.D. Hawksworth, S.O. Hill, T.J.B.M. Janssen, J. Singleton, M.J. Chamberlain, U. Ekenberg, G.M. Summers, G.A. Davies, R.J. Nicholas, E.C. Valadares, M. Henini, and J.A.A.J. Perenboom, Semicond. Sci. Technol. **8**, 1465 (1993).
- FIR spectroscopy of the FI-SDW gap in a Q1D organic conductor.
  A.M. Gerrits, T.J.B.M. Janssen, J.S. Brooks, A. Wittlin, J.A.A.J. Perenboom, and P.J.M. van Bentum, Proc. of the tenth Int. Conf. on Electronic Properties of Two-Dimensional Systems, 1993, Newport 1993, and Surface Science.
- The FI-SDW formation in $(TMTSF)_2ClO_4$ investigated in the infrared.
  A.M. Gerrits, T.J.B.M. Janssen, J.S. Brooks, A. Wittlin, J.A.A.J. Perenboom, and P.J.M. van Bentum, Journal de Physique IV (France) **3**, C2-299 (1993).
- High field magnetotransport studies of $(ET)_2 2MHg(SCN)_4$ salts ($M=K$, NH_4).
  J. Singleton, F.L. Pratt, M. Doporto, J.M. Caulfield, W. Hayes, I. Dekkers, G. Pitsi, F. Herlach, T.J.B.M. Janssen, J.A.A.J. Perenboom, M. Kurmoo, and P. Day, Synthetic Metals **56**, 2198 (1993).
- High magnetic field studies of two dimensional organic molecular metals based on ET.
  J. Singleton, J.M. Caulfield, S.O. Hill, P.T.J. Hendriks, F.L. Pratt, M. Doporto, I. Dekkers, G. Pitsi, F. Herlach, W. Hayes, T.J.B.M. Janssen, J.A.A.J. Perenboom, M. Kurmoo, and P. Day, to be published.
- A new mechanism for high-frequency rectification in a ballistic quantum point contact.
  T.J.B.M. Janssen, J.C. Maan, J. Singleton, N.K. Patel, and M. Pepper, to be published.

Curriculum Vitae

Jan-Theodoor Janssen
geboren op 2 november 1965 te Oudenbosch

1978-1984	Atheneum aan het Thomas More College te Oudenbosch
1984-1989	Studie Natuurkunde, Katholieke Universiteit Nijmegen Afstudeerrichting: experimentele vaste stof fysica Afstudeerthema: Magneto-optische en magneto-transport studie van het polaron effect in twee-dimensionale elektronen gassen
1989-1993	Promotie onderzoek in dienst van de Stichting voor Fundamenteel Onderzoek der Materie aan de Katholieke Universiteit Nijmegen op de afdeling Experimentele Vaste Stof Fysica 2 en het Laboratorium voor Hoge Magneetvelden, o.l.v. Prof. Dr. H. van Kempen en Dr. J.A.A.J. Perenboom

ISBN 90-9006609-8